N66-22355
(ACCESSION NUMBER)

(THRU)

234
(PAGES)

1
(CODE)

CR-65319
(NASA CR OR TMX OR AD NUMBER)

17
(CATEGORY)

FACILITY FORM 602

GPO PRICE $

CFSTI PRICE(S) $

Hard copy (HC) 6.00

Microfiche (MF) 1.25

ff 653 July 65

THE Marquardt CORPORATION

VAN NUYS, CALIFORNIA

THE Marquardt CORPORATION VAN NUYS, CALIFORNIA

[redacted]

FEBRUARY 1966 REPORT PR-3009-F

(Title -- Unclassified)

FINAL REPORT

INVESTIGATION OF HIGH STRAIN RATE BEHAVIOR OF REFRACTORY ALLOYS AND COATINGS

FEBRUARY 1966

CONTRACT NAS 9-4905

PROJECT 3009

PREPARED BY:

T. Miyagishima

T. Miyagishima
Principal Investigator

APPROVED BY:

I E Rosman

I. E. Rosman, Manager
Design Engineering

APPROVED BY:

E. P. Perlman

E. P. Perlman
Program Manager

TABLE OF CONTENTS

TABLE OF CONTENTS (continued)

LIST OF TABLES

LIST OF TABLES (continued)

LIST OF ILLUSTRATIONS

LIST OF ILLUSTRATIONS (continued)

I. INTRODUCTION AND OBJECTIVES

This investigation evolved as a result of extensive testing at The Marquardt Corporation during the development of the Apollo Service Module Reaction Control System Engine. Very high transient, near instantaneous pressures were experienced when this rocket engine was started under simulated high altitude conditions using hypergolic bipropellants. These hard starts did not occur on every occasion, but rather randomly at various peak pressures. On occasion, these transient ignition overpressures have been large enough to damage the rocket engine combustion chamber due to the resulting very high strain and strain rates experienced by the chamber material and coating system.

The Marquardt Corporation received from NASA Manned Spacecraft Center, Houston, Texas on 1 July 1965 a seven and one-half months contract for "Investigation of High Strain Rate Behavior of Refractory Alloys and Coatings" (NAS 9-4905). The objective of this investigation was to evaluate selected refractory alloys, both coated and uncoated, under the environmental and loading conditions that a rocket engine would be subjected to as a result of an ignition pressure spike. These investigations were to generate significant high strain rate data, establish engineering and design criteria, and materially assist in future engine combustion chamber improvements.

The selection of material systems for refractory metal rocket combustion chambers is normally based primarily upon strength and oxidation resistance characteristics. In this study, laboratory experiments with specimens of various material systems and hydrodynamic tests with full scale combustion chambers were used to extend the selection criteria to include the effects of single and repeated high dynamic strains.

II. SUMMARY

Material and coating systems investigated in this program are shown in the following Table A. The systems are for use in a rocket combustion chamber intended to operate within the temperature range -100°F to 2500°F.

TABLE A

MATERIAL AND COATING SELECTION SUMMARY

Material System	System Description	Why Chosen
90Ta-10W Substrate	90% Tantalum-10% Tungsten	Basic high strength tantalum alloy with high temperature capability.
and		
R512 Coating	Slurry applied disilicide + vacuum diffusion	No embrittling interstitial gases introduced into substrate during coating application.
C-103 Substrate	Hf-10%, Ti-1%, Zr-1%, Cb-Balance	TMC experience with this alloy shows good ductility and high strength to 2500°F.
and		
Durak KA Coating	Pack cementation applied disilicide plus thermal conditioning	High temperature capability in oxidizing atmosphere and some TMC experience.
or		
W + R508C Coating	Vapor deposited tungsten plus vacuum diffused aluminide	Tungsten provides barrier from products of combustion. Ductile aluminide coating protects the tungsten from oxidizing.
C-129Y Substrate	W-10%, Hf-10%, Cb-Balance	Highest strength/weight ratio of Cb alloys with good ductility to 2500°F.
and		
Durak KA Coating	Pack cementation applied disilicide	High temperature capability in oxidizing atmosphere and some TMC experience.
Molybdenum Substrate	Unalloyed molybdenum	Control specimen - same system used on Apollo Service Module Reaction Control Engine.
and		
Durak B Coating	Pack cementation disilicide	

Laboratory tests were performed on tensile specimens of these alloys in both uncoated and coated conditions to determine the effect of each coating on its substrate under both slow and high strain rate performance. Slow strain rate testing was conducted at -100°F, room temperature and 2500°F. High strain rate performance was evaluated at -100°F and R.T. using special, high speed tensile testing equipment which produced strain rates at equivalent order of magnitudes as that experienced by chamber wall material during maximum combustion ignition pressure conditions.

Tensile tests were also conducted subsequent to vacuum-thermal cycling and exposure of coated samples to 15 percent and 30 percent hydrogen levels, to evaluate the coating vacuum sublimation and substrate embrittlement, respectively. Fatigue torch testing of coated specimens was also conducted. Bend tests were performed on uncoated and coated specimens in the "as received" condition and on those which were previously fatigue-torch tested. Table B, Page 6, is a summary listing of the laboratory test specimens and test parameters.

Hydrodynamic tests utilizing a special Marquardt designed hydraulic rig were conducted on full-size chambers of the Apollo Service Module Reaction Control Engine (SMRCE) configuration to evaluate biaxial loading (axial and circumferential) conditions. (The laboratory tests included uniaxial loading only). These hydrodynamic tests simulated the rapid pressure rise rates experienced on actual engine firing. They produced maximum chamber pressure rise rates of 180 to 250 psi/microsecond as measured by a Kistler pressure transducer and chamber peak pressures to 15,000 psi (as recorded by strain gages). These compare to 150 to 250 psi/microsecond pressure rise rates and peak pressures to 6000 psi measured on engine firings.

Table C, Page 8, presents the test results of all the materials and materials systems evaluated (see Summary discussion). The ultimate strength performance of ductile materials, coated and uncoated, tested at high strain rates, was found to be 50 to 100 percent higher than strength values obtained under slow strain rate conditions. The material ductility was generally not affected. Testing of molybdenum (the control specimen material) reconfirms published data as well as previous Marquardt test data as to the brittle characteristics resulting from high strain at room temperature and slow strain rate at -100°F.

The results of the test program on both specimens and chamber testing as to the capability of the candidate materials to respond to high strain rate at -100 and R.T. conditions are concluded below:

1. Good strength and ductility resulted under high strain rate loading for C-103 for tensile, bend and full scale chamber testing; this alloy is considered to be an important candidate as a chamber back-up material.

2. Good strength and reasonably good ductility for C-129Y material systems was recorded. However, C-129Y was not thermally conditioned to maximize the ductility and no biaxial chamber testing was performed to conclude as to the C-129Y capability in this area. Bend test results indicated relatively poor ductility (an extreme test). However, it is felt that because of the superior strength/weight ratio of this alloy and the probability that high ductility could be restored with thermal conditioning similar to that given to C-103, C-129Y should still be considered as an important candidate for future evaluation.

3. 90Ta-10W materials system exhibited good strength and ductility with tensile specimens and full scale chamber testing. However, the results of bend testing after torch exposure showed an appreciable loss of ductility. This could be the result of embrittlement caused by interstitial gas penetration through the coating, or the result of non-optimum coating conditions. High bend ductility was obtained at -100°F with no pre-torch exposure. Good coating life was obtained (2900°F for one hour vs. 2650° for two hours for the columbium alloys), and from this aspect and the high strength and ductility

properties under high strain rate, this material should also be considered as a candidate back-up material. However, because of its high density and post-torch embrittlement, this material is considered somewhat inferior to the columbium alloys.

4. The R-508W coating on C-103 substrate is rated low because this aluminide showed a tendency to sublimate and/or outgas during the vacuum thermal cycle. All other coatings tested indicated good oxidation resistance and that none of them tend to degrade the performance of its substrate.

TABLE B

LABORATORY TEST PARAMETERS

	Slow Strain Rate			High Strain Rate					Bend	Fatigue	Fatigue-Torch
						Temp. Cycle and Vacuum Exposure	H_2-Thermal Exposure				
	-100°F	R.T.	2500°F	-100°F	R.T.	-100°F	15% -100°F	30% -100°F	-100°F	R.T.	
Molybdenum	X	X	X	X	X				X	X	
Molybdenum/ Durak B	X	X	X	X	X	X	X	X	X	X	
90 Ta-10W	X		X	X	X				X		
90 Ta-10W/ R512	X	X	X	X	X	X	X	X	X		X
C=103	X		X	X	X						
C-103/ Durak KA	X	X	X	X	X	X	X	X	X		X
C-103/ W + R508C	X	X	X	X	X	X	X	X	X		X
C-129y	X	X	X	X	X				X		
C-129y/ Durak KA	X	X	X	X	X	X	X	X	X		X

III. RESULTS AND CONCLUSIONS

A. Results

1. Laboratory Testing

Table C is a summary of the material ultimate strength and elongation characteristics determined from the laboratory tests with material specimens.

a. Molybdenum/Durak B

Test results reconfirm both published data and TMC test data previously performed during the development of Apollo SMRCE chamber. These results showed that at slow strain rate, partially recrystallized material (as-coated condition) has high ductility, however, the ductility decreases rapidly as:

(a) The degree of recrystallization increases

(b) The temperature decreases

(c) The strain rate increases

b. 90Ta-10W/R512

At -100°F, this alloy, coated or uncoated, is capable of 180° bends without fracture. The elongation at -100°F tensile tests was 20 percent in the coated condition, and the strength was over 100,000 psi. At 2500°F, the coated material had the highest tensile strength of any metal-coating combination tested. There is some question as to the capability of the coating system to act as a barrier in preventing interstitial gas penetration into the substrate. This was evidenced by bend testing specimens which had been previously exposed to torch tests where low bend angles were observed. The torch life at 2900°F was approximately one hour.

Strengths obtained during high strain rate tests were 50 to 70 percent higher than those obtained during slow strain rate tests. High strain rates produced no loss in ductility. Neither hydrogen exposure or vacuum-thermal cycling had a detrimental effect on high strain rate values.

TABLE C

TYPICAL ULTIMATE STRENGTH/ELONGATION TABLE - KSI/PERCENT

Material Coating	Density	Slow Strain Rate			High Strain Rate				
	lbs/in^3	-100°F	R.T.	2500°F	-100°F	R.T.	Vacuum Thermal Cycle -100°F	15% H_2 -100°F	30% H_2 -100°F
Molybdenum Durak B	.369	*92/0	*80/27	*8/8	*73/4	*80/1	**70/1	*74/0	*68/0
90 Ta-10W R512	.607	110/20	92/25	23/20	181/24	160/26	177/25	200/22	171/24
C-103 Durak KA	.320	79/21	62/28	10.5/18	119/23	141/30	121/24	117/22	114/22
C-103 W + R508C	.320	88/18	68/18	12/3	140/16	130/23	150/18	168/17	153/19
C-129Y Durak KA	.343	102/21	86/21	17/14	151/16	151/25	177/18	172/16	182/15

Slow Strain Test Speed - .005 in/in/min to .2 percent yield (elastic strain)
.05 in/in/min to ultimate (plastic strain)

High Strain Test Speed - 100 to 250 in/in/sec (elastic strain)
500 in/in/sec (plastic strain to ultimate stress)

* Partial recrystallization as a result of coating application

** Additional recrystallization as a result of thermal conditioning

c. Columbium C-103

This material was tested with two coatings; one, Durak KA, and the other, a vapor deposited tungsten layer followed by R508C, aluminide. The Durak KA coated specimens were given a 2500°F, 2-1/2 hour, air, thermal conditioning treatment after coating. Both coatings gave 180° bends at -100°F. At -100°F, when compared to uncoated specimens, both coatings showed small loss of tensile ductility, and increase in strength. At 2500°F both coatings caused little or no loss of strength; but based on only one test sample, the W + R508C caused a severe loss in ductility. In torch testing at 2650°F, the Durak KA coating showed degradation in less than 120 minutes, while the W + R508C coating looked satisfactory after 120 minutes, when tests were discontinued.

Strengths obtained during high strain rate tests of specimens coated with either coating were 50 to 100 percent higher than those obtained during slow strain rate tests. High strain rates produced only small losses in ductility. No effect was noted on strength or ductility due to H_2 or vacuum exposure.

d. Columbium C-129Y/Durak KA

The Durak KA coating used on this alloy was the same as was used on C-103. However, no postcoating thermal conditioning treatment was used as was in the case of C-103. Since thermal conditioning of the coated alloys to restore ductility must be done at high temperature to outgas any embrittling interstitial gases (mainly hydrogen) it was felt that a penalty in coating life would result. It was therefore desirable to evaluate the ductility characteristics of one columbium material system without thermal conditioning. C-129Y was chosen. Brittle tendencies were noted that could probably have been removed by the thermal conditioning treatment.

The bend ductility at -100 F was low (20 to 55°, 4T bend radius). The coating had little effect on the strength or the elongation at all temperatures. It had the highest strength/density of any of the alloys tested. The Durak KA coating showed signs of degradation in less than 120 minutes at 2650°F during torch testing.

The high strain rate tests showed increases over slow strain rate tests of 50 to 80 percent in strength and decreases of 25 percent in elongation.

2. High Strain Rate Experiments with Full Scale Combustion Chambers

Table D is a summary of the design data obtained from high strain rate specimen testing. These stresses were induced into full scale combustion chambers by hydrodynamic techniques. A total of nine chambers was tested after checkout of the test rig. Tests of a ductile stainless steel combustion chamber indicated the hydrodynamic test setup could simulate pressure maximums and pressure rise rates of the same magnitude as those experienced on engine firing. Further evidence of the suitability of the hydrodynamic rig was obtained by comparing the stress levels induced into the chamber walls with the results obtained from the high strain rate tests. The comparison showed a consistency in the material performance.

Three molybdenum chambers coated with Durak B manufactured and processed exactly like the Apollo SMRCE chambers were hydrodynamically tested. These chambers fractured in a brittle fashion between 3700 to 6700 psi pressure at pressure rise rates on the order of 180 to 250 psi/microsecond. Photographs of these fractured chambers showed a similarity to chambers that had failed during engine firing tests.

TABLE D

HIGH STRAIN RATE ULTIMATE TENSILE STRENGTH AT ROOM TEMPERATURE (SPECIMENS)

Elastic Strain Rate ≅ 100-200 in/in/sec
Plastic Strain Rate ≅ 500 in/in/sec

Material/Coating	Ultimate Stress (psi)
Molybdenum/Durak B	75 - 85,000
90 Ta-10W/R512	154 - 165,000
C-103/Durak KA	137 - 148,000
C-103/W + R508C	121 - 136,000

Two 90 Ta-10W/R512 chambers withstood 15,000 psi chamber pressure at 150 to 250 psi/microsecond pressure rate and experienced 0.0046 inch/inch dynamic strain without failure. Photomicrographs showed no flaking or peeling of the coating. These chambers were subjected to a minimum of five pulses and as high as ten pulses above 5000 psi with no detrimental effects.

Two C-103/Durak KA chambers behaved similarly to the tantalum chambers in all respects.

Two C-103/W + R508C aluminide chambers were similarly tested and results were again similar. However, physical changes were noticed on the chamber. These changes could be attributed to two possibilities:

(1) Due to the dynamic pulses imposed on the chamber, the soft eutectic on the aluminide flaked off.

(2) The mercury (used as the fluid in the chamber) attacked the aluminide.

In examining photomicrographs of tensile specimens exposed to 10^{-4} torr at 2500°F, the aluminide coating showed a tendency to outgas or sublimate. If this coating were on an engine in space, the aluminide coating might sublimate or outgas completely, exposing the tungsten to the products of combustion. Tungsten is not a good oxidizing material and would oxidize rapidly, subsequently exposing the substrate to the embrittling combustion gases.

C-129Y/Durak KA was not tested in the chamber configuration; the contract provided only for the nine chambers tested. However, extrapolation of the C-103/Durak KA data to approximate C-129Y/Durak KA performance appears reasonable when based on results of the laboratory tests with both these material systems.

A qualitative comparison of all materials at each test condition is presented in the following chart. Based on test results obtained, the best performance is rated 3, intermediate performance 2, and lowest performance 1. An overall average is also provided. This chart is for generalized comparison only, since no particular values were assigned to each column rated.

COMPARISON OF ALL MATERIALS EVALUATED

Rating Scale:

Best Performance - 3
Intermediate Performance - 2
Lowest Performance - 1

Material Coating	Strength/Density Ratio							Bend Ductility	Oxidation Resistance (Torch-Fatigue)	Full Scale Chamber Testing	Average Performance
	Slow Strain Rate .005-.05 in/in/min			High Strain Rate 100-500 in/in/sec							
	-100°F	R.T.	2500°F	-100°F	R.T.	Vacuum-Thermal Cycle -100°F to 2500°F	H_2 Thermal Exposure -100°F				
Moly/Durak B	1	3	1	1	1	1	1	1	Not Tested (a)	1	1.4
90Ta-10W/R512	1	1	2	2	2	2	2	2	2	3	1.9
C-103/Durak KA	2	2	1	3	3	3	3 (d)	3	2	3	2.5
C-103/W + R508C	2	2	2	3	3	1 (c)	3	3	3	1 (c)	2.3 (c)
C-129Y/Durak KA	3	3	3	3	3	3	3	2	2	Not Tested (b)	2.8

(a) Apollo data shows good oxidation resistance to ≅ 3000°F
(b) Data extrapolated from laboratory testing shows highest performance
(c) No effect on mechanical properties; but coating did not stay on through test
(d) Two of four specimens tested failed brittle-embrittlement may have resulted from pinholes on coating.

B. Conclusions

1. All ductile materials which were evaluated in this program demonstrated high strength and ductility under high strain rate induced loads, therefore, they would be considered suitable for combustion chamber materials.

2. The high strain rate tensile testing machine can be a valuable tool in the evaluation of materials for rocket combustion chamber use; the machine developed strain rates in the test materials which approximate those experienced by combustion chambers as a result of ignition spikes.

3. The ductile materials exhibited a 50 to 100 percent increase in ultimate strength when tested at high strain rates as compared to slow strain rates. Ductility for these materials was not generally affected by change in strain rate.

4. It is considered that the 90Ta-10W tantalum tungsten material system is somewhat inferior to the columbium, (C-103 and C-129Y material systems) mainly because of its higher density and lower bend ductility properties after fatigue-torch testing.

5. The columbium material system (C-103 and C-129Y with Durak KA) demonstrated high capability under high strain rate conditions. C-129Y showed superior strength/weight and somewhat inferior ductility. Oxidation resistance was about equal for the two alloys. Although pin holes were observed in some C-103 torch disks, it is felt that improvement in the coating application technique would eliminate this condition. The C-103 demonstrated capability to withstand high biaxial stresses during the full scale chamber testing. C-129Y was not tested in this mode, however, when comparing tensile test results, it would indicate that it was also capable of withstanding the biaxial chamber test loads.

6. Molybdenum exhibited insignificant change in its ultimate strength when tested at high strain rates. It demonstrated brittle characteristics under high strain rates at R.T. and -100°F.

7. None of the coatings appeared to affect their substrate properties.

8. The hydrodynamic testing technique used in this program was shown capable of simulating some of the critical stress conditions imposed on rocket combustion chambers by ignition spikes. As such, it may be used as a tool for the preliminary evaluation of material systems for rocket combustion chambers. The extent of simulation is limited, and does not preclude the eventual requirement for evaluation by full scale rocket test firings.

IV. RECOMMENDATIONS

Recommendations derived from the experience gained under this program are separated into three categories. The first set of recommendations outlines work which is considered important in the search for a suitable back-up to the recently qualified Service Module RCS Engine (SMRCE) combustion chamber. The second set concerns materials and coatings which would support requirements for advanced engine designs requiring a temperature higher than the 2500°F maximum established for this program. The third set describes recommended improvements to the hydrodynamic evaluation technique.

A. Recommendations for SMRCE Backup

1. C-129Y chambers coated with the Durak KA disilicide should be evaluated in firings of full-scale engines. This material system showed the best performance of the several evaluated under this program. The firing tests recommended should include both fatigue (i.e., repeated ignition spike testing) and endurance runs. C-103, also coated with Durak KA, could be an alternative to C-129Y.

2. Conduct full-scale firing test with combustion chambers made of C-129Y coated with several coatings not tested under this program, but which have been reported in the open literature to be satisfactory. This program has, to a reasonable degree, demonstrated that the ductility obtainable with columbium alloys is suitable for ignition spike containment. However, the number of coatings evaluated was limited.

The additional coatings which should be evaluated in the fatigue and endurance mode are the R512 slurry disilicide, and the Ti-Cr-Si ternary system. Again, C-103 could be an alternate to C-129Y.

3. Columbium materials not tested under this program, but reported satisfactory in the open literature include SCb 291 and Cb 752. These materials and the coatings listed above are recommended for comparative firing evaluation.

B. Recommendations for Advanced High Temperature Engines, (i.e, Over 2500°F)

1. Conduct full-scale firing tests with 90Ta-10W/R512. This system demonstrated a high level of performance in the numerous tests conducted under this program. Although its performance did not equal that of the columbium alloys at the 2500°F level, at higher temperatures, it possesses a higher strength/density ratio than the columbium alloys. Also, reasonably satisfactory performance was noted during torch tests at 2900°F.

2. Extend the search for materials and coatings with capabilities to include temperatures ranging up to 3200°F instead of the 2500°F limitation used in the current program. This search should include analysis, laboratory tests with material samples, and hydrodynamic tests with full-scale chambers.

3. Conduct full-scale firing tests to evaluate the spike resistance characteristics and endurance abilities of those other coatings and substrates determined sutiable as a result of the above-recommended laboratory and hydrodynamic tests.

C. Recommendations for Improved Methods of Evaluation

1. Further exploit the hydrodynamic test rig by evaluating advanced material systems in a fatigue testing mode. Minor mechanical additions to the test rig could make possible fatigue tests wherein the spike load is repeated several times per minute.

2. Extend the test rig to simulate asymmetrical loading. The combustion process in full-scale engines is not symmetrical, and therefore, the degree of simulation accomplished with the current test rig is restricted.

3. Computerize the stress analysis of the hydrodynamic setup so that better definition of the stress pattern inside the combustion chamber may be obtained.

V. TECHNICAL DISCUSSION

The program was conducted in three major phases:

1. Phase I - Analysis and Selection of Material and Coating System
2. Phase II - Laboratory Studies
3. Phase III - High Strain Rate Chamber Experiments

A. Phase I - Analysis and Selection of Material and Coating System

1. Analysis

The following design criteria were established to guide the selection of materials and coatings for evaluation during Phase I:

a. Maximum wall temperature 2500°F
b. Minimum wall temperature -100°F
c. High strain rate of 167 in/in/sec

The maximum chamber temperature of 2500°F was selected because test data on the Apollo Service Module Reaction Control System Engine (SMRCE) has indicated that relatively high performance radiation-cooled rockets can be designed to operate at or below this temperature.

Inasmuch as the SMRCE engine was contractually designated the configuration to be tested, this 2500°F limitation was deemed more appropriate than those higher temperatures identified with other engine designs. This lower limitation made possible a wider range of materials and coatings from which to choose.

The selection of -100°F was based on the estimated temperature of the SMRCE chamber at altitude conditions.

The results of full-scale static firing tests with stainless steel chambers made to the SMRCE engine configuration were evaluated to establish the strain rate requirements for the laboratory and full-scale testing phases. Analysis of the combustion chamber vacuum ignition pressures recorded during these tests indicate the following:

(1) Pressures are maximum at hard vacuum, cold propellants, and cold chamber wall conditions when the oxidizer flow leads fuel flow in the approximate range of 3 to 20 milliseconds.

(2) Experiments with nonrefractory alloys such as stainless steel and L-605 have shown that under high pressure rise rate loading, these materials absorbed the energy through slight yielding or plastic deformation.

(3) These pressure pulses have been measured by both "Kistler" pressure transducers and recorded on oscilloscopes with Polaroid cameras, as well as strain gages which had been calibrated under static pressure conditions. These data showed that for the higher ignition overpressures, the strain gages read pressure values approximately twice those obtained with the Kistler. This indicates that nonsymmetrical bending stresses under violent combustion conditions are superimposed on average pressure stresses and/or a dynamic effect takes place based on the interaction of pressure rise rate and peak time with chamber wall material frequency in bending and circumferential stress modes.

(4) These maximum pressure rise rates are approximately 150,000 to 250,000 psi/ms as recorded on Kistler transducers while the strain gages show equivalent pressure rise rates of 300,000 to 500,000 psi/ms.

Based on these data, the 167 in/in/sec strain rate design criterion is derived below.

$$\text{Stress (S)} = \frac{pr}{t}$$

and

$$\text{Stress Rate } (S_T) = S/T = \frac{p}{T}\frac{r}{t}$$

where:

p = pressure rise - psi
p/T = pressure rise rate = psi/sec
r = combustor radius = 1.0 in.
t = average combustor wall thickness = 0.10 in.

$$\text{Stress Rate } (S_T) = 10\ (p/T)$$

$$\text{Strain (e)} = \frac{S}{E} = \frac{10p}{E}$$

where E = Modulus of Elasticity

$$\text{Strain Rate } (e_T) = \frac{e}{T} = \frac{S}{TE} = \frac{S_T}{E} = \frac{10}{E}\frac{p}{T}$$

For the L-605 chamber:

$E = 30 \times 10^6$ psi and $P/T = 500{,}000 \times 10^3$ psi/sec

therefore, $$\text{Strain Rate } (e_T) = \frac{10}{E}\frac{p}{T} = \frac{10 \times 500{,}000 \times 10^3}{30 \times 10^6} = 167 \text{ in/in/sec}$$

All tensile specimens were high speed tested at approximately 167 in/in/sec, from the L-605 strain rate derived above. To permit direct comparison, it was assumed the material response rate for all chambers, regardless of material, will be the same as the maximum strain rate measured in the Apollo stainless steel spike test program.

2. Materials and Coatings Selection

a. The materials which were eventually selected for test evaluation are listed below:

Material	
90 Ta-10W	Basic tantalum alloy (TA-90%, W-10%)
C-129Y	Advanced Columbium alloy (W-10%, Hf-10%, Cb-bal)
C-103	Basic Columbium alloy (Hf-10%, Ti-1%, Zr-1%, Cb-bal)
Molybdenum	Unalloyed molybdenum control for comparison (this is the SMRCE chamber material)

The Marquardt Corporation in early 1964 selected 90 Ta-10W as a backup material for the Apollo SMRCE combustion chamber. A series of tests was conducted, but these tests strongly indicated that disilicide coated 90 Ta-10W was severely embrittled by the coating, and therefore could not contain the high impact load. However, Solar Aircraft Company, under Air Force Materials Laboratory Contract RTD-TDR-63-4006, "Evaluation of Coated Refractory Metal Foils," showed partial recovery of disilicide coated ductile substrate properties after thermal conditioning (in air) at 2000°F for 8 hours. This opened up a new field for selecting refractory alloys such as columbium and 90 Ta-10W, with high strength for high temperature potential.

Further evidence of the suitability of these refractories was gained under a Marquardt-funded effort. Test investigation showed ductility could be restored to thin round discs of C-103, C-129Y, or 90 Ta-10W coated with disilicide coatings.

These columbium alloys (C-103 and C-129Y) and the tantalum alloy (90 Ta-10W) were selected for further evaluation on this program based on their strength/density ratio at 2500°F, ductility, repeatability and procureability. Table E summarizes all of the materials considered, and the many factors which led to the final selection listed above.

TABLE E

MATERIALS SUBSTRATE EVALUATION FOR PHASE II TESTING

Primary Material	Alloy	Advantages	Disadvantages	Remarks
Tantalum	1. 90 Ta-10W	1. Readily procurable 2. Easily fabricated 3. Compatible coatings 4. TMC experience background	1. High density (0.607 lb/cu.in.) 2. Coated material requires outgassing of interstitials H_2, O_2, N_2	1. Recommended for high strain rate evaluation
	2. T-111	1. High strength above 2000°F 2. Can be procured, fabricated and coated	1. High density (0.604 lb/cu.in.)	1. Not recommended - no significant advantage over 90 Ta-10W
	3. T-222	1. Extra strong Ta alloy 2. Maintains good strength to 3500°F 3. DMIC 189 reports good fabricability	1. Procurement difficulty 2. High density 0.604 lb/cu.in. 3. Lack of coating history	1. Recommended for high strain evaluation- if procurable
Columbium	1. C-103	1. Readily available 2. Easily fabricated 3. Compatible coatings 4. Good TMC experience 5. Low density 0.320 lb/cu.in. 6. Good ductility	1. Limiting strength factor above 2500°F 2. Thermal conditioning required after coating	1. Recommended for high strain rate evaluation

TABLE E (Continued)

Primary Material		Alloy		Advantages		Disadvantages		Remarks
Columbium (continued)	2.	C-129Y	1.	High strength Cb alloy 22,000 psi at 2500°F	1.	Thermal conditioning required after coating (not optimized)	1.	Recommended for high strain rate evaluation
	3.	Cb752	1.	Available and readily fabricable	1.	Repeatable properties difficult to achieve	1.	Not recommended - because of lack of reliable data
	4.	FS85	1.	Available and readily fabricable			1.	Not recommended - no significant elevated temperature strength advantage over C-103 and exhibits less strength than C-129Y
	5.	Scb291	1.	Available and readily fabricable	1.	Typical data shows C-129Y and Cb752 with higher strength		
			2.	Comparable to C-103 and C-129Y in physical properties				

TABLE E (Continued)

Primary Material	Alloy	Advantages	Disadvantages	Remarks
Molybdenum	1. TZM	1. High recrystallization temperature (2650°F) 2. High strength M_o alloy 3. Fabricable 4. TMC experience	1. Lack of ductility at low temperatures 2. Temperature limited by coating capability; i.e., must be used below 2600°F	1. Recommended for high strain rate evaluation due to high recrystallization temperature which theoretically should leave material in cold worked condition after coating
	2. 1/2Ti Moly	1. Higher recrystallization temperature than moly (2400°F) 2. Good TMC experience 3. Fabricable	1. Brittle at low temperatures 2. No significant advantage over moly	1. Not recommended - operational temperatures would recrystallize the substrate resulting in little or no advantage over unalloyed moly
	1. Hf-Ta	1. Excellent potential for oxidation resistance to 4000°F	1. Availability 2. Lack of design data	

b. Coatings selected for the above materials are:

(1) Durak B (disilicide - pack cementation) for molybdenum - this is the SMRCE chamber material system.

(2) Durak KA (disilicide - pack cementation) for Columbium alloys (C-103 and C-129Y).

(3) Sylcor R512 (disilicide - slurry + vacuum diffusion) for 90 Ta-10W

(4) W + Sylcor R508C (vapor deposited tungsten covered with an aluminide) for Columbium C-103

The selection of Durak KA on Columbium alloys C-103 and C-129Y was most logical because of its proven high temperature capability in an oxidizing environment.

The brittle characteristics induced into the substrate as a result of the coating process may be removed by thermal conditioning. Based upon experience with Durak B there was no indication that the brittle nature of this coating would be too restrictive on overall material system performance.

The selection of vapor deposited tungsten plus Sylcor R508 on C-103 was made to permit comparison of the relative properties of a brittle verses a ductile protective coating. The Sylcor R508C is an Ag-Si modified aluminide which is relatively ductile, and was selected as being the most promising high temperature ductile coating. The tungsten plus R508C coating description indicates that a barrier coating of tungsten (0.002 in.) will be applied (vapor deposition) prior to vacuum diffused aluminide. This barrier is applied to retard or preclude interstitial gas penetration under operational conditions.

R512 was selected for 90 Ta-10W because it would provide data on a disilicide process alternate to the Durak KA pack cementation. R512 is a slurry applied disilicide followed by a high temperature vacuum diffusion. The latter process both builds up a diffusion barrier at the substrate interface and drives out the coating induced embrittling interstitial gases.

Original plans for 90 Ta-10W were to coat it with a fluidized bed disilicide. This coating process does not induce embrittling gases into the substrate and exhibits satisfactory oxidation resistance characteristics. However, further investigation established that neither of the coating vendors who apply this coating were willing to undertake the coating of an SMRCE combustion chamber; the coating process had not been developed sufficiently beyond the flat plate application stage.

The table provided in the Section II Summary recaps the material systems tested, system descriptions, and reasons for their selection.

As previously stated, the Durak B on molybdenum is the same process used on the SMRCE engine.

Table F summarizes the coatings and considerations which led to the final coating selection.

B. Phase II Laboratory Testing

The materials, coatings and test parameters were investigated as previously shown in Table B, Page 6.

1. Results of laboratory tests can be summarized as follows:

   a. Slow Strain Rate

      (1) The uncoated columbium and tantalum-tungsten materials were ductile within the range of test conditions. Molybdenum exhibits brittle characteristics at -100°F; or if thermally conditioned, at 2150°F for one hour.

      (2) None of the coatings altered the substrate characteristics to a major extent.

   b. High Strain Rate

      (1) All molybdenum specimens had zero to 6 percent elongation and exhibited brittle failure. Strength values were scattered and lower than those from slow strain rate tests.

(2) Ductile materials (uncoated and coated columbium and tantalum) had 50 to 100 percent greater strengths than at slow strain rates. Except for uncoated C-129Y at -100°F, elongation was between 14 to 34 percent, similar to slow strain rate results. The elongation of C-129Y at -100°F was significantly lower, ranging from 3 to 8 percent* versus slow strain rate elongation values of 17 to 25 percent.

(3) No noticeable change in the ultimate strength was observed on any of the materials due to vacuum or hydrogen exposure except for C-129Y, which had a slight increase. These exposures did not affect elongation.

c. Bend Tests

Coatings adhered to substrates during bend tests of 20° and more (or until failure of the substrate in the case of molybdenum).

d. Torch and Fatigue-Torch Tests

The nonmolybdenum specimens, except for the C-103 coated with W + R508C, exhibited coating degradation after one or more hours of torch testing at 2650°F.

---

*This condition may be attributed to the material being contaminated.

TABLE F

REFRACTORY COATINGS EVALUATION FOR PHASE II TESTING

Type of Coating	Advantages	Disadvantages	Remarks
1. Aluminides Examples R505C-GT & E NAA85 - North American	1. Slurry applied 2. Low temperature vacuum diffuesd 3. No coating contaminants 4. High temperature capability	1. Need improvement in vapor pressure behavior in vacuum 2. Erosion resistance due to coating fluidity at elevated temperature needs improvement 3. Unknown resistance to H_2 penetration	1. Not recommended
2. Tungsten + Aluminide R508C - Sylcor	1. Relatively ductile 2. High temperature capability 3. "W" prohibits interstitial gas penetration	1. Same as No. 1 & 2 for Aluminides	1. Backup for fluidized bed process.
1. RM055	1. Relatively easy to apply 2. High temperature capability	1. Unpredictable	
Disilicide Processes			
1. Pack Cementation a. Molybdenum & Moly alloys Examples Durak B PFR6	1. Consistent 2. High temperature capability in oxidizing environment 3. Integral bond with substrate 4. Large background of experience at TMC	1. Brittle 2. Limited thermal data in vacuum	1. Recommended - proven history of capability

TABLE F (Continued)

Type of Coating	Advantages	Disadvantages	Remarks
b. Tantalum Alloys Examples Durak MGF PFR50	1. Consistent 2. Same 3. Same 4. Some background of experience at TMC	1. Brittle 2. Embrittles substrate 3. Thermal treatment required to outgas interstitials	1. Not recommended - too much development work on thermal cycling required
c. Cb Alloys Example Durak KA	1. Same as a and b	1. Same as in lb.	1. Recommended - cycling after coating improves capability
2. Slurry Applied (Vac. Diffused) Sylcor R512 or LTV	1. Uniform coating thickness regardless of design complexity 2. Reduces processing time, therefore, cost 3. Potentially applicable to M_O, Cb, & Ta & their alloys		1. Recommended as a backup to fluidized bed
3. Fluidized Bed Example Boeing Disil & Pfaudler Corp.	1. Process precludes embrittling 2. History indicates consistency 3. Integral bond with substrate 4. High temperature capability	1. Coating requires additional development	1. Recommended - appears to be optimum processing procedure

e. Tensile Test Summary

The following table tabulates the average ultimate strengths and elongations at the conditions tested.

ULTIMATE STRENGTH/ELONGATION TABLE - KSI/PERCENT

Material Coating	Density	Slow Strain Rate			High Strain Rate				
	lbs/in^3	-100°F	R.T.	2500°F	-100°F	R.T.	Vacuum Thermal Cycle -100°F	15% H_2 -100°F	30% H_2 -100°F
Molybdenum Durak B	.369	*92/0	*80/27	* 8/8	* 73/4	*80/1	**70/1	*74/0	* 68/0
90 Ta-10W R512	.607	110/20	92/25	23/20	181/24	160/26	177/25	200/22	171/24
C-103 Durak KA	.320	79/21	62/28	10.5/18	119/23	141/30	121/24	117/22	114/22
C-103 W + R508C	.320	88/18	68/18	12/3	140/16	130/23	150/18	168/17	153/19
C-129Y Durak KA	.343	102/21	86/21	17/14	151/16	151/25	177/18	172/16	182/15

Slow Strain Test Speed - .005 in/in/min to .2 percent yield (elastic strain)
.05 in/in/min to ultimate (plastic strain)

High Strain Test Speed - 100 to 250 in/in/sec (elastic strain)
500 in/in/sec (plastic strain to ultimate stress)

* Partial recrystallization as a result of coating application

** Additional recrystallization as a result of thermal conditioning

2. Test Specimen Configuration (Table 1)

a. Tensile

The use of round bar tensile specimens rather than flat specimens was chosen for two reasons:

(1) Bar stock more closely simulates the condition of materials being used to fabricate small rocket engines.

(2) Better high strain rate data is obtained using round tensile specimens. This is because a no-slack specimen-to-grip attachment can best be accomplished using threaded round bars rather than pinned flat specimens.

The standard 1/2-13 UNC thread was used for all slow strain rate test specimens, while a 1/2-20 NF thread was used for the high strain rate test specimens. This finer thread further reduces the slack present in the specimen-to-grip attachment. A 0.125 inch diameter test section was selected to insure failure of the brittle specimens within the reduced section under the high strain rates imposed. Further, 0.125 inch closely approximates the coating-to-substrate dimensional relationship of the SMRCE combustor. A 0.125 inch diameter test section was therefore utilized on all slow strain rate test specimens for direct comparison.

b. Bend

A 1/2 by 2 inch bend specimen was chosen as being adequate to properly accomplish the necessary tests.

c. Fatigue

All fatigue test specimens of molybdenum were manufactured to the same configuration as was used for the slow strain rate tensile test specimens. Normally, this is not possible because fatigue will occur in the test specimen threads. However, the special, small diameter test section chosen for this investigation was also ideally suited for fatigue testing.

d. Fatigue-Torch

The configuration developed for these tests permits a fatigue test followed by a torch test with the same specimen. Torch testing required a minimum hot surface of 2 inches by 2 inches. The fatigue test requires loading holes for application of tension forces. A 3 by 6-inch specimen was designed for these tests. This specimen has the necessary torch test area and the loading holes are placed well outside this test area. It is not desirable to have the loading holes border the test area because the stresses are not uniform around these holes.

3. Materials and Coatings

a. Vendors

The base metals, coating systems, methods of application and coating vendors used in this investigation are listed below.

Material	Coating System and Type		Method of Application	Coating Vendor
Molybdenum	Durak "B"	Disilicide	Pack cementation	Chromizing Hawthorne, California
90 Ta-10W	Sylcor R512	Disilicide	Slurry application	Sylvania Electric Products Hicksville, New York
C-103	Durak "KA"	Disilicide	Pack cementation	Chromizing
C-103	W + R508C	Vapor depositied tungsten + vacuum diffused aluminide		Sylvania
C-129Y	Durak "KA"	Disilicide	Pack cementation	Chromizing

The Durak "B" coating on molybdenum was applied in accordance with Marquardt Process Specification, MPS-519. This is the same specification used for the SMRCE. The Sylcor R512 coating on 90 Ta-10W was 0.0025 ± 0.0005 inch thick. The W + R508C coating applied to C-103 was 0.0020 to 0.0025 inch thick tungsten per side plus 0.0035 inch thick maximum R508C per side. The Durak "KA" coatings were applied according to vendor proprietary practice as to thickness.

The overall increases in specimen sizes, due to coatings, are listed in Table 2.

b. Thermal Conditioning

After coating, all molybdenum test specimens were "smoke checked," 2 cycles, at 2000°F for 5 minutes in air, per cycle. This is in accordance with the applicable Marquardt coating specification, MPS 519, and represents the procedure used for all Apollo SMRCE engine molybdenum combustion chambers. The Durak "KA" coated C-103 test specimens were given a 2500°F, 2-1/2 hour, thermal treatment in air prior to testing. This treatment was previously developed to increase the ductility of the coated C-103. It is believed that the increased ductility is due to interstitial gas removed from the C-103 by the thermal cycle.

4. Test Equipment and Test Plan

a. Slow Strain Rate Tensile

All slow strain tensile tests at room temperature and -100°F were conducted on the Marquardt 60,000-pound Baldwin Universal Test Machine (Figure 1). The -100°F test temperature was obtained by immersion in a dry ice and alcohol mixture. Extensometers attached to the test section of each specimen were used to obtain the strain data at -100°F.

The 2500°F tensile testing was conducted on the Marquardt Elevated Temperature Test Machine (TM-1) (Figure 2). The test temperature is generated by self-resistance heating of the test specimen.

The uncoated specimens were tested in an atmosphere chamber that enclosed the specimen. Argon was used in the chamber to prevent oxidation during the 15-minute hold time and during the actual testing.

The coated specimens were tested in an air atmosphere using a 15-minute hold time before testing.

b. High Strain Rate Tensile

All high strain rate testing was conducted on the Optron Model 900 High Speed Tensile Tester (Figures 3 and 4) by Optron personnel at their facilities in Santa Barbara, California. This tester achieves very high strain rates (up to 60,000 inches per minute) by the hydraulic storage and sudden release of energy through the test specimen.

The load experienced by the specimen during testing is determined by a proprietary load cell which is integral with one of the specimen threaded grips. The unique placement of this load cell is claimed to reduce the errors caused by acceleration forces during testing. The strain is measured by two strain gages attached to each test specimen reduced section.

The -100°F high strain rate tensile tests were conducted using a liquid nitrogen, cryogenic test chamber which is a standard accessory to the Model 900 test machine.

All high strain data were obtained by Polaroid pictures of oscilloscope traces. Figure 5 is an example. Both filtered and unfiltered data were recorded for each test. On the strain trace, the first portion is the elastic strain (e_{el}) and the second portion is the plastic strain (e_{pl}).

The strain gages separate from the specimen after the first few percent of plastic deformation. The strain data are in the form of in/in/sec. The first portion of the load trace is the maximum loading rate (psi/sec) during the elastic portion of the test. The second portion of the load trace is the plastic deformation, ending with specimen failure and the maximum load sustained by the specimen.

The value of E, modulus of elasticity, was assumed to be the same for the high and the slow strain tests. Recent work by Optron has indicated this to be generally the case on both brittle and ductile materials. The limited number of specimens available for this program precluded verification.

The tensile tests using round test specimens were conducted on each metal-coating combination, in accordance with the following table:

	Uncoated		Coated	
	-100°F	R.T.	-100°F	R.T.
No. Tested	3	2	3	2

The test speeds were in the range 100 to 250 in/in/sec. Each tensile test gave the following data: ultimate tensile strength, elongation, and stress rise rate.

Tensile tests were conducted on each metal-coating combination in accordance with the following table:

	Uncoated			Coated		
	-100°F	R.T.	2500°F	-100°F	R.T.	2500°F
No. Tested	2	2	2	2	2	2

The data from the slow strain rate tensile tests include: ultimate tensile strength, 0.2 percent yield strength, and percent elongation. Stress/strain curve data were produced, but not plotted, because of the lack of high strain rate stress/strain curves for comparison.

c. Vacuum Thermal Cycling

After the vacuum thermal cycling described below, four tests were conducted on each metal-coating combination. The specimens were subjected to two vacuum thermal cycles each consisting of: R.T. to 2500°F in two hours, hold at temperature one-half hour, furnace cool to room temperature, remove from vacuum and cool to -100°F, hold at temperature one hour, and finally still air warm to room temperature. After these two cycles, the specimens were tensile tested at -100°F at high strain rates. Data was obtained on ultimate strength, elongation and stress rise rate. The failed specimens were then metallographically checked to determine the effect of the vacuum thermal cycles.

d. Hydrogen-Thermal Exposure

After the hydrogen exposure described below, four tests were run on each metal-coating combination. Thirty percent H_2 - 90 percent A and 15 percent H_2 - 85 percent A atmospheres were used and a one-hour exposure at 1400°F will be performed. Heating and cooling rates were recorded. Tensile tests at -100°F were performed. The failed specimens were metallographically investigated.

High strain rate tensile tests were conducted at -100°F, the most critical spiking temperature, on specimens which had been exposed to varying percentages of H_2 at elevated temperatures.

1400°F is the approximate temperature at which maximum H_2 solubility into the substrate materials occurs. Figure 6 shows the variation of solubility with temperature for various materials.

Thirty percent H_2 was selected on an approximation of the maximum percentage to which the combustor chamber walls will be in direct contact. Two specimens of each material coating combination were exposed to a 15 percent H_2 - 85 percent A atmosphere at 1400°F and two other specimens of each material coating combination were exposed to a 30% H_2 - 70 percent A atmosphere also at 1400°F.

Data obtained from these hydrogen-thermal cycles tests included ultimate strength, and stress rise rates elongation, at strain rates of 100 - 200 in/in/sec.

e. Bend Tests

All bend tests were conducted on the Baldwin Universal Test Machine. A two roller fixture illustrated below was used to hold the specimen during testing. A -100°F test temperature was obtained by immersing the test specimen, fixture and part of the punch and a mixture of dry ice and alcohol.

Four bend tests were conducted for each metal-coating combination, two coated and two uncoated. The first setup is illustrated below:

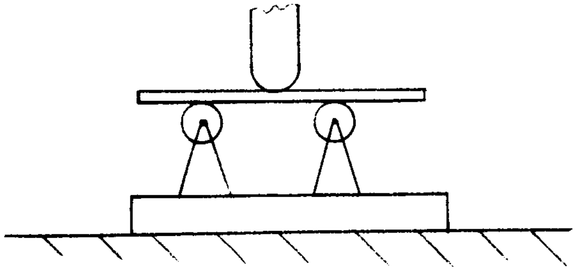

The punch radius was 0.150 inch and a testing speed of 10.0 in/min. was used. The angle at which fracture occurs was recorded and the condition of the coating after testing was determined.

f. Fatigue

Molybdenum specimens, coated and uncoated, were fatigue tested at a + 0.1 minimum to maximum stress ratio at 1800 CPM at room temperature and at -100°F. Tests were conducted on the Model SF-1-U fatigue machine. (Fig. 6).

Endurance limits were obtained for varying loading conditions.

g. Fatigue-Torch

Three each of each coated material, except for molybdenum, were fatigue-torch tested. Molybdenum fatigue specimens were not subjected to torch testing because of the known oxidation resistance qualities of the Molybdenum/Durak B system, gained under the SMRCE development program. All specimens were given an initial fatigue exposure of 10,000 cycles at -100°F.

The torch testing was then conducted in the Marquardt Coated Test Specimen Evaluation Facility, Figure 8. This facility and its standardized test procedures have been developed specifically for materials evaluation studies of coated refractory materials. The results of these tests can be used for direct comparison to past and future work.

All torch tests were conducted using a 10 minute cycle test schedule. This involves a 10 minute continuous exposure to the torch, followed by cooling to room temperature with an air blast. After visual inspection of the coating the next 10 minute exposure cycle is started. Weights of the test specimens before and after testing are recorded.

5. Results and Discussion

a. Slow Strain Rate Tensile Tests

(1) Room Temperature (Tables 3 and 4)

The tensile test results for uncoated molybdenum show very good properties for the as-forged material. However, after thermal conditioning at 2150°F for 1 hour, recrystallization of the material eliminates the ductility and renders the material so brittle that it ruptures before reaching its true ultimate tensile strength. For applications in which the time and temperature do not cause recrystallization, molybdenum can be expected to have excellent ductility and shock resistance when cooled to room temperature. However, the times and temperatures at which molybdenum does not recrystallize are usually so low as to make the material non-competitive with superalloys.

The data in Table 4 indicate that the molybdenum Durak B after coating and smoke checking, has excellent strength and ductility at room temperature. The data developed in this investigation indicate that a treatment of 2150°F for one hour probably causes complete recrystallization and grain growth, resulting in brittle behavior.

The room temperature tensile properties of C-103 coated with Durak KA or W + 508C show KA with a slightly lower strength but higher elongation than W + R508C. The higher W + R508C strength is attributed to the layer of vapor deposited tungsten. The higher Durak KA elongation may be due to the 2500°F, 2 1/2 hour thermal conditioning it receives after coating. The room temperature strength of 90 Ta-10W appeared to be lowered by coating with R512. The Durak KA on C-129Y did not appear to change its room temperature properties.

The slow strain rate data for coated material at room temperature indicate that all of the metal-coating combinations and thermal conditioning treatments tested resulted in good ductilities and could be considered as candidate materials for rocket applications. However, the room temperature data for uncoated material indicates no ductility for molybdenum after exposure to conditions as severe as 2150°F for one hour.

(2) -100°F, Slow Strain Rate (Tables 5 and 6)

Except for the molybdenum, all of the metal-coating combinations tested indicated excellent performance values.

The recrystallization uncoated molybdenum (one hour at 2150°F) behaved in a very brittle fashion, and did not reach 0.2 percent offset during any tensile test. This behavior indicates a very brittle material comparable to gray or even white cast iron. The energy absorption to rupture is very low due to the limited strain prior to failure. The -100°F test environment caused an increase of approximately 20 to 25 percent in the strength of the uncoated 90 TA-10W without any significant loss of ductility. The ductility and strength of the C-103 also remained high at -100°F.

The tensile properties of the coated molybdenum at -100°F show no ductility and no yield strength. Ultimate strength is surprisingly high with only moderate scatter.

The tensile properties of the coated 90 Ta-10W show a nominal loss of strength and elongation when compared to the same material uncoated. Both C-103 with Durak KA or W + R508C show similar or increased strengths as compated to the same material uncoated. Elongations are only slightly lowered by the coatings. C-129Y coated and uncoated, has similar properties at -100°F, however, larger than normal scatter exists in the coated tensile data.

(3) Slow Strain Rate, 2500°F (Tables 7 and 8)

All metal-coating combinations tested show usable strengths and ductilities at 2500°F with the coated molybdenum having the lowest strength and the 90 Ta-10W having the highest strength. However, 90 Ta-10W loses a considerable portion of its advantage due to its high density. A problem may exist with low ductility for C-103/W + R508C.

Both the uncoated and coated molybdenum show elongations of 5 to 9 percent and moderate strength values at this test temperature.

The strength and elongation exhibited by 90 Ta-10W/R512 are over twice as great as those shown for coated molybdenum. However, on a strength to density basis, these advantages are considerably reduced.

Coated C129Y has about twice the strength and elongation as coated molybdenum at 2500°F.

The strength properties of C-103 with a Durak KA coating or a W + 508C coating are somewhat greater than coated molybdenum. The W + R508C appears to have lowered the C-103 elongation. (Only one test was completed on this combination).

The coating processes have caused only slight changes in the tensile properties at 2500°F when compared to the uncoated properties.

b. Bend Tests at -100°F (Tables 9 and 10)

The uncoated test specimens of molybdenum had bend angles of 0 - 4°. This brittle behavior is consistent with the tensile properties without rupture. The 90 Ta-10W did not develop any visible cracks after being bent 180° over a 0.150 inch diameter punch, but the columbium alloys exhibited some surface cracking. The uncoated C-129Y showed tendency to form severe surface cracks while the uncoated C-103 had only fine surface cracks.

Coated molybdenum exhibited no ability to take a bend at -100°F. This is consistent with the tensile results. All the other metal-coating combinations tested, except C-129Y, had the exceptional ability to be bent 180° at -100°F with a 0.150 inch diameter punch (4T) without fracture.

The C-129Y could be bent only 20° to 55° before it failed by base metal cracking. 90 Ta-10W substrate showed ductility, as expected, since no hydrogen is introduced during the coating process. The Durak KA pack cementation process for C-103 and C-129Y induces H_2. The C-129Y and ductile behavior of C-103 was expected, since only the latter was thermally conditioned to restore ductility. Coated C-103 was thermal cycled and ductility was apparently restored. Coated C-129Y, which did not undergo thermal cycling did not bend so much.

The adherance of the coatings to the base metals in all the systems tested was considered to be excellent. While some flaking and peeling were noted it is not considered detrimental for combustor application because of the severity of the test conditions, i.e., 180° 4T bends at -100°F. Even though these disilicide coatings are inter-metallic or ceramic in nature and are not noted for good ductility. The ductility demonstrated is considered sufficient for combustor applications.

c. Fatigue, Room Temperature (Table 11)

As previously found with the slow strain rate tensile tests, forged molybdenum combustion chamber material, if not exposed to conditions as severe as 2150°F, 1 hour, does not exhibit brittle behavior and has very competitive mechanical properties.

At room temperature the uncoated, but thermally conditioned, 1 hour at 2150°F, molybdenum fatigue specimens exhibited extremely brittle behavior. This is consistent with the tensile test results at the same temperature. However, the coated molybdenum test specimens which had been conditioned for only 10 minutes at 2000°F gave excellent fatigue properties at room temperature (9,449,000 cycles at 50 percent of UTS with no failure), again consistent with tensile test results for similar material at the same test temperature.

d. Fatigue-Torch Testing (Tables 12 and 13)

The fatigue torch control specimens were weighed before and after torch testing and the weight changes are presented in Table 12. All of these control specimens gained weight. This weight gain is due to the formation of oxides on both the front and rear surfaces of the test specimen. The weight gains were small and equal to a percentage change of 0.1 to 0.4 percent. However, the weight changes show a small scatter within each of the coating-metal combinations tested.

The fatigue-torch test specimens, were weighed in the same sequence as the controls (before and after torch testing). Some specimens showed weight gains and others showed weight losses. The scatter of weight change values from positive to negative for the fatigue torch specimens is probably due to coating material that has flakes off. This flaking is probably due to the weakening of the coating during the fatigue tests. However, some or all of this flaking could have taken place in the high stress concentration areas close to the attach holes outside the test area.

No torch tests were run on Durak B coated molybdenum because of the wealth of data that has already been generated on this combination. This combination has a torch life at 3100°F of 2 to 6 hours. This superior to any of the metal-coating combinations tested except for the C-103/ W + R508C which did not degrade at 2650°F in the 2 hours maximum test time. While the 2 hours life of this system is undoubtedly greater than 2650°F, it is doubtful that it could equal the 3100°F of Durak B coated molybdenum. Photographs of control specimens are shown in Figures 9, 10, 11, and 12.

All of the fatigue-torch test specimens were fatigue conditioned at -100°F for 10,000 cycles at 15,000 psi stress level. The 15,000 psi stress was the maximum that could be applied to the test specimen configuration used without having failure occur in the loading holes. The 15,000 psi stress level is considerably above that encountered in the Apollo engine under normal operating conditions, however, it is less than might be caused by an ignition overpressure condition.

Since the ultimate strengths of the coated alloys at -100°F varied from 80,000 to 110,000 psi, the 15,000 psi fatigue stressing represents 14 to 19 percent of the ultimate tensile strengths.

The determination of the time of failure for the metal-coating systems tested is a very difficult task. None of the base metals "smoke" as molybdenum does when the oxidation protective coating fails. Therefore, the time of coating degradation was determined by visual examination at the end of each 10 minute cycle. Post test photographs of specimens are shown on Figures 13, 14, 15, and 16.

No effort on torch life was found due to fatigue conditioning at 15,000 psi for 10,000 cycles at -100°F.

Degradation of the R512 coating was always accompanied by formation of a few raised bubbles on the surface of the test specimen. (See Figure 12). The W + R508C aluminide coating (See Figure 14) did not fail at the test temperature prior to the termination of the tests at 2 hours. However, considerable melting and gravity flow of the soft layer had occurred, with a build-up of this molten material at the lower edge of the specimen.

A torch-test temperature of 2900°F was originally selected for all non-molybdenum specimens. This temperature was expected to produce coating failure in approximately 2 hours, since vendors stated all coatings would last at least 2 hours at 2500°F. However, 90Ta - 10W/R512 degraded after only approximately one hour of torch time. The test temperature was therefore reduced to 2650°F for the other specimens.

e. Comparative Bend Peformance

A comparative bend performance table of each of the coated material systems is shown in Table 14. Bend tests were conducted with both fatiguq-torch tested and torch tested only specimens. Values from this -100°F bend test are shown for comparative purposes.

The tests performance showed the C-103 material system substrate was not affected by the oxy-propane torch or the fatigue endurance test followed by the oxy-propane test. The 90Ta-10W/R512 and C-129Y/Durak KA shows partial embrittlement has resulted when exposed to oxy-propane torch testing, however, the amount of degradation may not be enough to degrade the overall performance of this material system.

f. High Speed Tensile Tests

(1) Molybdenum and Molybdenum/Durak B (Table 15)

The values for coated and uncoated molybdenum, Table 14, indicate that high strain rate tests caused the molybdenum to fail in a brittle fashion with elongation values of 0-6 percent. Strength values were also lower than those found during slow strain rate testing. Since high strain rate testing usually raises the strength, these lower strengths can be interpreted as another indication of brittle behavior. The Molybdenum vacuum - thermal cycle for hydrogen exposed specimens had elongation values from 4-6 percent. The specimens usually failued in several places and the pieces could not be recovered to obtain the actual elongation values.

(2) 90Ta-10W and 90Ta-10W/R512 (Table 16)

The test results for 90Ta-10W, coated and uncoated, are presented in Table 16. All strength values have increased by 50 percent - 75 percent as compared to slow strain rate tests. The elongation values show very little scatter and are very similar to those found in the slow strain rate tests. The vacuum-thermal or hydrogen exposures had no effect on strength or ductility.

(3) C-103 and C-103/Durak KA (Table 17)

The data for C-103 and C-103/Durak KA are presented in Table 17. All strength values were increased approximately 50 percent - 100 percent by the high strain rates. Elongation values were high for all test groups. The vacuum-thermal or hydrogen exposures had no effect on the tensile properties or ductility.

(4) C-103/W + R508C (Table 18)

The test results for C-103 / W + R508C are presented in Table 18. The strength of these specimens at room temperature was similar to C-103 / Durak KA, but the C-103 / W + R058C coated specimens had higher strengths and lower elongation values at the -100°F test temperature.

The strength of these specimens, after either vacuum-thermal or hydrogen exposure, was higher than the Durak KA coated C-103 and elongations were lower.

(5) C-129Y and C-129Y/Durak KA (Table 19)

The high strain rate tensile data for C-129Y, coated and uncoated, are presented in Table 19. The high strain rate gave an increase to the room temperature uncoated strength but a much larger increase to the room temperature coated strength. The ductility of the uncoated specimens at -100°F was only 0-8 percent. These low values present a potential problem,however, the coated material at -100°F had 15-16 percent elongation. The explanation for this unusual behavior may lie in the thermal treatment to which the coated specimens are exposed to during the coating cycle, or the bare material was contaminated.

Neither the vacuum-thermal or the hydrogen exposure cause any effect on the elongation values. Strength values were slightly raised by these exposures.

g. Metallography

Photomicrographs were taken of at least one sample specimen subsequent to the tensile tests listed below:

	Slow Strain Rate	Fatigue Torch	High Strain Rate	
			Vacuum Thermal	Hydrogen Exposure
Moly/Durak B	X	--	X	X
90Ta - 10W/R512	X	X	X	X
C-103/Durak KA	X	X	X	X
C-103/W+R508C	X	X	X	X
C129Y/Durak KA	X	X	X	X

It should be noted again, that none of the coatings tested appeared to degrade the mechanical strength properties of the substrate materials. Also, vacuum-thermal cycling between -100°F and 2500°F over a 2 hour period did not degrade the high strain performance of any of the materials system.

(1) Molybdenum/Durak B

(a) Molybdenum/Durak B after slow strain rate tests (Figure 17a)

This sytem has been smoke checked at 2000°F, 5 minutes, for two cycles. As is normal for this disilicide coating on molybdenum, a thin intermetallic layer between the coating and base metal can be seen. The coating itself is primarily composed of $MoSi_2$. The remaining particles observed in the coating are intermetallic constituents. The usual cracking in the coating can also been seen.

(b) Molybdenum/Durak B after High Strain Vacuum-Thermal Cycle (Figure 20).
The intermetallic constituents have been reduced due to vacuum thermal conditioning and slight crazing probably due to outgassing or sublimation is noticeable.

(c) Molybdenum/Durak B After High Strain H_2 Exposure (Figure 20)
H_2 exposure specimen show the intermetallics to have agglomerated, with the usual crazing present. The H_2 exposure did not affect the mechanical strength.

(2) 90Ta-10W/R512

(a) 90Ta-10W/R512 After Slow Strain Rate Tests (Figure 17b)
In this disilicide type of coating, a thin layer can be seen at the coating-metal interface. Two unidentified layers are noted in the coating. Coating crazing can be noted.

(b) 90Ta-10W/R512 After Fatigue-Torch Tests (Figure 21a)
Torch tests have increased the thickness of the diffusion area between coating and substate and severe attak of outer surface is noticeable. However, sufficient coating appears present to provide suitable protection for further torch testing.

(c) 90Ta-10W/R512 After High Strain Thermal Cycling Tests (Figure 21c)
The vacuum thermal conditioning treatment has increased the thickness of the diffusion area and has caused changes on the outer surface. Additional crazing is noticeable in the coating.

(d) 90Ta-10W/R512 After High Strain H_2 Exposure Test (Figure 21b)
Hydrogen exposure produced only minor change to the vacuum coating condition and tests showed no change in mechanical strength or elongation due to this exposure.

(3) C-103/Durak KA

(a) C-103/Durak KA After Slow Strain Rate Tests (Figure 18a)
This coating-metal had been given a thermal conditioning of 2500°F for 2 1/2 hours, in air, after coating. A diffusion barrier is formed as the result of this thermal treatment, and the remainder of the coating is a silicide $Cb_x\ Si_y$. Some severe crazing (vertical and longitudinal) is noted which is filled with oxidation products.

(b) C-103/Durak KA After Fatigue-Torch Testing (Figure 22a)
Torch tests penetrated the coating and changed the diffusion layer structure.

(c) C-103/Durak KA After High Strain Vacuum-Thermal Tests (Figure 22b)
The vacuum thermal treatment caused severe change in the microstructure of the coating. Approximately four distinct coating layers were formed as compared to two on the original coating.

(d) C-103/Durak KA After High Strain H_2 Exposure Tests (Figure 22c)

Hydrogen exposure produced no change to the diffusion area, coating or substate. However, tensile tests showed 2 of 4 specimens were brittle with lower strength, while the other two showed good elongation and strength. Photomicrographs were taken of all four specimens. All appeared similar to both the H_2 exposed specimen shown in Figure 22c and the non-H_2 exposed specimen shown in Figure 18a.

(4) <u>C-103/W+R508C</u>

(a) C-103/W+R508C After Slow Strain Rate Tests (Figure 18b)

The tungsten layer is approximately .002 inch thick. This can be seen in the micro structure. The R508C coating applied over the tungsten layer forms the aluminide structure, an interface layer followed by the hard aluminide structure, an interface layer followed by the hard aluminide layer and then soft eutetic layers.

(b) C-103/W+R508C After Fatigue-Torch Tests (Figure 23a)

Torch tests increased the thickness of the soft eutectic layer. No change to the hard aluminide layer or to the substate was noted. Only minor surface effects were noted on visual inspection.

(c) C-103/W+R508C After High Strain Vacuum-Thermal Tests (Figure 23b)

Vacuum thermal treatment increased the thickness of the soft eutectic layer at the expense of the hard aluminide layers. Inspection of surfaces reveals the majority of the soft eutectic and the hard aluminide have disappeared.

(d) C-103/W+R508C After High Strain H_2 Exposure Tests (Figure 23c)

Hydrogen exposure removed some of the soft eutectic while the remainder of the coating remained intact. Tensile tests revealed no loss in mechanical strength was incurred due to H_2 exposure.

(5) C-129Y/Durak KA

(a) C-129Y/Durak KA After Slow Strain.Rate Tests (Figure 19)

Since no thermal treatment was given to this coating, there is no diffusion into the substate. Fine crazing which did not penetrate to the base metal is noticeable.

(b) C-129Y/Durak KA After Fatigue-Torch Tests (Figure 24a)

Torch testing caused major changes in the coating structure. Specimens show two distinct layers, each having additional phases present. The second layer appears to be a diffusion of the coating into the base metal. The torch testing appears to penetrate the coating layer into the substrate.

(c) C-129Y/Durak KA After High Strain Vacuum-Thermal Tests (Figure 24b)

Vacuum thermal treatment exposure caused Major change in the structure of the coating. Additional phases were noted and intermetallics appear to have agglomerated. Several other changes can be ssen in the coating substate interface. Nevertheless, tensile tests showed approximately 17 percent increase in strength and a minor increase in elongation due to the vacuum thermal cycle.

(d) C-129Y/Durak KA After High Strain H_2 Exposure Tests (Figure 24c)

Hydrogen exposure changed portions of the coatings, such that major crazing is present. Nevertheless, tensile tests showed a 17 percent increase in ultimate strength and no change in elongation.

C. Phase III - High Strain Rate Chamber Experiments

1. Summary

The Phase II Laboratory Tests subjected the test specimens to uniaxial loading only. The full scale combustion chamber test phase was designed to evaluate the performance of selected materials in a more realistic multiple loading environment. The chamber materials selected for evaluation were the same as for the Phase II Laboratory portion tests except for the omission of C129Y/Durak KA. They were:

Molybdenum/Durak B
90Ta-10W/R512
C103/Durak KA
C103/W + R508C

Simulation of the more critical spiking conditions was accomplished through the use of a hydrodynamic test technique. One end of the test chamber was plugged, the chamber was filled with liquid, and a piston at the other end was impacted by a drop weight. The pressures in the liquid were, in this manner, raised to peaks of 15,000 psi, at rise rates in the order of 100 - 250 psi/ sec. Test results are summarized in Table 19. They show the molybdenum chambers failed in a brittle fashion at maximum pressures ranging from 3700 to 6700 psi.

Each of the ductile 90Ta-10W and C-103 chambers exhibited measurable strain within their elastic limit and could not be fractured at the 15,000 psi maximum pressure capability of the test design set-up. The induced stresses for all chambers were computed to be compatible with the allowable ultimate as determined from the high strain rate tests.

2. Test Objectives

The purpose of the full scale combustor test was to evaluate the several material systems of interest under the multiple loading conditions simulating a chamber reaction to an engine ignition spike. Further, a full scale chamber was desirable to insure that machining stresses were properly included in the materials evaluation.

Typical ignition overpressure data had been previously obtained through a lengthy test series utilizing an Apollo configuration combustion chamber fabricated from L-605 stainless steel. A non-preigniter injector was used to generate spike levels beyond those obtainable with the current Apollo SMRCE preigniter design. The L-605 chamber permitted adequate documentation of this extended spike performance region. Representative data from these tests presented in Figures 25 and 26.

Chamber pressure was determined through two methods; Kistler pressure transducer and combustor wall mounted strain gages which had been statically calibrated with chamber pressure. Data analyses show that at higher pressure levels an approximate two to one ratio exists between the strain gage determined pressure and the Kistler measured pressures. This is believed due to the non-symmetrical stresses being imposed on the average pressure stresses and/or a dynamic effect taking place due to the interaction of pressure rise rate and pressure peak time with chamber wall material frequency in both bending and circumferential stress modes.

Further analyses of the representative spike data discussed above shows a peak overpressure of approximately 6,000 psi maximum as determined by the highest value obtained from the 24 strain gages used in this test sequence. A pressure rise rate varying between 150 to 250 psi was determined by measurements obtained with a Kistler pressure transducer.

Test objectives were established to subject the chambers to a pressure level higher than the 6,000 psi peak previously noted but at a pressure rise rate comparable to the spike data. Chambers were, therefore, to be exposed to the following:

Combustion pressure maximum > 10,000 psi (strain gage)
Combustion Pressure rise rate = 150 - 250 psi/micro second (Kistler)

3. Test Techniques and Test Setup

Initially, it was intended to simulate pressure spikes by a hydrostatic technique utilizing nitrogen pressurized chambers. These tests were to be accomplished by installing the chambers in a pressure vessel and simultaneously pressurizing the outside of the chamber with water and the inside of the chamber with nitrogen. A burst diaphragm was to be installed on the water side of the test setup to allow an increase in gas and water pressure until the water pressure burst the diaphgram. Although this technique would not have completely simulated the actual effect of ignition pressure buildup on the combustion chamber, it would have provided a controlled means of applying a rapid pressure transient on the combustion chamber.

Investigation of other suitable spiking simulation techniques included actual engine firings, and a hydrodynamic technique described in detail in Appendix 1. The firing technique was recognized as providing the ultimate in simulation but the random nature of spikes made it impractical to conduct a controlled test such as is required in evaluating several alternate materials with only a very limited number of tests.

The selected approach utilizes the scheme sketched in Figure 1 of Appendix 1. It was selected over the earlier mentioned hydrostatic test because it lent itself to a better controlled test setup. In this adopted scheme, the test chamber is plugged at the throat, filled with a liquid and a piston inserted from the injector side into the chamber. This piston is then impacted with a drop weight; the resulting chamber fluid is pressurized and induces stresses into the chamber walls. A Kistler pressure transducer incorporated into the throat plug provided one measure of the chamber pressure - time history. Strain gages located circumferentially and longitudinally on the chamber exterior critical areas provided another measure of these pressures. A photograph of the test hardware set-up is shown in Figure 27.

Design analyses to guide the design of test set-up components is also detailed in Appendix 1. This analysis assumes the system has a spring analog in which the striker and piston combine to represent the mass. The fluid bulk modulus and system geometry are proportional to a spring constant, the mass displacement is the piston displacement, the energy into the system is the drop weight energy at impact. From this, the time to maximum pressure is described by the relationship for the simple harmonic motion of a spring mass system, i.e., frequency is independent of amplitude. The equation expressing this time to peak pressure is given as:

$$t = \frac{\pi}{2AX} \sqrt{\frac{V\ (W_1 + W_p)}{g\ K'}}$$

where:

t = Time to peak pressure
A_X = Piston cross-sectional area
V = System volume
W = Drop weight
W_p = Piston weight
K^1 = Bulk modulus of chamber fluid

For a given system, the time to peak pressure is, therefore, estimated to be constant and independent of the peak pressure. Peak pressure is varied by changes in drop height. Since the time to peak pressure is constant, rise rates are also varied by changing the peak pressure.

To obtain pressure rise rates comparable to spiking conditions, it was necessary to minimize rise time. This was accomplished by the selection of a working liquid containing the highest bulk modulus. A literature survey showed mercury to be the best available liquid with the required high bulk modulus and it was, therefore, used as a working fluid for all tests.

4. Test Advantages and Relations

As stated earlier, the hydrodynamic or water hammer technique described above was selected because it permits the application of controlled and reproducible stresses to the test chamber.

The degree of ignition spike simulation is restricted. The following two conditions are considered to have been suitably simulated.

a. Rapid or high pressure rate loading conditions.
b. Loading was accomplished both circumferentially and axially.

Other advantages associated with this system are listed below:

a. A large number of data points can be gathered in minimum time.
b. A rapid changeover is possible from one test chamber to another.
c. Facilities required for this test are minimum as compated to other types considered.
d. Manpower requirements to conduct tests are minimized.
e. Tests may be limited to the non-destructive type.

Some of the recognized test limitations are as follows:

a. No temperature simulation.
b. Loading was uniform and not asymmetrical as is characteristic of engine spikes.
c. Circumferential and axial loading was not necessarily sequenced at the same rate as a real engine spike. This is a result of different wave propagation times for the loading methods involved.
d. Transverse chamber detonations or waves are not simulated.
e. Pulse duration was not necessarily the same as for a real engine spike.

A detailed analysis was attempted to show the relationship between the combustion chamber pressures generated hydrodynamically and combustion chamber stress. This analysis is given in Appendix II. The analysis indicated that the water hammer test used to simulate chamber detonations applies a complex load system to the structure being tested. The internal pressure creates circumferential stresses. When the piston generated wave is reflected from the opposite end of the chamber, axial stresses are created. These stresses are propagated through the chamber walls and reflect with increased magnitude from the flange end of the chamber. As the water hammer wave moves through the liquid it creates an axial pressure discontinuity. This causes bending stresses to appear in the walls.

All of these three stresses are transient, appearing at different positions in the chamber at different times. The computation of the maximum combined loading was considered beyond the scope of the present program.

However, the analysis did derive the independent equations which define each of these transients such that they can be computerized and used to estimate the maximum chamber stresses. Further, it showed the estimated maximum circumferential stress can be approximated by using the maximum pressure determined from strain gage readings. The analysis indicated the strain gage readings would be approximately twice the Kistler readings. This general relationship had been earlier established in engine firings with a stainless steel chamber and was again verified in the hydrodynamic test conditions under this program on full scale chambers.

5. Test Hardware

Nine full scale combustion chambers of the Apollo SMRCE configuration were used to obtain comparative data on four material systems including a control. Chambers tested were:

Quantity	Material/Coating	Post-Coating Treatment
3	Moly/Durak B	2 Cycles/5 min/2000°F/Air
2	90Ta-10W/R512	None
2	C-103/Durak KA	2 1/2 Hrs/2500°F/Air
2	C-103/W + R508C	None

Pre-test photographs of each type with strain gages installed is shown in Figure 28. Contract limitations did not provide for testing more than the nine chambers listed above, however, it was concluded that data for a C129Y-Durak KA chamber could be extrapolated from C-103/Durak KA chamber test data using the laboratory specimen tests as a guide.

All material systems were produced to coating specifications and post-coating treatments identical to those used for the slow and high strain rate laboratory specimens. As previously noted, the Molybdenum/Durak B control was processed in accordance with current Apollo SMRCE specifications.

The molybdenum chamber tested was identical to the SMRCE internal and external configuration. Based on a completely recrystallized condition, (i.e., ultimate strength = 42,000 psi), this chamber is calculated to fail at 2580 psi. The calculation is based on the following equation:

$$\sigma = \overset{(1)}{\left(\frac{\delta}{R}\right) E} + \overset{(2)}{\frac{PR}{t}} + \overset{(3)}{\nu \frac{6M}{t^2}}$$

(1) Stress due to flange deflection normal to the chamber center line

(2) Circumferential stress

(3) Stress due to bending

where:

δ = Radial deflection normal to chamber center line
R = Radius of chamber
E = Modulus of elasticity - psi
P = Calculated failure pressure
t = chamber thickness (average)
ν = Poisson's ratio
M = Moment due to discontinuity (at attach flange)
σ = Ultimate allowable stress of material

A molybdenum chamber is shown in Figure 29. The Columbium and Tantalum chambers were designed for circumferential loading only since their ductility makes them non-critical in bending modes. They were designed to yield at 4,500 and 8,000 psi, respectively on the basis of:

$$\sigma_y = \frac{PR}{t}$$

Figures 30 and 31 are photos of C-103 Columbium and 90Ta-10W Tantalum chambers prior to coating. These were designed with straight exterior chamber walls for simplicity. Their interior configuration was identical to the Apollo SMRCE engine. The variation of exterior configuration of these test chambers was not considered a factor which would influence test results. Previously conducted Apollo sponsored tests on typical molybdenum chambers have shown the effective wall thickness to be the average wall thickness of the chamber. Accordingly, chambers could be compared on the basis of average wall thickness.

The C-103 chambers were not machined below the combustion chamber diameter dimension at the throat section exterior. This section of the combustion chamber is non-critcal and does not influence test results.

6. Test Procedure

Initial tests were performed with a stainless steel chamber to check the instrumentation and other test setup features. Maximum strain gage pressures of 6,000 psi and Kistler pressure rise rates of 150 psi/micro seconds were obtained before proceeding with the nine chambers to be evaluated.

All of these nine chambers were loaded incremently to either failure or to the maximum capability of the test setup, 12,000 to 15,000 psi, well in excess of chamber design values.

Kistler and strain gage data were taken to establish both the dynamic yield and permanent yield (if any) and/or the failure pressures and pressure rise rates.

Typical oscillograph traces are illustrated in Figures 25 and 26 for a L-605 chamber during engine firing tests. For comparison, Figure 32 is provided to show a typical trace obtained with hydrodynamic testing.

7. Test Results

a. General

A summary of the results obtained from the hydrodynamic testing of the nine full scale test chambers is shown in Table 20. The results indicate the data obtained from the high strain rate tensile test are compatible with the full scale chamber results. This compatibility indicates a suitability for use in combustion chamber design.

Table 20 shows, for each chamber tested, the recorded maximum Kistler measured pressure, Kistler measured rise rate, and strain gage measured pressure. An approximate two to one ratio of strain gage to Kistler pressure maximum is noted. This ratio is comparable to that obtained during firing tests conducted with L-605 chambers. It is also consistent with the previously discussed test technique analysis. Further, the Kistler pressure rise rates all vary between 185-250 psi/microseconds and are within the 150-250 psi microsecond range observed during L-605 firing tests. These data tend to validate the hydrodynamic test approach.

Table 20 also lists the maximum induced computed stress for each chamber. Strain gage pressure readings were used as a basis for these computations instead of Kistler values because the strain gage reading is based on the actual material response to the pressure field. In this way, the computation includes the effects of configuration, machining stresses, dynamic factors, etc. Finally, the material system ultimate stress, as determined by the high strain rate test phase, is shown for comparison with the computed induced stress on chambers. As is further explained in the following paragraphs, the computed induced stresses are in all cases compatible with these material ultimates.

b. Molybdenum/Durak KA

Figure 33 is a photograph of a molybdenum/Durak KA chamber after it had been fractured as a result of exposure to a strain gage measured chamber pressure of 6700 psi. Figure 34 shows a similar chamber fractured during engine firing tests. The similarity between the failure modes may be observed. Both show brittle failure. The longitudinal cracks in the hydrodynamic test chamber indicate failure primarily in the circumferential or hoop mode. The transverse cracks indicate a secondary failure in bending. The hot fired chamber appears to have failed in a multiple loading mode including both bending and hoop loads.

Table 20 lists two values for stresses induced in the molybdenum chamber. The computed minimum value assumes failure was in the circumferential mode only. The maximum computed stress assumes failure in a multiple loading manner. This latter stress computation was made using the combined loading equation used in the preceeding section. The real stress probably lies somewhere between these two limits. The photo indicates it to be closer to the circumferential mode.

It is noted that the high strain rate determined ultimate falls between these two induced stress limits in both cases where data at failure was obtained.

c. <u>90Ta-10W/R512</u>

The 90TA-10W/R512 chambers withstood dynamic loads as high as 15,000 psi at Kistler rise rates to 250 psi/microseconds with no permanent set. (The .0005 to .0014 inch changes noted in the pre and post test measurement of the combustion chamber diameters are within coating tolerances).

Pressures above 15,000 psi could have been obtained by redesign of the chamber throat plug and piston seals. However, 15,000 psi is more than adequate to simulate the maximum anticipated spike levels.

The 90Ta-10W chambers had been designed for .002 inches per inch yield strain at 8,000 psi pressure based upon typical slow strain rate design data. However, these chambers withstood .0046 inches per inch strain without permanent set, almost twice the design pressure. The induced stresses are computed to be 120,000 to 155,000 psi. The high strain data for this material 154,000 - 165,000 psi ultimate. Lack of a high strain rate yield point makes a complete comparison between these data impossible. However, the data are not in conflict, and may be considered comparable. This showed the feasibility of the high strain data for combustion design. In achieving these maximum pressures, the chamber was subjected to pressures in excess of 5,000 psi approximately ten times.

A photomicrograph of a chamber cross section taken in the area of a strain gage installation is shown in Figure 35. No flaking or cracking of the coating into the substrate is apparent. Typical surface crazing is noted as was observed in the high strain test specimens.

d. C-103/Durak KA

The C-103/Durak KA chambers behaved similarly to the 90Ta-10W chambers and did not suffer permanent set at maximum pressures. The maximum pressure reached was approximately 11,000 psi. Pressures above this level could have been obtained by redesigning of the throat plug and piston seals. However, 11,000 psi is considered more than adequate to simulate maximum anticipated spike levels.

The C-103 chambers had been designed to yield at 4500 psi pressures based on .002 inches per inch yield strain at typical slow strain rate values. The chamber performance, however, was approximately three times this value without any permanent set. The computed induced stresses were 106 - 150,000 psi and are below the 137 - 148,000 ultimate values determined by high strain rate testing. Again, the values obtained for these parameters are comparable, even though high strain rate yield data is not available for a complete comparison.

In achieving the maximum pressures noted, these chambers were subjected to pressures greater than 5,000 psi approximately fifteen times.

A photomicrograph of a combustion chamber cross section through a strain gaged area is shown in Figure 36b. The crazing appears to stop in the diffusion layer indicating the coating would continue to offer protection from an oxidizing atmosphere.

Figure 36a is a photomicrograph of a 2 1/2 inch diameter control sample of this same Cb103/Durak KA material system. However, the control was not given the 2 1/2 hour/2500°F/air thermal treatment. The lack of a diffusion layer is noted.

e. C-103/W + R508C

C-103/W + R508C chambers behaved in a similar manner to the C-103 and 90Ta-10W chambers discussed above. That is, no permanent set was observed at the maximum attained combustion chamber pressure, 14,000 psi and 210 psi/microsecond rise rate. And again, this chamber pressure maximum was due to sealing limitations and is well above anticipated spike levels.

The chamber withstood approximately three times its slow strain yield design maximum of .002 inches per inch at 4500 psi pressure; dynamic strains to .0053 inches per inch were recorded at pressures to 14,300 psi without permanent set. These data are comparable to high strain rate tensile tests. The test procedures subjected these chambers to approximately ten impact loads greater than 5,000 psia.

A post test visual check showed some of the coating had flaked off in large areas. However, a photomicrograph of a section through one of these flaked areas near a strain gage (Figure 37b) shows that only the soft eutectic external layer was lost; the hard aluminide coating remains intact. It is also possible that the soft eutectic was chemically attacked between mercury liquid in the chamber. Figure 37a is a microphotograph of a control disc of this same material system. It shows the soft eutectic layer in its original form.

REFERENCES

1. K. G. Hoge, Some Mechanical Properties of Uranium -10 Wt. % Molybdenum Alloy Under Dynamic Tension Loads, February 1965
2. Koshiro Oi, Transient Response of Bonded Strain Gages
3. L. Sama, S. Priceman, B. Reznick, Development of Oxidation Resistant Coatings for Refractory Metals, STR 64-5401.5 August 1964
4. J. J. Kappl, R. M. Knox, Altitude Ignition Hypergolic Bipropellant Rockets
5. A. R. Stetson, V. S. Moore, Development and Evaluation of Coating & Joining Methods for Refractory Foils, RTD-TOR-63-4006 Part III, June 1965
6. P. G. Shewmon, V. F. Zackay, Response of Metals to High Velocity Deformation, Vol. 9 Metallurgical Society Conference, July 1960
7. R. J. Roark, Formulas for Stress & Strain, 1954
8. R. Sedlacek, Tensile Strength of Brittle Materials, AFML-TR-65-129 August 1965
9. L. Sama, D. Lawthers, G. Pepino, Sylcor Hf-Ta Base Slurry Coating SIR-65-1, September 1965
10. K. Marnock, High Temperature Oxidation Resistant Hafnium-Tantalum System, AFML-TR-65-240, July 1965

TABLE I

TEST SPECIMEN CONFIGURATION
Tensile and Fatigue

Material and Test	Overall Length (in)	Threads	Length of Threads (in)	Test Section Diameter (in)	Radius-Test Section to Thread (in)
Molybdenum - Slow Strain Rate Tensile and Fatigue	3.28	1/2-13UNC	0.62	0.125	0.5
Molybdenum - High Strain Rate Tensile	3.5	1/2-20NF	0.75	0.125	0.5
C-103, C-129Y 90Ta-10W High Strain Rate Tensile	3.5	1/2-20NF	0.75	0.125	0.5
Slow Strain Rate Tensile	3.5	1/2-13UNC	0.62	0.125	0.5

BEND

Molybdenum, 90Ta-10W, C-103 - 1/2"x 2"x 0.040" inch thick edges rounded

C-129Y - 1/2"x 2"x 0.030" inch thick edges rounded

FATIGUE - TORCH

90Ta-10W, C-103 - 3"x 6"x 0.040" inch thick, edges rounded, (2) 3/8 inch diameter loading holes at each end

C-129Y - 3"x 6"x 0.030" inch thick, edges rounded, (2) 3/8 inch diameter loading holes at each end

TABLE 2

THICKNESS INCREASE DUE TO COATING

Molybdenum / Durak B	2000°F, 5 Minutes, 2 Cycles	
	3 Bend Specimens	0.0025 - 0.0035 inch (2 surfaces)
90Ta-10W / R512	6 Fatigue-Torch Specimens	
	Thickness Increase	0.005 - 0.007 inches (2 surfaces)
C-103 / Durak KA	2500°F, 2 1/2 Hours, Air	
	6 Fatigue-Torch Specimens	
	Thickness Increase	0.002 - 0.004 inches (2 surfaces)
C-103 / W + R508C	14 Tensile Specimens	
	Diameter Increase due to W: - 0.0022 - 0.0039 inches	
	Diameter Increase due to W: - R508C: 0.0095 - 0.0145 inches	
C-129Y / Durak KA	6 Fatigue-Torch Specimens	
	Thickness Increase	0.002 - 0.003 inches (2 surfaces)

TABLE 3

SLOW STRAIN RATE TENSILE PROPERTIES AT ROOM TEMPERATURE FOR UNCOATED MATERIAL

Material:	1/2" Diameter rod for 90Ta-10W, C-103, C-129Y, Forgings for Molybdenum
Thermal Conditioning:	2150°F, 1 Hour, Vacuum
Strain Rate:	0.005 in./in./Min to Yield Strength 0.05 in./in./Min to Rupture

Specimen Number	Material	Yield Strength 0.2% (ksi)	Ultimate Tensile Strength (ksi)	Elongation in 1.0 Inch (%)	Modulus of Elasticity (x10^6 psi)
672M	Molybdenum	-	51.3	-	39.
677M	Molybdenum - No thermal conditioning	86.4	104.1	24.	45.
675M		92.2	104.7	30.	41.
683M	C-129Y	65.5	83.7	28.	17.
684M	C-129Y	68.9	86.4	25.	18.
(1)	90Ta-10W	(102.)	(138.)	35, for 0.5 in G.L	(20 to 27)
(2)	C-103	45.0	59.0	26.0	12.6

(1) Data from Aerospace Structural Metals Handbook, Volume II

(2) Wah Chang (Sheet - No bar data available)

TABLE 4

SLOW STRAIN RATE TENSILE PROPERTIES AT ROOM TEMPERATURE FOR COATED MATERIAL

Material:	1/2 inch Diameter for 90Ta-10W, C-103, C-129Y, Forgings for Molybdenum
Thermal Conditioning after Coating:	Molybdenum - 2000°F, 5 Minutes, Air, (2 Cycles) C-103 (Durak KA) 2500°F, 2 1/2 Hours, Air Others - None
Strain Rate:	0.005 in./in./Min to Yield Strength 0.05 in./in./Min to Rupture
Test Temperature:	Room Temperature

Specimen Number	Material	Yield Strength 0.2% (ksi)	Ultimate Tensile Strength (ksi)	Elongation in 1.0 Inch (%)	Modulus of Elasticity ($X10^6$ psi)
658M	Molybdenum +	73.0	87.9	23	46
659M	Durak B	45.5	72.5	32	42
723M	90Ta-10W +	80.0	92.4	27	25
724M	R512	77.0	91.7	24	26
691M	C-103 +	45.5	61.9	32	15
692M	Durak KA	46.5	61.8	27	16
749M	C-103 +	54.9	68.2	16.8	20
750M	W + R 508C	52.1	67.3	20.0	19
679M	C-129Y +	63.6	84.0	24	16
680M	Durak KA	67.0	87.8	18	17

TABLE 5

SLOW STRAIN RATE TENSILE PROPERTIES AT -100°F FOR UNCOATED MATERIAL

Material:	1/2" Diameter rod for 90Ta-10W, C-103, C-129Y, Forgings for Molybdenum
Thermal Conditioning:	2150°F, 1 Hour, Vacuum
Strain Rate:	0.005 in./in./Min to Yield Strength 0.05 in./in./Min to Rupture
Test Temperature:	-100°F, Dry ice and alcohol immersion

Specimen Number	Material	Yield Strength 0.2% (ksi)	Ultimate Tensile Strength (ksi)	Elongation in 1.0 Inch (%)	Modulus of Elasticity ($x10^6$ psi)
665M	Molybdenum	-(1)	90.7	-	43.
666M	Molybdenum	-(1)	55.2(2)	-(2)	45.
729M	90Ta-10W	108.1	119.8	24.	27.
730M	90Ta-10W	108.8	118.1	24.	27.
693M	C-103	56.3	74.6	27.	13.
694M	C-103	57.6	78.1	25.	13.
685M	C-129Y	85.2	103.	17.	18.
686M	C-129Y	86.4	105.	25.	16.

(1) Brittle Break, no yield

(2) Broke in Radius

TABLE 6

SLOW STRAIN RATE TENSILE PROPERTIES AT -100°F FOR COATED MATERIAL

Material:	1/2" Diameter rod for 90Ta-10W, C-103, C-129Y, Forgings for Molybdenum
Thermal Conditioning After Coating:	Molybdenum - 2500°F, 5 Minutes, Air, (2 Cycles) C-103 + Durak KA - 2500°F, 2 1/2 Hours, Air Others - None
Strain Rate:	0.005 in./in./Min to Yield Strength 0.05 in./in./Min to Rupture
Test Temperature:	-100°F, Immersion in Dry Ice and Alcohol

Specimen Number	Material and Coating	Yield Strength 0.2% (ksi)	Ultimate Tensile Strength (ksi)	Elongation in 1.0 Inch (%)	Modulus of Elasticity (x10^6 psi)
655M	Molybdenum + Durak B	(71.9)*	90.5	0	42.
656M		(68.9)*	86.8	0	44.
657M		(91.8)*	98.3	1	48.
721M	90Ta-10W + R512	99.1	112.2	21	28.
722M		94.8	108.8	19	25.
689M	C-103 + Durak KA	61.6	79.3	24	15
690M		63.1	79.7	18	18
747M	C-103 + W + R508C	68.7	84.5	19	22
748M		72.1	90.1	17	23
676M	C-129Y + Durak KA	89.9	108.6	9	17
677M		94.2	104.3	24	17
678M		77.7	94.4	29	15

*Specimen did not reach 0.2% offset values reported are for proportional limit

TABLE 7

SLOW STRAIN RATE TENSILE PROPERTIES AT 2500°F FOR UNCOATED MATERIAL

Material:	1/2" Diameter Rod for 90Ta-10W, C-103, C-129Y, Forgings for Molybdenum
Thermal Conditioning:	2150°F, 1 Hour, In Vacuum
Strain Rate:	0.005 in./in./Min to Yield Strength 0.05 in./in./Min to Rupture
Test Temperature:	2500°F, 15 Minutes hold time, self resistance heating
Temperature Measurement:	

Specimen Number	Material	Yield Strength 0.2% (ksi)	Ultimate Tensile Strength (ksi)	Elongation in 1.0 Inch (%)	Modulus of Elasticity ($x10^6$ psi)
663M	Molybdenum	7.3	10.9	5.0	13
664M	Molybdenum	-	-	-	-
727M	90Ta-10W	23.7	30.0	8.0	12
728M	90Ta-10W	28.3	35.7	6.0	17
699M	C-103	16.4	23.4	11.0	9
700M	C-103	10.9	15.8	15.0	11
681M	C-129Y	21.0	28.6	3.5	11
682M	C-129Y	18.0	18.5	3.5	11

TABLE 8

SLOW STRAIN RATE TENSILE PROPERTIES AT 2500°F FOR COATED MATERIAL

Material:	1/2" Diameter rod for 90Ta-10W, C-103, C-129Y, Forgings for Molybdenum
Thermal Conditioning After Coating:	Molybdenum - 2000°F, 5 Minutes, Air, (2 Cycles) C-103 + Durak KA - 2500°F, 2 1/2 Hours, Air Others - None
Strain Rate:	0.005 in./in./Min to Yield Strength 0.05 in./in./Min to Rupture
Test Temperature:	2500°F, Minutes hold time, self resistance heating, in air
Temperature Measurement:	Photomatic Automatic Optical Pyrometer Model A107 Pyrometer Instrument Co.

Specimen Number	Material and Coating	Yield Strength 0.2% (ksi)	Ultimate Tensile Strength (ksi)	Elongation in 1.0 Inch (%)	Modulus of Elasticity ($x10^6$ psi)
660M	Molybdenum + Durak B	9.2	12.0	8.5	4.0
661M		7.5	11.2	9.0	3.7
662M		8.2	11.9	8.0	7.5
725M	90Ta-10W + R512	22.4	29.7	19.5	19
726M		23.4	31.0	20.0	19
697M	C-103 + Durak KA	10.8	14.8	17	11
698M		10.1	14.5	19	11
751M	C-103 + W + R508C	-	-	-	-
752M		12.4	17.5	3.0	12
687M	C-129Y + Durak KA	18.0	22.7	15	13
688M		16.5	22.1	13	10

TABLE 9

BEND TESTS AT -100°F FOR UNCOATED MATERIAL

Material:	Sheet for 90Ta-10W, C-103, C-129Y, Strip cut from Forgings for Molybdenum
Thermal Comditioning:	2150°F, 1 Hour, Vacuum
Test Temperature:	-100°F, Immersion in dry ice and alcohol
Test Speed:	1 in./Min (Approx.)

Specimen Number	Material	Thickness (inch)	Bend Diameter (inch)	Bend Angle (°)	Remarks
811M	Molybdenum	.041	.150	0	10° Elastic Bend
812M	Molybdenum	.041	.150	4	Brittle Break
774M	90Ta-10W	.042	.150	180	No visible cracks
775M	90Ta-10W	.042	.150	180	No visible cracks
756M	C-103	.038	.150	180	Small surface cracks at edges
757M	C-103	.038	.150	180	Very small surface cracks in bend
792M	C-129Y	.030	.150	180	Heavy surface cracking throughout bend
793M	C-129Y	.030	.150	180	Heavy surface cracking throughout bend

TABLE 10

BEND TESTS AT -100°F FOR COATED MATERIAL

Material:	Sheet for 90Ta-10W, C-103, C-129Y, Strip Cut From Forgings for Molybdenum
Thermal Conditioning After Coating:	Molybdenum - 2000°F, 5 Minutes, Air (2 Cycles) C-103 (Durak KA) - 2500°F, 2 1/2 Hours, Air Others - None
Test Temperature:	-100°F, Immersion in Dry Ice and Alcohol
Test Speed:	1 in./Min (Approx)

Specimen Number	Material and Coating	Thickness After Coating And Thermal Conditioning (inch)	Bend Diameter (inch)	Bend Angle (°)	Remarks
807M	Molybdenum + Durak B	.0445	.150	0	Cracked
808M		.044	.150	0	Cracked
809M		.0445	.150	0	Cracked
771M	90Ta-10W + R512	.047	.160	180	Coating flaking on edges
772M		.047	.150	180	Coating flaking on edges
753	C-103 + Durak KA	.042	.150	180	Coating flaking on edges
754M		.0415	.150	180	Coating flaking on edges and face
1	C-103 + W + R508C	.052	.150	180	Coating flaking and spalling
2		.0515	.150	180	Coating peeling
3		.051	.150	180	Coating flaking and spalling
5		.052	.150	180	Coating flaking and spalling
789M	C-129Y + Durak KA	.032	.150	30	Cracked
790M		.0325	.150	20	Cracked
791M		.032	.150	55	Cracked

TABLE 11

FATIGUE PROPERTIES AT ROOM TEMPERATURE FOR MOLYBDENUM

Material:	Forgings
Fatigue Testing Stress Ratio:	Min/Max = 0.1
Testing Speed:	1800 cpm
Thermal Conditioning:	2150°F, 1 Hour, Vacuum

UNCOATED

Specimen Number	Load (psi)	Cycles to Failure
673M	40,000	Less than 1000
674M	20,000	Less than 1000

COATED

Coating:	Durak B, Per Marquardt MSP 519, 0.0026 ± 0.0006 inch thick per surface
Coating Thermal Check:	2000°F, 5 Minutes, in air, (2 cycles)

Specimen Number	Load (psi)	Cycles to Failure
668M	25,000	2,000,000 No Failure
669M	35,700	3,016,000 No Failure
670M	50,400	1,000
671M	43,200	9,449,000 No Failure

TABLE 12

WEIGHT CHANGE OF FATIGUE-TORCH TEST SPECIMENS

Material:	Sheet - 0.030 inch thick C-129Y - 0.040 inch thick C-103 and 90Ta-10W
Thermal Conditioning After Coating:	C-103 + Durak KA - 2500°F, 2 1/2 Hours, Air Others - None
Fatigue Conditioning Treatment:	10,000 cycles, 15,000 psi max. stress, $\frac{\text{Minimum Stress}}{\text{Maximum Stress}}$ = 0.01, 1800 CPM, specimen immersed in a mixture of dry ice and alcohol at -100°F

Material and Coating	Nominal Specimen Weight (gm)	Controls (Torch Test Only)		Test Specimens (Fatigue and Torch Test)	
		Specimen Number	Weight After Torch Test Minus Weight Before Torch Test (gms)	Specimen Number	Weight After Torch Test Minus Weight Before Torch Test (gms)
90Ta-10W + R512	195.	783M	+ 0.73	786M	+0.43
		784M	+0.45	787M	+0.60
		785M	+0.35	788M	+0.31
C-103 + Durak KA	100	765M	+0.05	768M	+0.06
		766M	+0.05	769M	-0.13
		767M	+0.05	770M	+0.04
C-103 + W+R508C	135	1	+0.07	4	-0.06
		2	+0.02	5	-0.09
		3	+0.12	6,000 cycles	+0.10
C-129Y +Durak KA	80	801M	+0.05	805M 1000 cycles	-0.09
		802M	+0.06		
		803M	+0.06	806M	+0.05

TABLE 13

FATIGUE-TORCH TEST DATA

Material:	Sheet - 0.030 inch thick C-129-Y 0.040 inch thick C-103 and 90Ta-10W
Thermal Conditioning after Coating:	C-103 and Durak KA - 2500°F, 2 1/2 hours, Air. Others - None
Fatigue Conditioning Treatment:	10,000 cycles; 15,000 psi max. stress $\frac{\text{Minimum Stress}}{\text{Maximum Stress}} = +0.01$, 1800 cpm Specimen immersed in a mixture of dry ice and alcohol at -100°F
Torch Test Equipment:	Marquardt Coated Materials Evaluation Test Facility (Oxy-Propane)
Torch Test Procedure:	Run in 10 minute cycles (run 10 minutes, cool with air blast, inspect, start next run)
Temperature Measurement Equipment:	Pyromatic automatic optical pyrometer and ray-o-tube thermopile

Material and Coating	Test Temperature (°F)	Controls (Torch Test Only)			Fatigue Test Specimens (Fatigue Cycling Torch Test)		
		Specimen Number	Total Run Time (min)	Remarks	Specimen Number	Total Run Time (min)	Remarks
90Ta-10W + R512	2900 ±100	783M	60	Degraded	786M	60	Degraded
		784M	50	Degraded	787M	70	Degraded
		785M	50	Degraded	788M	60	Degraded
C-103 + Durak KA	2650 ± 50	765M	120	Degraded*	768M	120	Degraded*
		766M	120	Degraded*	769M	90	Degraded*
		767M	120	Degraded*	770M	120	Degraded*
C-103 + W + R508C	2650 ± 50	1	120	No Effects	4	120	No Effects
		2	120	No Effects	5	120	No Effects
		3	120	No Effects	6	120	No Effects
C-129-Y + Durak KA	2650 ± 50	801M	120	Degraded	805M	120	Degraded
		802M	120	Degraded	(1000 cycles)		
		803M	120	Degraded	806M	120	Degraded

*Degraded also severe attack of back surface.

TABLE 14

COMPARATIVE BEND & ELONGATION PERFORMANCE

Bend Test = .002 in/Sec.

Material/Coating	-100°F	Torch Controls R.T.	Fatigue-Torch R.T.	Slow** Strain Rate Elongation ~ % R.T./-100°F
90Ta-10W/R512	180°	45°*	80°	25%/20%
C-103/Durak KA	180°	180°	180°	29%/22%
C-103/W + R508C	180°	180°	180°	18%/18%
C-129Y/Durak KA	35°	15°*	90°*	21%/21%

*Test Stopped at First Indication of Cracks

**Results taken from previously conducted slow strain tensile testing

TABLE 15

HIGH STRAIN RATE TENSILE PROPERTIES FOR MOLYBDENUM

Material - Forgings

Thermal Conditioning - Uncoated - 2150°F, 1 Hour Vacuum
Coated - 2000°F, 5 Minutes, Air, 2 Cycles

Test Machine - Optron Model 900

Test Speeds - Approximately 200 in/in/sec

Stress Rise Rate - Approximately 7.3 x 10^6 psi/ms

Specimen No.	Type		Test Temperature (°F)	Ultimate Tensile Strength (KSI)	Elongation (%)
716M	Uncoated		RT	40.4	2
712M	Uncoated		-100	45.2	2
713M	Uncoated		-100	43.1	-
714M	Uncoated		-100	71.0	-
715M	Uncoated		-100	-	2
701M	Coated	Durak B	RT	75.4	0
702M	Coated	Durak B	RT	-	0
717M	Coated	Durak B	RT	85.0	-
720M	Coated	Durak B	RT	-	4
703M	Coated	Durak B	-100	67.5	6
718M	Coated	Durak B	-100	79.0	4
719M	Coated	Durak B	-100	(134)*	6
704M	Coated	Vacuum Exp.	-100	-	2
705M	Coated	Vacuum Exp.	-100	72.0	-
706M	Coated	Vacuum Exp.	-100	69.0	-
707M	Coated	Vacuum Exp.	-100	-	4
708M	Coated	15% H_2 Exp.	-100	(201)*	-
709M	Coated	15% H_2 Exp.	-100	74.0	-
710M	Coated	30% H_2 Exp.	-100	86.0	-
711M	Coated	30% H_2 Exp.	-100	51.0	-

* Data shows excessive ringing

TABLE 16

HIGH STRAIN RATE TENSILE PROPERTIES OF 90Ta-10W

Material - 1/2 Inch Diameter Rod

Thermal Conditioning - Uncoated - 2150°F, 1 Hour, Vacuum
Coated - None

Test Machine - Optron Model 900

Test Speeds - Approximately 500 in/in/sec (plastic strain)

Stress Rise Rates - Approximately 4.15 x 10 psi/ms

Specimen No.	Type	Test Temperature (°F)	Ultimate Tensile Strength (KSI)	Elongation (%)
649M	Uncoated	RT	161.0	27
651M	Uncoated	RT	146.0	34
647M	Uncoated	-100	162.0	27
648M	Uncoated	-100	183.0	25
650M	Uncoated	-100	200.0	26
653M	Coated - R512	RT	165.0	26
654M	Coated - R512	RT	154.0	27
637M	Coated - R512	-100	203.0	20
638M	Coated - R512	-100	169.0	24
652M	Coated - R512	-100	172.0	29
639M	Coated Vacuum Exp.	-100	176.0	25
640M	Coated Vacuum Exp.	-100	185.0	26
641M	Coated Vacuum Exp.	-100	-	27
642M	Coated Vacuum Exp.	-100	171.0	22
643M	Coated 15% H_2 Exp.	-100	200.0	26
644M	Coated 15% H_2 Exp.	-100	-	19
645M	Coated 30% H_2 Exp.	-100	166.0	25
646M	Coated 30% H_2 Exp.	-100	176.0	24

TABLE 17

HIGH STRAIN RATE TENSILE PROPERTIES FOR C-103

Material - 1/2 inch diameter rod

Thermal Conditioning - Uncoated - 2150°F, 1 Hour, Vacuum
Coated - 2500°F, 2 1/2 hours, Air

Test Machine - Optron Model 900

Test Speeds - Approximately 500 in/in/sec (Plastic strain)

Stress Rise Rate - Approximately 2.6×10^6 psi/ms

Specimen No.	Type	Test Temperature (°F)	Ultimate Tensile Strength (KSI)	Elongation (%)
631M	Uncoated	RT	95.0	28
633M	Uncoated	RT	70.0	31
636M	Uncoated	RT	105.0	30
632M	Uncoated	-100	131.0	26
634M	Uncoated	-100	131.0	26
635M	Uncoated	-100	144.0	19
695M	Uncoated	-100	142.0	28
617M	Coated - Durak KA	RT	137.0	33
618M	Coated - Durak KA	RT	138.0	26
620M	Coated - Durak KA	RT	148.0	32
619M	Coated - Durak KA	-100	126.0	22
621M	Coated - Durak KA	-100	110.0	22
622M	Coated - Durak KA	-100	120.0	26
623M	Coated Vacuum Exp.	-100	114.0	23
624M	Coated Vacuum Exp.	-100	120.0	26
625M	Coated Vacuum Exp.	-100	123.0	27
626M	Coated Vacuum Exp.	-100	127.0	19
627M	Coated 15% H_2 Exp.	-100	-	
628M	Coated 15% H_2 Exp.	-100	117.0	22
629M	Coated 30% H_2 Exp.	-100	114.0	22
630M	Coated 30% H_2 Exp.	-100	-	-

TABLE 18

HIGH STRAIN RATE TENSILE PROPERTIES FOR C-103/W + R508C

Material	- 1/2 Inch Diameter Rod
Thermal Conditioning	- Uncoated - 2150°F, 1 Hour, Vacuum Coated - None
Test Machine	- Optron Model 900
Test Speeds	- Approximately 500 in/in/sec (plastic strain)
Stress Rise Rate	- Approximately 2.6 x 10^6 psi/ms

Specimen No.	Type	Test Temperature (°F)	Ultimate Tensile Strength (KSI)	Elongation (%)
740M	Coated - W + R508C	RT	136.0	20
743M	Coated - W + R508C	RT	121.0	20
745M	Coated - W + R508C	RT	133.0	30
739M	Coated - W + R508C	-100	129.0	-
741M	Coated - W + R508C	-100	117.0	15
742M	Coated - W + R508C	-100	165.0	16
744M	Coated - W + R508C	-100	144.0	14
746M	Coated - W + R508C	-100	145.0	20
731M	Coated Vacuum Exp.	-100	127.0	18
732M	Coated Vacuum Exp.	-100	167.0	18
733M	Coated Vacuum Exp.	-100	169.0	18
734M	Coated Vacuum Exp.	-100	136.0	17
735M	Coated 15% H_2 Exp.	-100	165.0	21
736M	Coated 15% H_2 Exp.	-100	171.0	14
737M	Coated 30% H_2 Exp.	-100	172.0	22
738M	Coated 30% H_2 Exp.	-100	134.0	16

TABLE 19

HIGH STRAIN RATE TENSILE PROPERTIES FOR C-129Y

Material - 1/2 Inch Diameter Rod

Thermal Conditioning - Uncoated - 2150°F, 1 Hour, Vacuum
Coated - None

Test Machine - Optron Model 900

Test Speeds - Approximately 500 in/in/sec (plastic strain)

Stress Rise Rate - Approximately 2.7×10^6 psi/ms

Specimen No.	Type		Test Temperature (°F)	Ultimate Tensile Strength (KSI)	Elongation (%)
612M	Uncoated		RT	128.0	20
614M	Uncoated		RT	124.0	22
616M	Uncoated		RT	119	28
611M	Uncoated		-100	-	-
613M	Uncoated		-100	153.0	3
615M	Uncoated		-100	119.0	8
597M	Coated -	Durak KA	RT	142.0	25
600M	Coated -	Durak KA	RT	171.0	22
602M	Coated -	Durak KA	RT	157.0	28
598M	Coated -	Durak KA	-100	142.0	15
599M	Coated -	Durak KA	-100	169.0	16
601M	Coated -	Durak KA	-100	142.0	16
604M	Coated	Vacuum Exp.	-100	185.0	18
605M	Coated	Vacuum Exp.	-100	165.0	17
606M	Coated	Vacuum Exp.	-100	181.0	20
607M	Coated	15% H_2 Exp.	-100	176.0	15
608M	Coated	15% H_2 Exp.	-100	167.0	17
609M	Coated	30% H_2 Exp.	-100	173.0	13
610M	Coated	30% H_2 Exp.	-100	192.0	17

TABLE 20

FULL SCALE CHAMBER TEST RESULTS

Combustor/Coating	Wall Thickness Coating Thickness (inches)	Chamber Dia. Before Test (inches)	Chamber Dia. After Test (inches)	Remarks	Kistler Press - Psi Kistler Rise Rate Psi/μsec Strain Gage Equiv. Press Psi	Induced Stress Psi	High Strain Rate Tensile Test Ult. Stress @ R.T. - Psi
T10664 S/N 008 Molybdenum/Durak B Disilicide Post Coating Treatment-5 Min (2000°F) 2 cycles	.110 .0026 ± .0006	1.9040/1.9049		Fractured No. of Impact Loading ~ 14	P_K = 3400 PRR = 215 $P_{s.g}$ = 5700	1. 57,000 2. 82,000	Ftu = 75-85,000
T10664 S/N 1001 Molybdenum/Durak B Disilicide Post Coating Treatment-5 Min (2000°F) 2 cycles	.110 .0026 ± .0006	1.9040/1.9028		Fractured No. of Impact Loads = 6	P_K = 3500 PRR = 190 $P_{s.g}$ = 6700	1. 67,000 2. 109,000	
T10664 S/N 010 Molybdenum/Durak B Disilicide Post Coating Treatment-5 Min (2000°F) 2 cycles	.110 .0026 ± .0006	1.9041/1.9034		Chamber Fractured No data-Instrm. did not trigger. Data is from previous drop test. No. of Impact Loads = 9	$P_K \geq 2900$ PRR ≥ 183 $P_{s.g} \geq 3700$	1. > 37,000 2. > 60,000	
T8298 S/N 003 90Ta-10W/Sylcor R512 Disilicide Post Coating Treatment - None	.076 .0025 ± .0005	1.9330/1.9335	1.9337/1.9349	No permanent set * Δ Dia. = .0006-.0014. Max. dynamic strain = .004. No. of impact loads = 10	P_K = 6300 PRR = 217 $P_{s.g}$ = 15,500	155,000	Ftu = 154-165,000
T8298 S/N 002 90Ta-10W/Sylcor R512 Disilicide Post Coating Treatment - None	.076 .0025 ± .0005	1.9360/1.9352	1.9365/1.9365	No permanent set * Δ Dia. = .0005-.0013. Max. dynamic strain = .004. No. of impact loads = 10	P_K = 6500 PRR = 250 $P_{s.g}$ = 12,000	120,000	
T13343-1 S/N 001 C-103/Durak KA Disilicide Post Coating Treatment-2500°F, 2 1/2 hr. Air	.100 .0035 - .0040	1.9850/1.9849	1.9850/1.9850	No permanent set Max. dynamic strain = .0042. No. of impact loads = 7	P_K = 7750 PRR = 250 $P_{s.g}$ = 10,600	106,000	Ftu = 137-148,000
T13343-1 S/N 002 C-103/ Durak KA Disicilide Post Coating Treatment-2500°F, 2 1/2 Hr. Air	.100 .0035 - .0040	1.9862/1.9859	1.9865/1.9875	No permanent set Max. dynamic strain = .0044. No. of impact loads = 32	P_K = 8500 PRR = 200 $P_{s.g}$ = 11,150	115,000	
T13343-501 S/N 003 C-103/Vapor Dep. W + Sylcor R508C (Aluminide) Post Coating Treatment - None	.100 W = .0025 R508C = .0035	1.9870/1.9880	1.9870/1.9880	No permanent set Max. dynamic strain = .0053. No. of impact loads = 16	P_K = 6600 PRR = 200 $P_{s.g}$ = 14,300	143,000	Ftu = 121-136,000
T-13343-501 S/N 004 C-103/Vapor Dep. W + Sylcor R508C (Aluminide) Post Coating Treatment - None	.100 W = .0025 R508C = .0035	1.9860/1.9865	1.9860/1.9866	No permanent set Max. dynamic strain = .0037. No. of impact loads = 34	P_K = 7700 PRR = 210 $P_{s.g}$ = 11,000	110,000	

*Variation of Measurements are Within Coating Tolerances

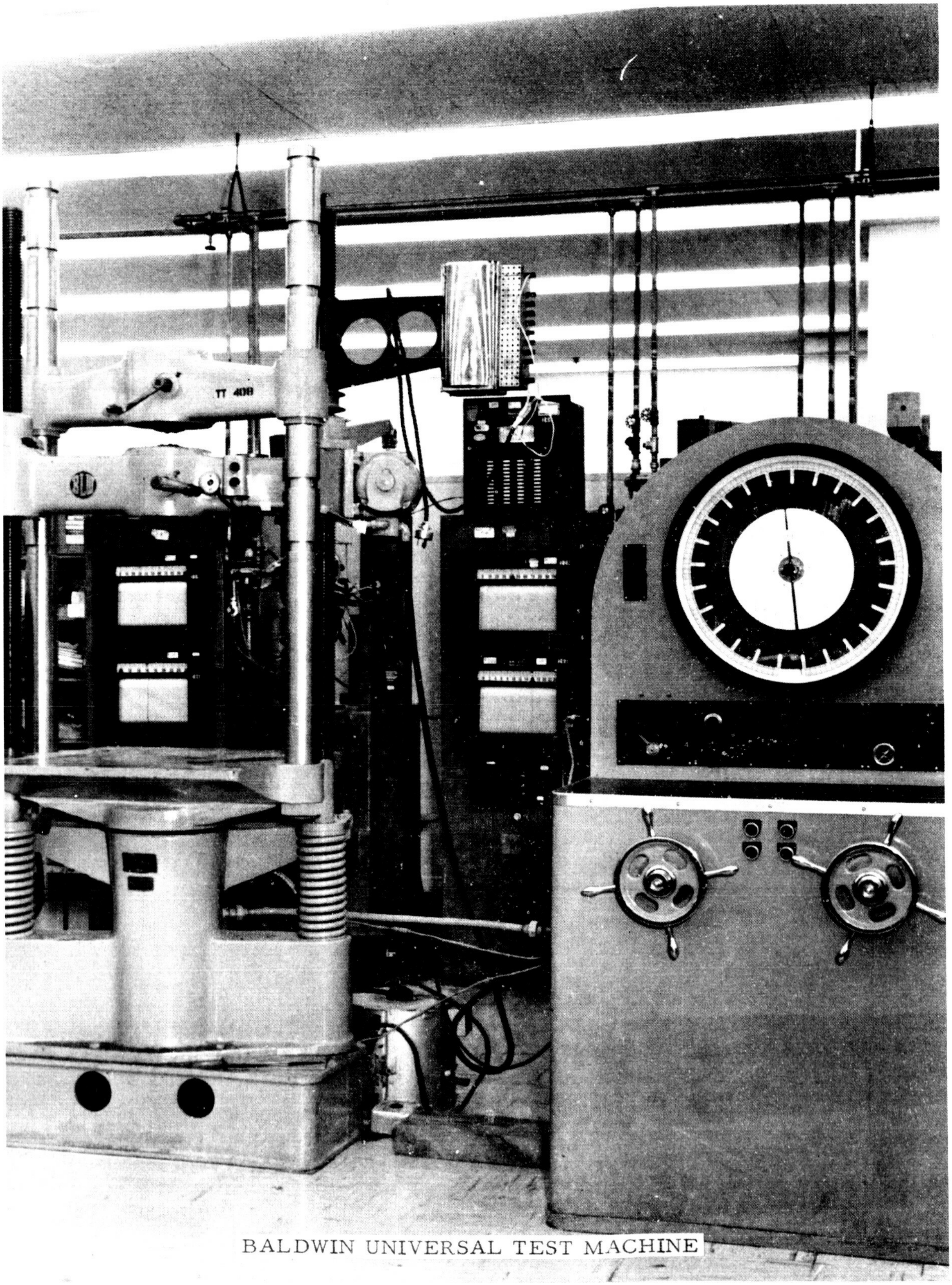

BALDWIN UNIVERSAL TEST MACHINE

FIGURE 1

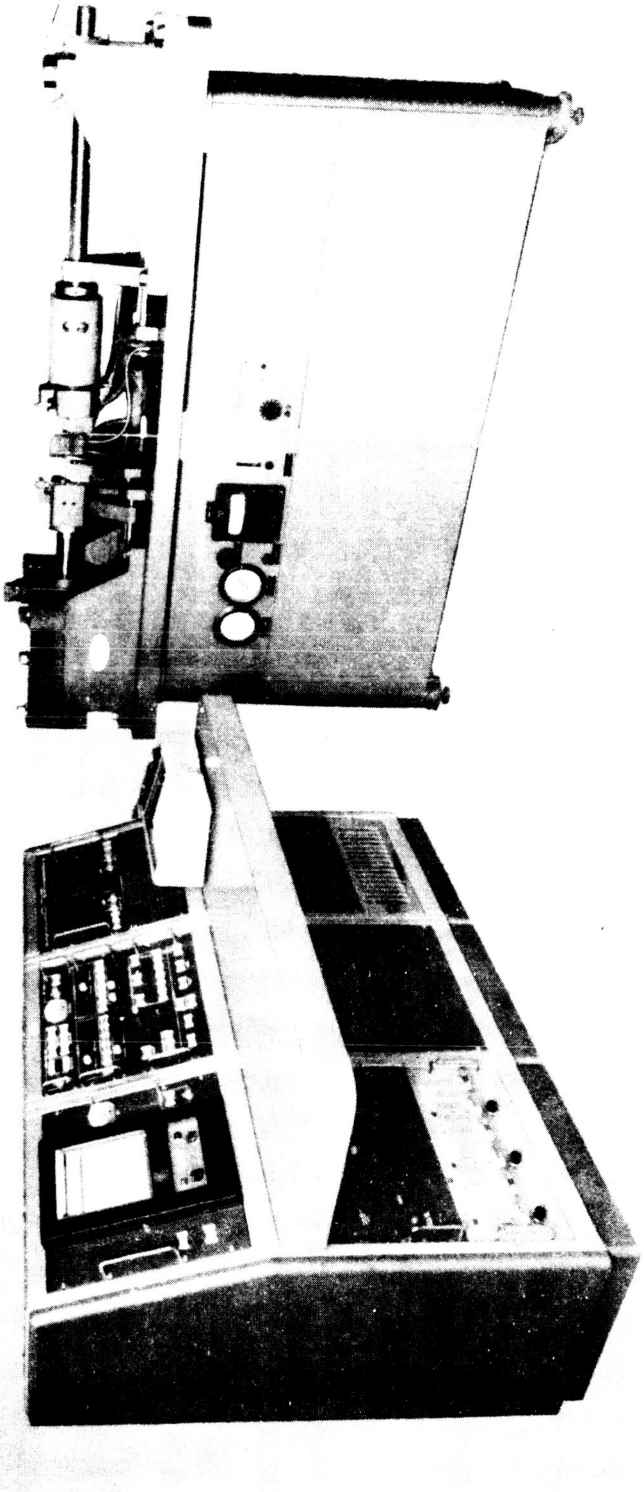

TM-1 TENSILE TEST MACHINE

NEG. CA 2936-2

FIGURE 2

OPTRON HIGH SPEED TENSILE TESTING MACHINE

NEG. C6983-3

FIGURE 3

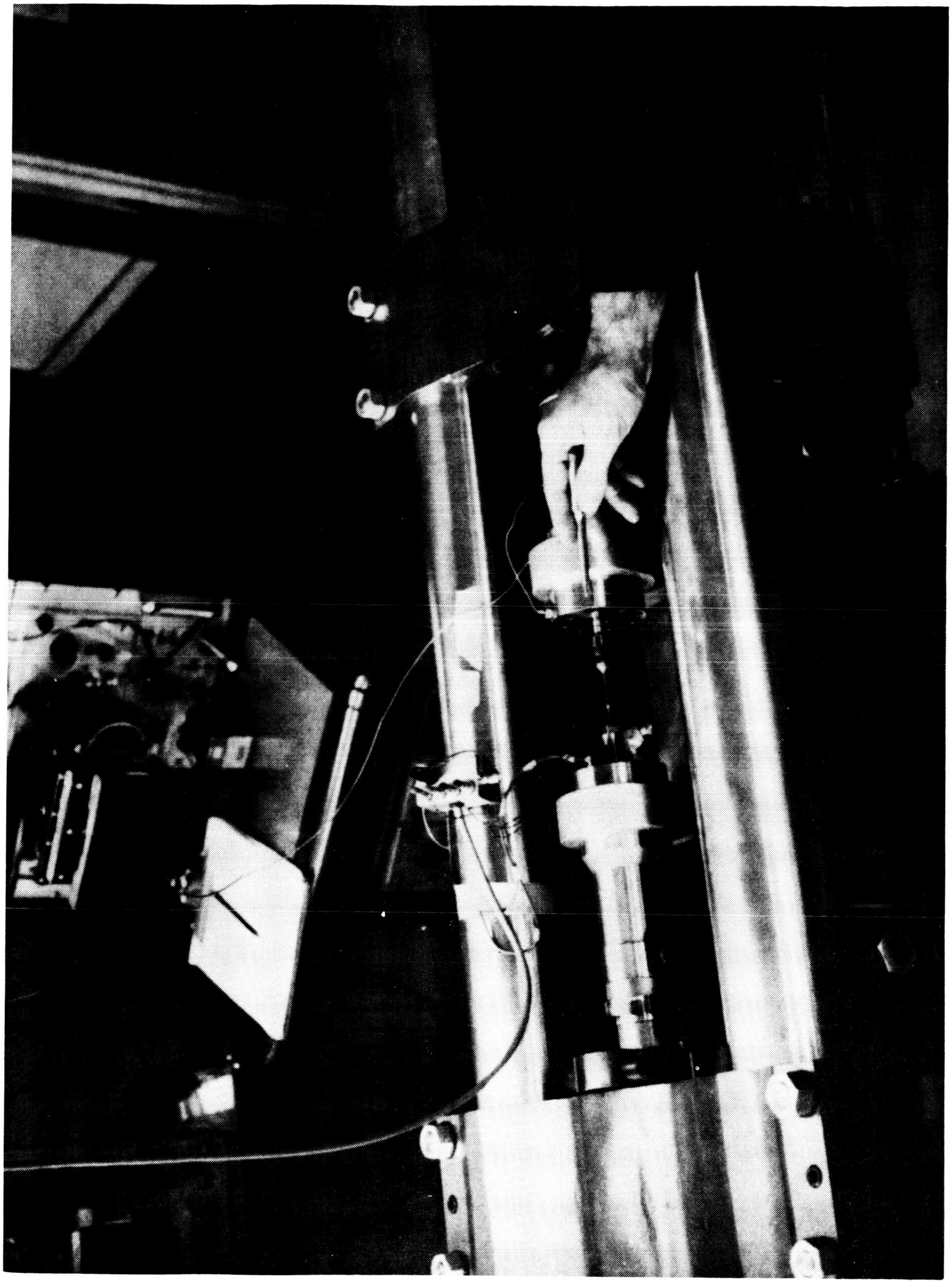

NEG. C6983-2

OPTRON HIGH SPEED TENSILE TESTING MACHINE

FIGURE 4

628
C-103/Durak KA
-100°F

Filtered Data

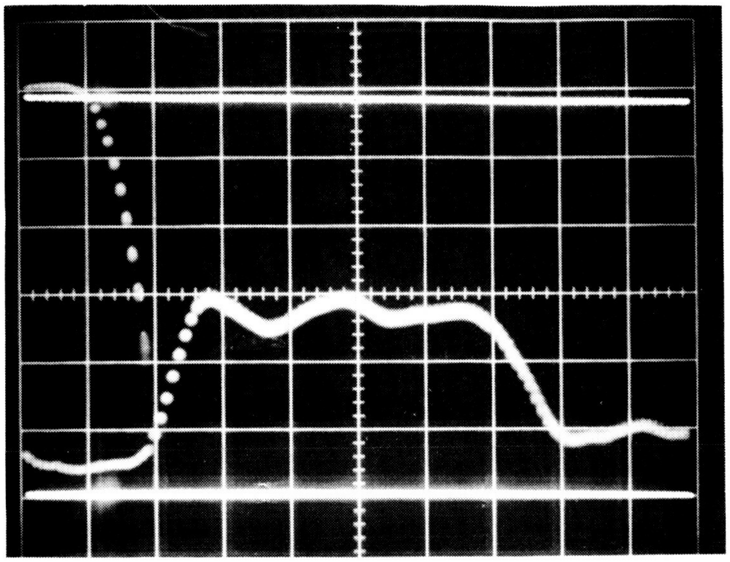

e = 4 x 10^{-4} in/in/div

p = 538 lbs/div

t = 5 X 10^{-5} sec/div

Raw Data

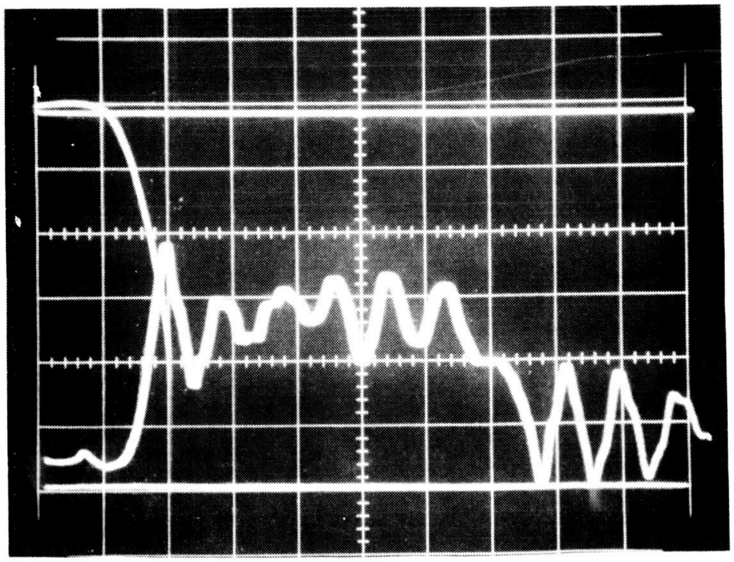

e = 4 x 10^{-3} in/in/div

p = 538 lbs/div

t = 5 X 10^{-5} sec/div

TYPICAL HIGH STRAIN RATE TEST OSCILLOSCOPE TRACE

FIGURE 5

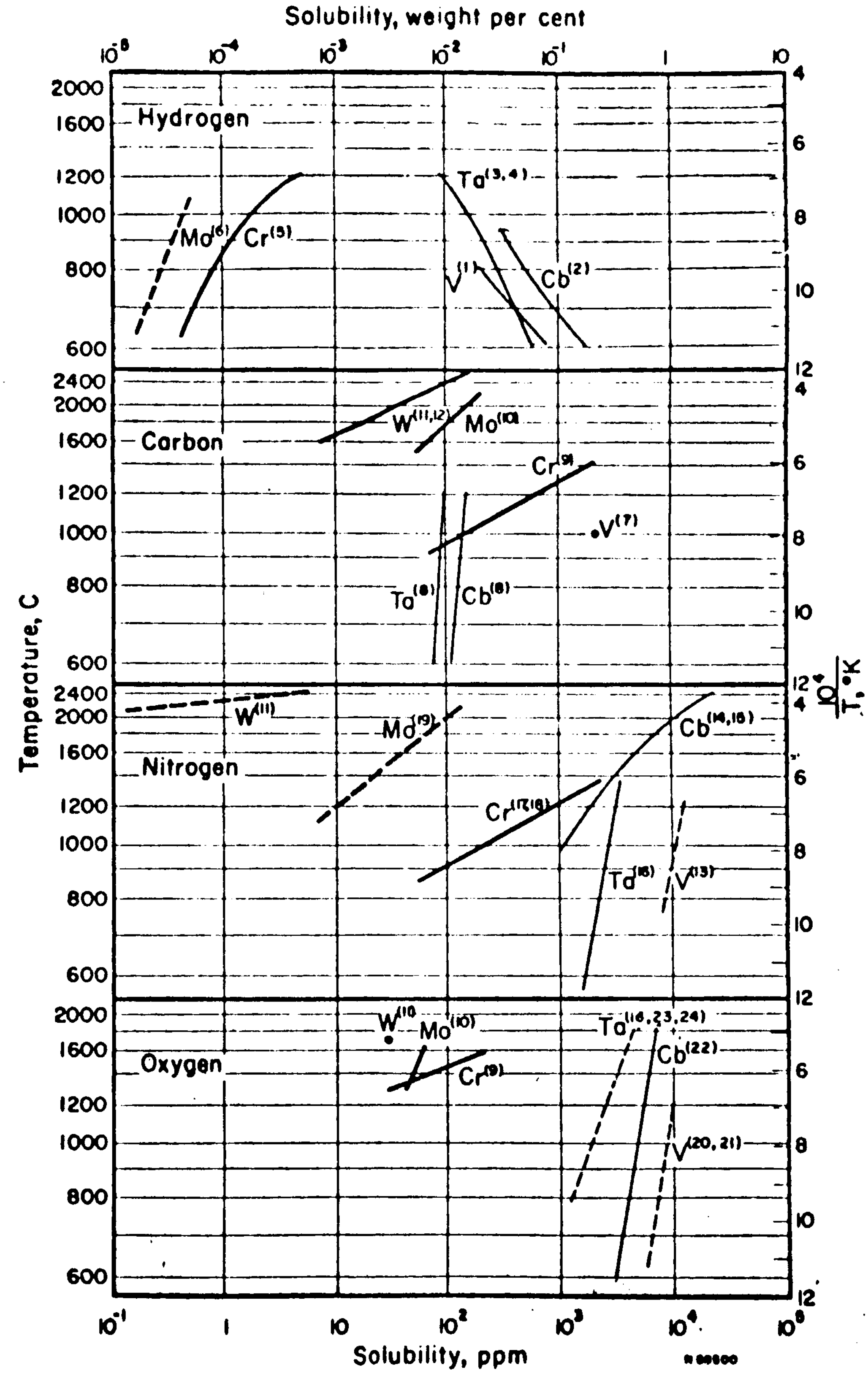

SOLUBILITIES OF INTERSTITIALS IN
GROUP VA AND VI-A METALS

BATTELLE MEMORIAL INSTITUTE

FIGURE 6

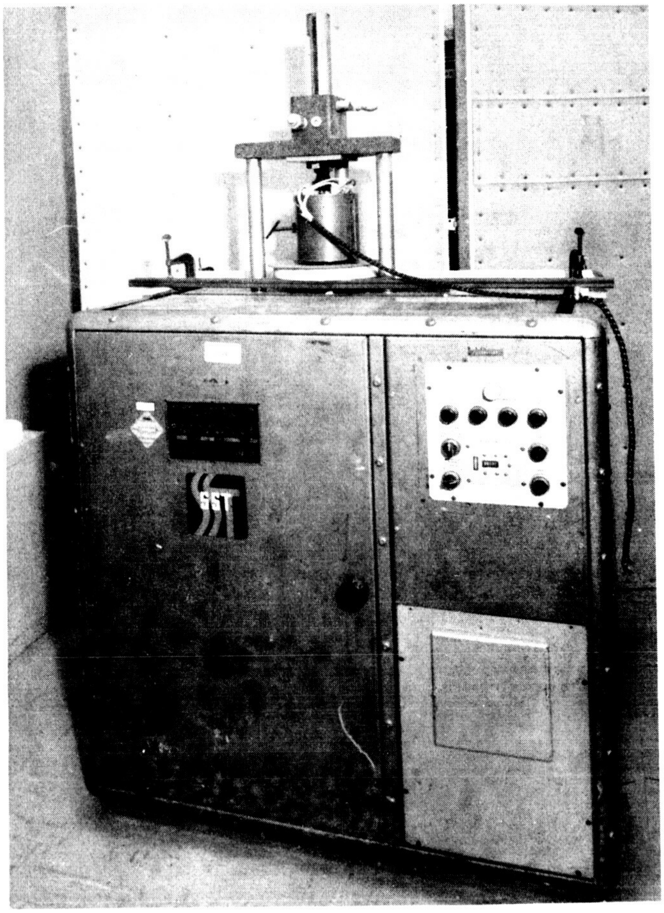

FATIGUE TEST MACHINE

FIGURE 7

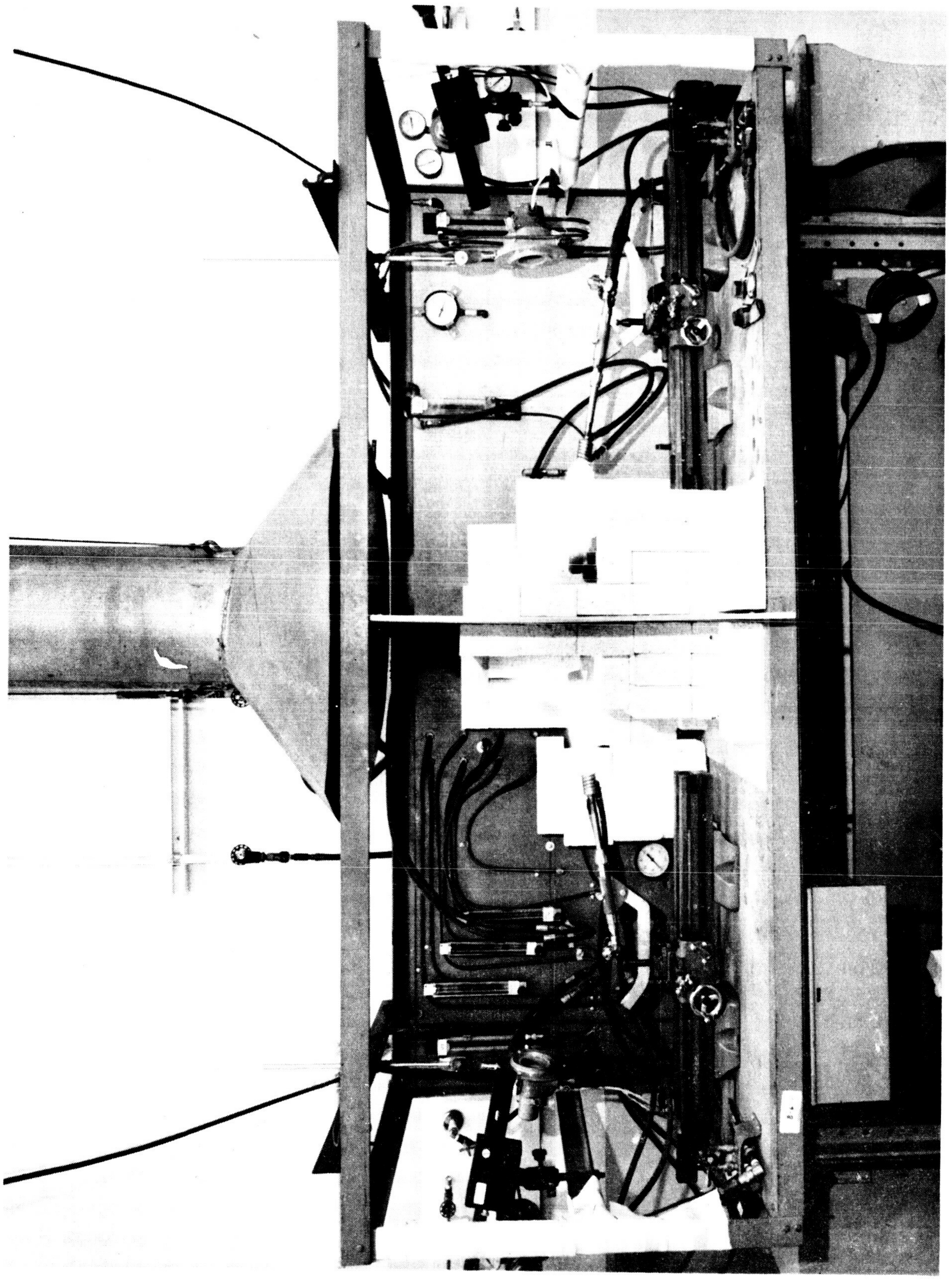

COATING THERMAL TEST MACHINE

FIGURE 8

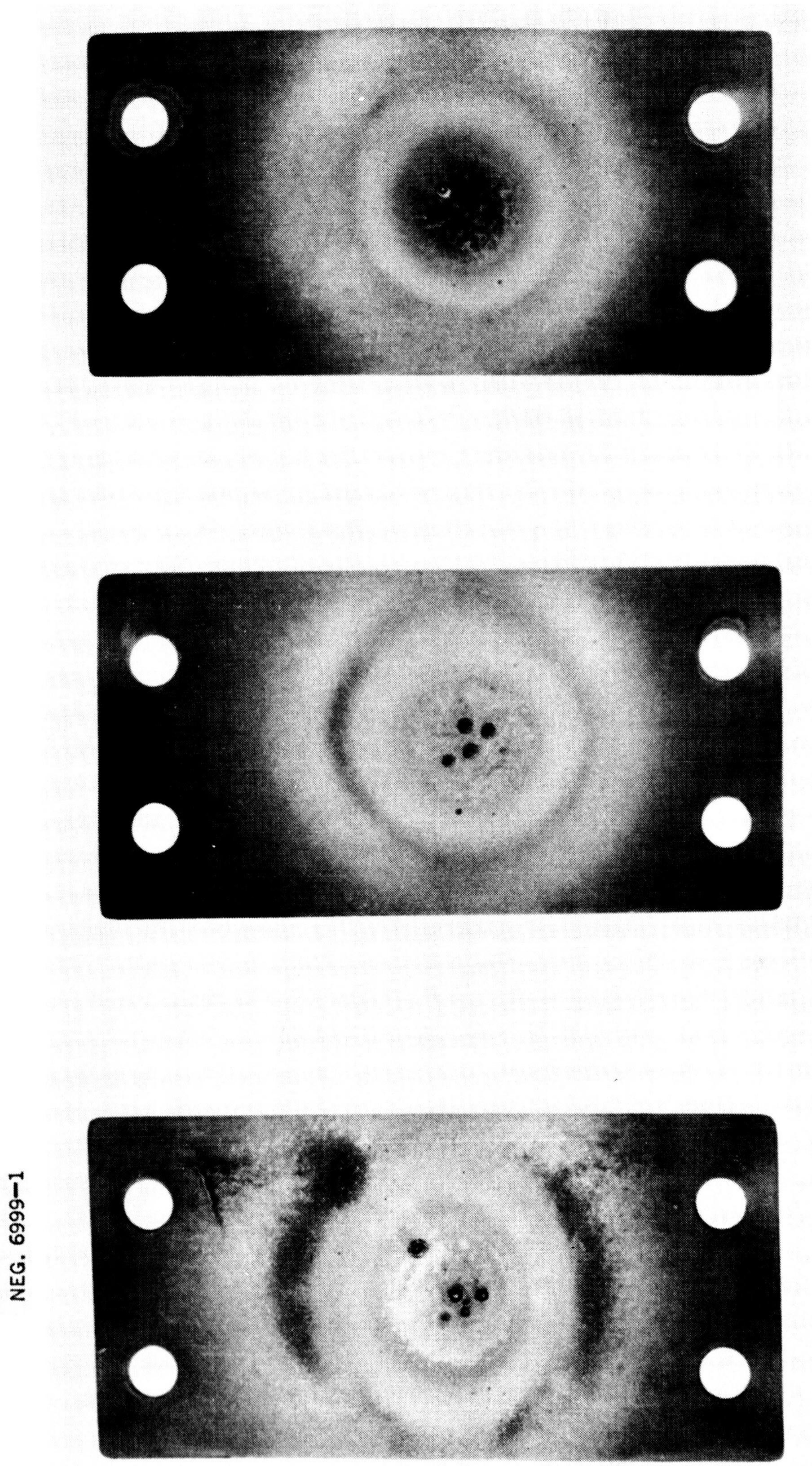

90Ta-10W/R512 After Torch Testing

FIGURE 9

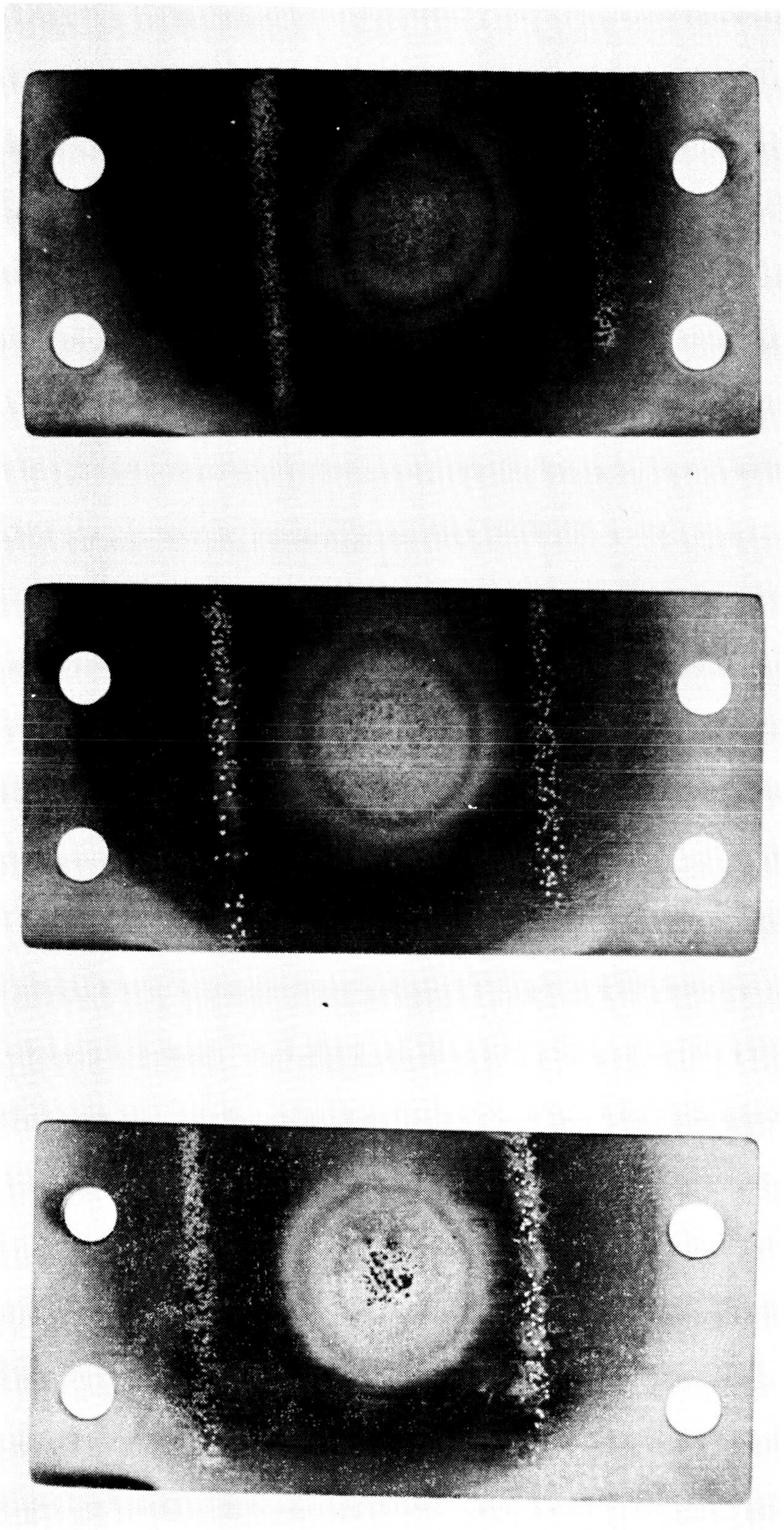

C-103/DURAK KA AFTER TORCH TESTING

FIGURE 10

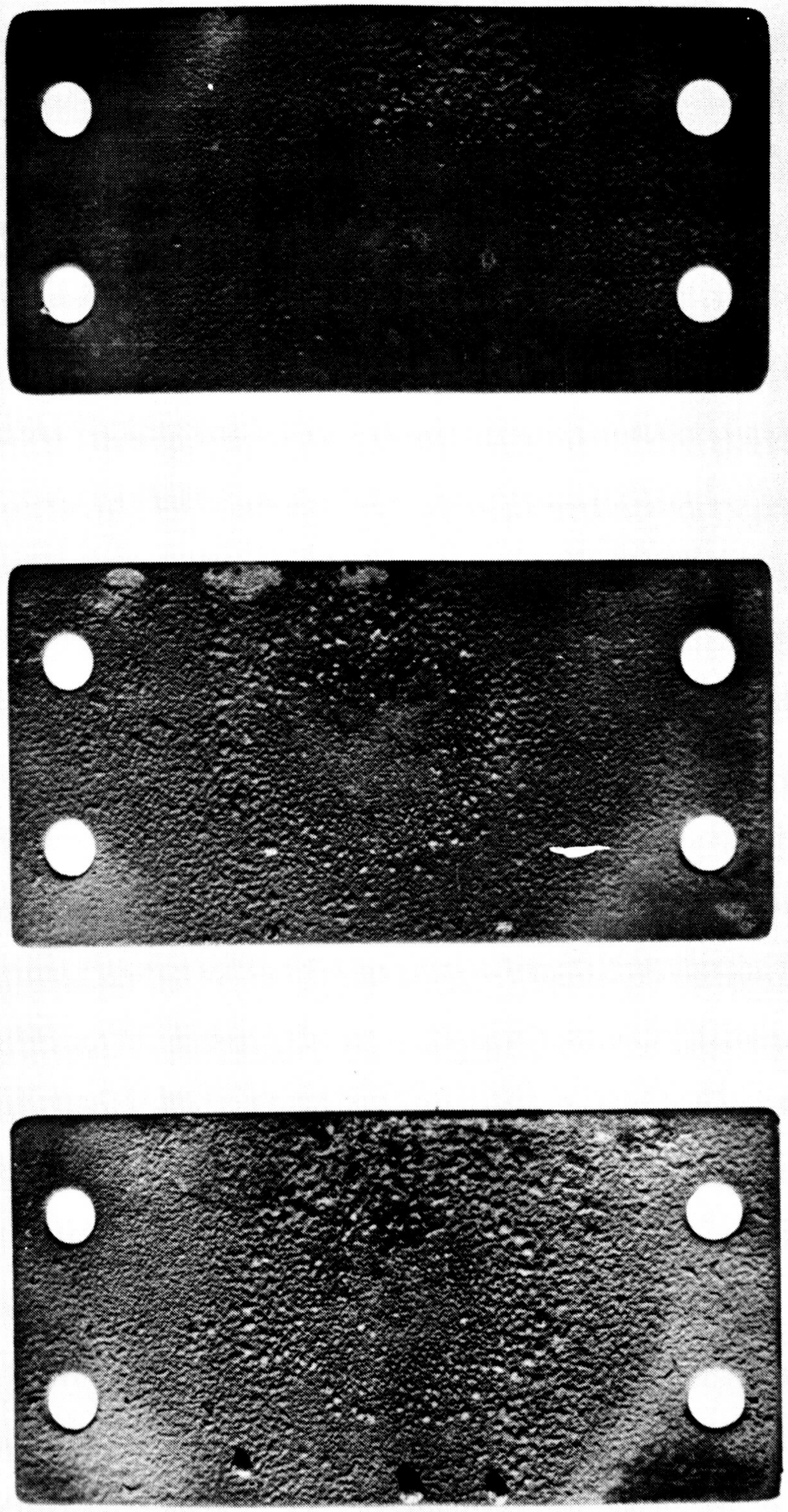

NEG. 6999-4

C-103/W + R508C AFTER TORCH TESTING

FIGURE 11

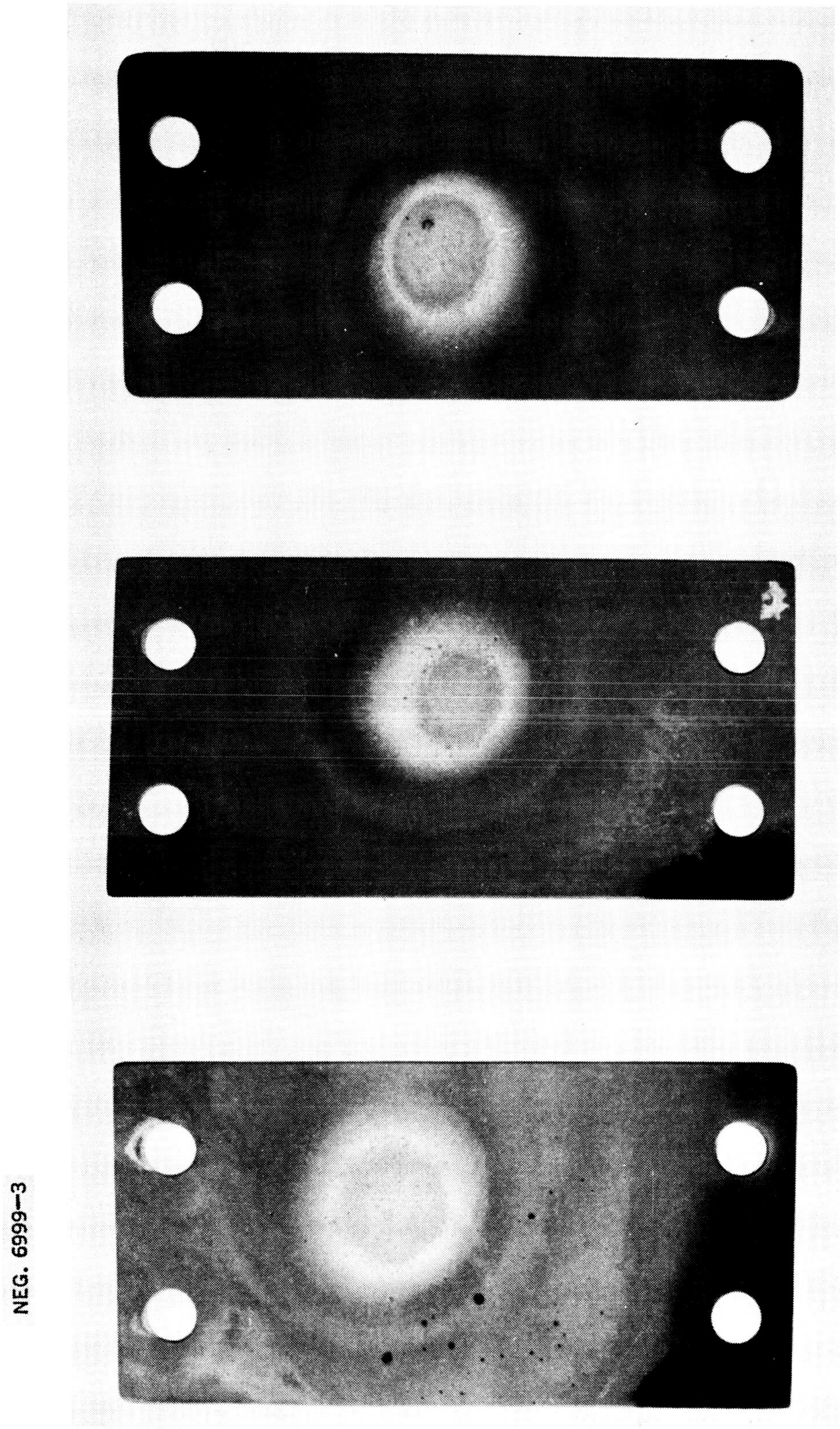

C-129Y/DURAK KA AFTER TORCH TESTING

FIGURE 12

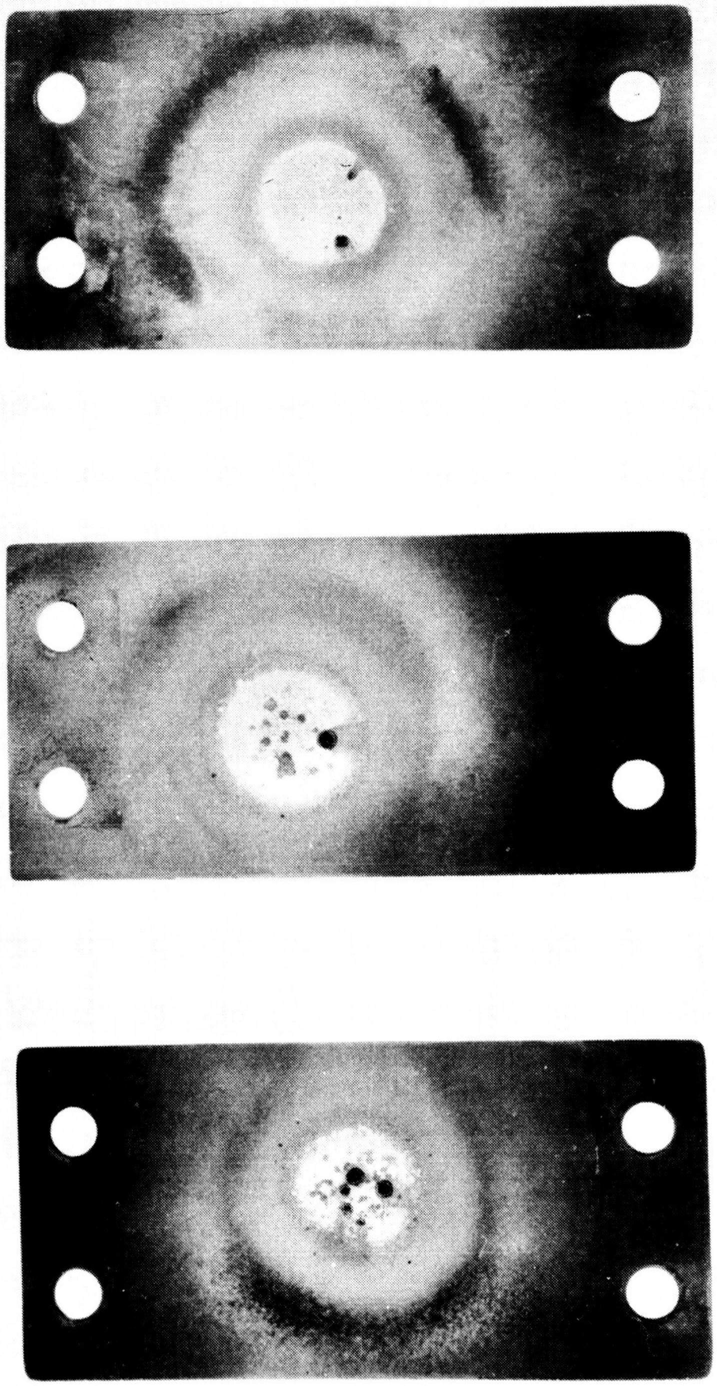

NEG. 7018-1

90Ta-10W/512 AFTER FATIGUE-TORCH TESTING

FIGURE 13

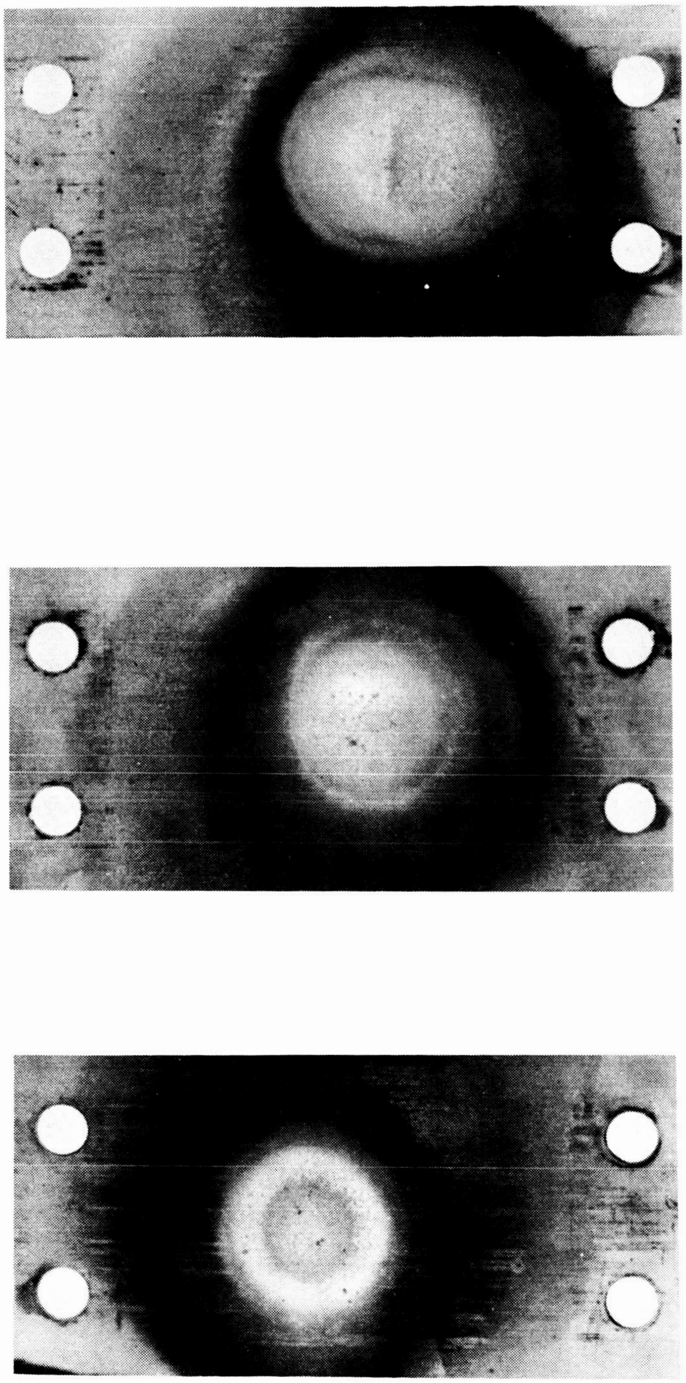

NEG. 7018–2

C-103/DURAK KA AFTER FATIGUE-TORCH TESTING

FIGURE 14

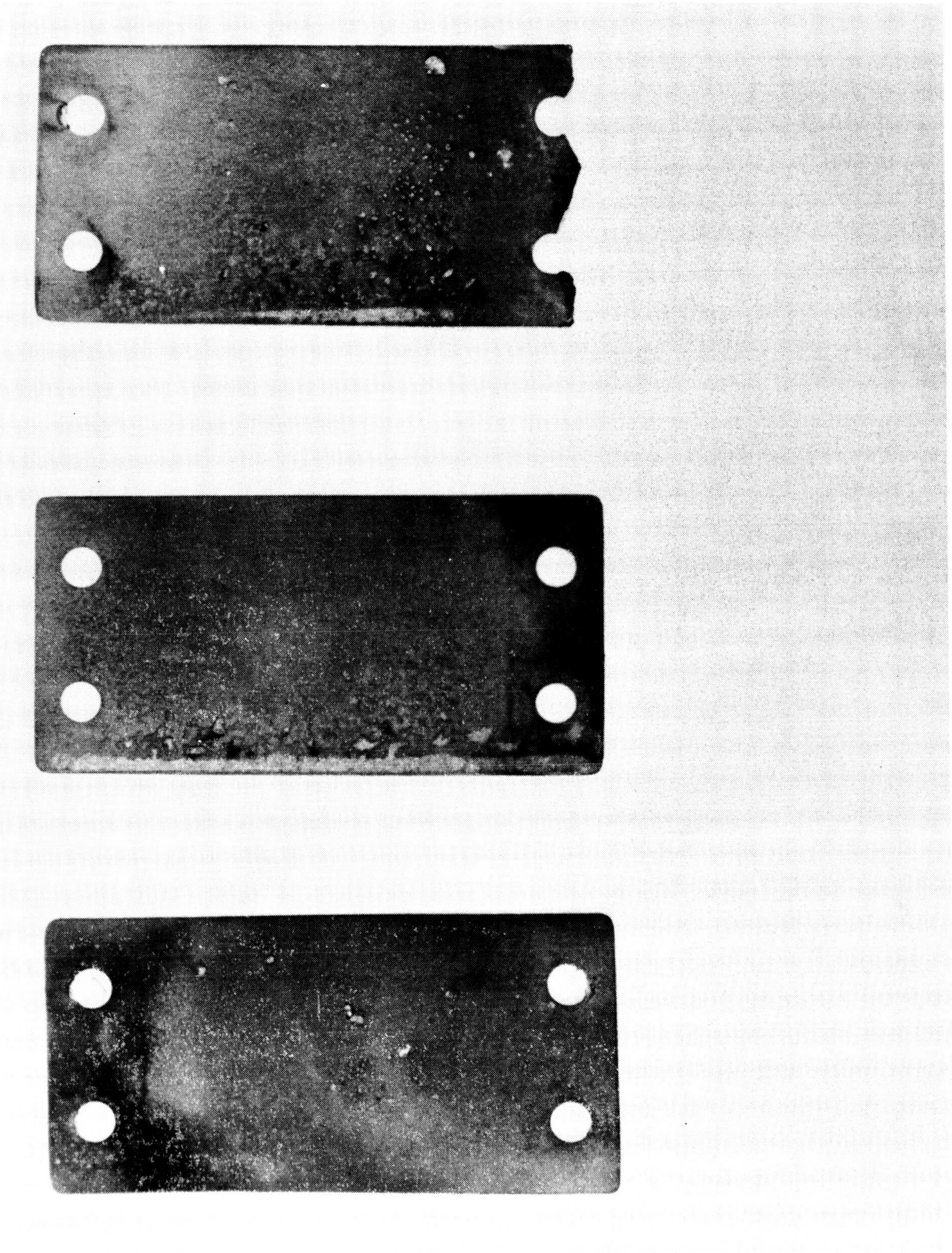

NEG. 7018-4

C-103/W + R508C AFTER FATIGUE-TORCH TESTING

FIGURE 15

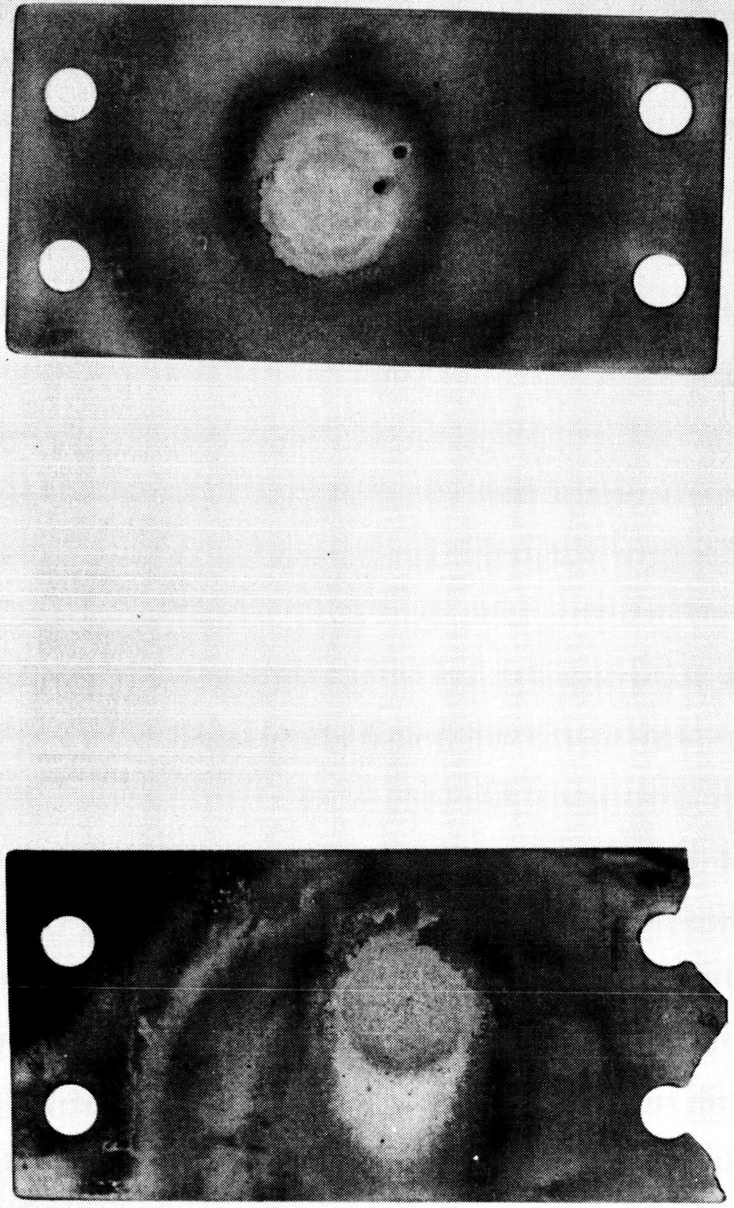

NEG. 7018-3

C-129Y/DURAK KA AFTER FATIGUE-TORCH TESTING

FIGURE 16

NEG. 7011-1

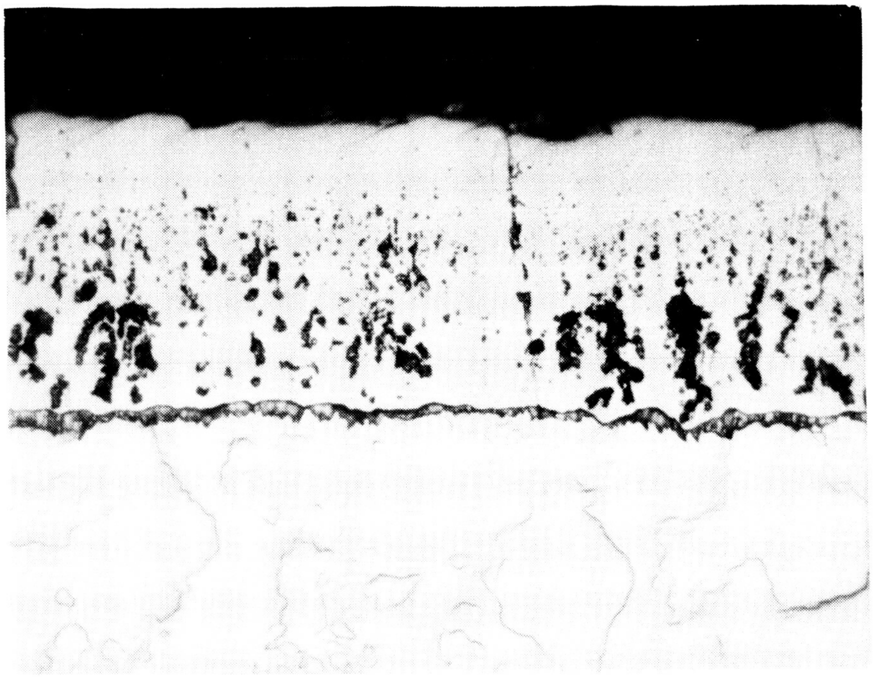

(a) MOLYBDENUM/DURAK B

NEG. 7011-2

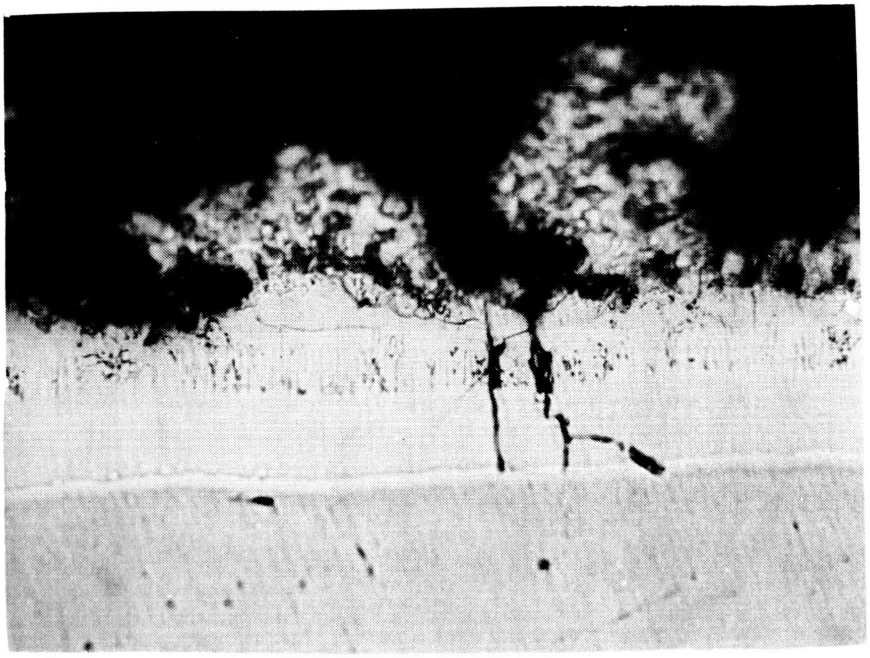

(b) 90Ta-10W/R512

COATED SPECIMENS AFTER TENSILE TEST - 500X

FIGURE 17

NEG. 7011-3

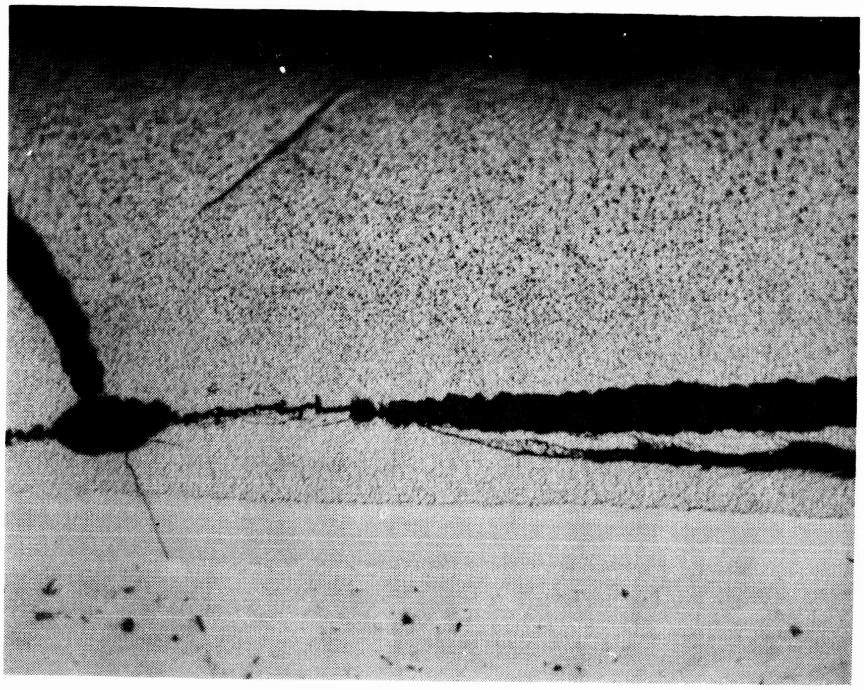

(a) C-103/DURAK KA

NEG. 7011-4

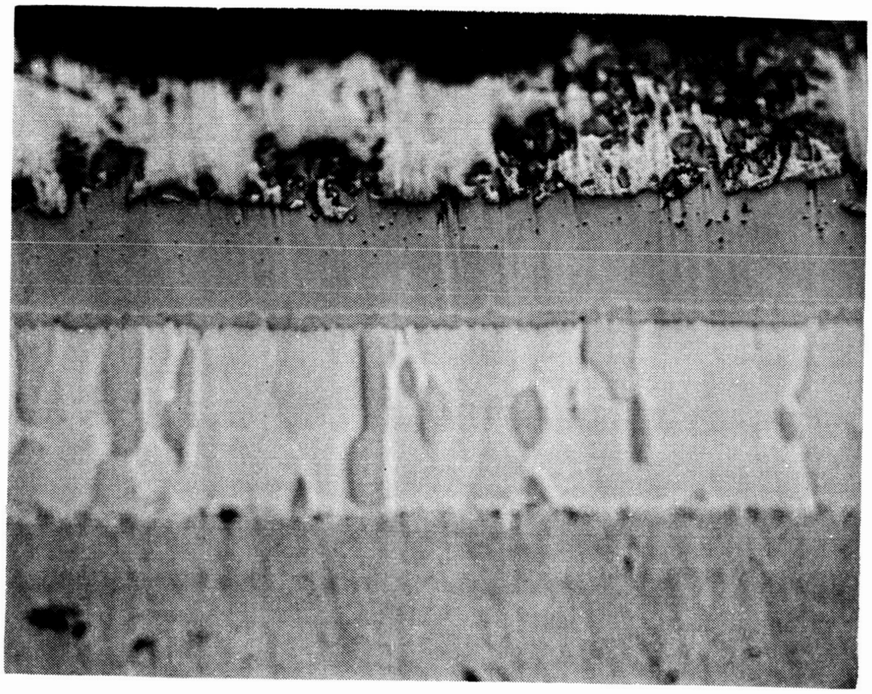

(b) C-103/W + R508C

COATED SPECIMENS AFTER TENSILE TESTING - 500X

FIGURE 18

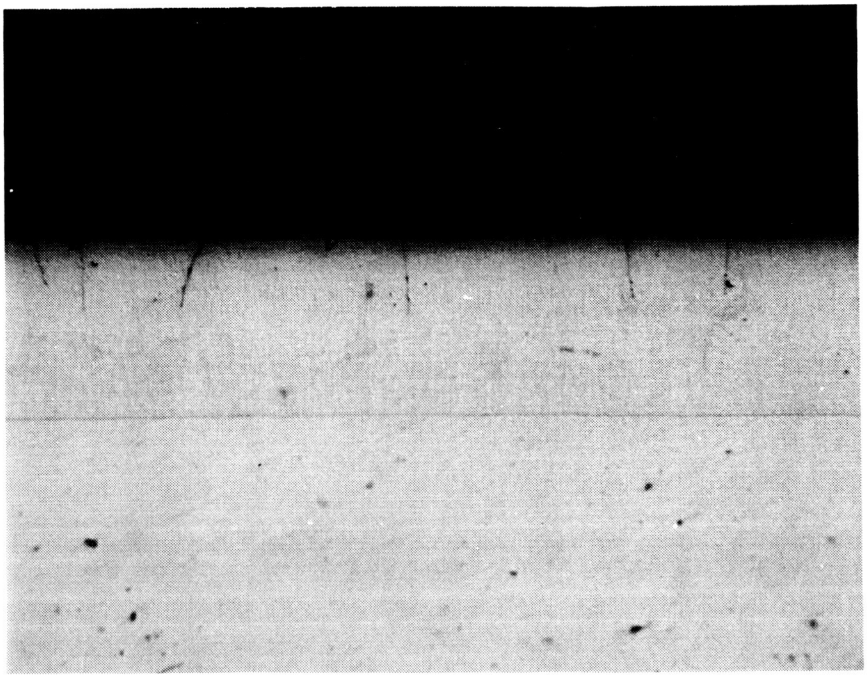

C-129Y/Durak KA Specimen After Tensile Testing - 500X

FIGURE 19

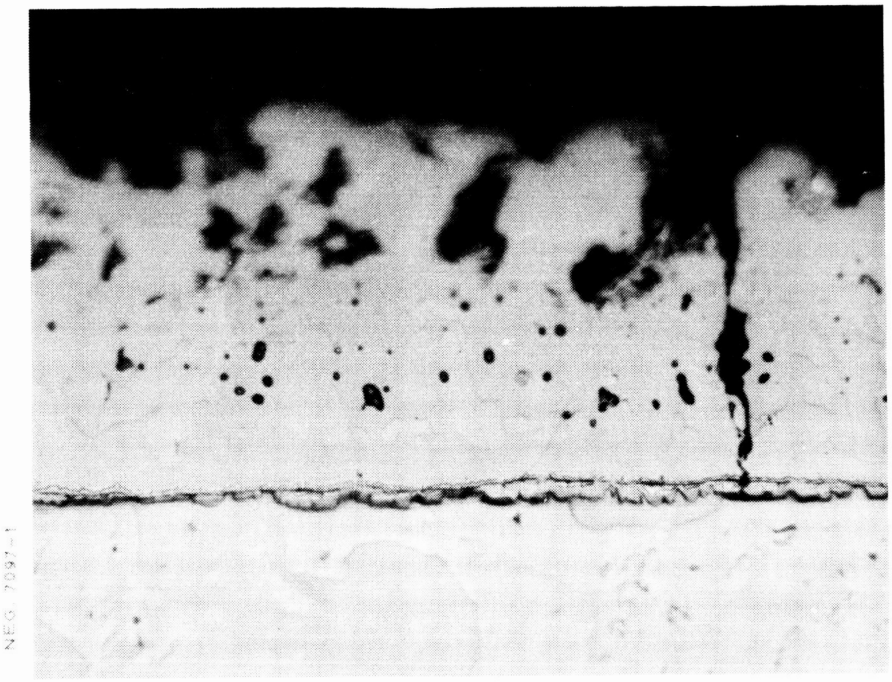

(a) Vacuum-Thermal Cycle

(b) H_2 Thermal Exposure

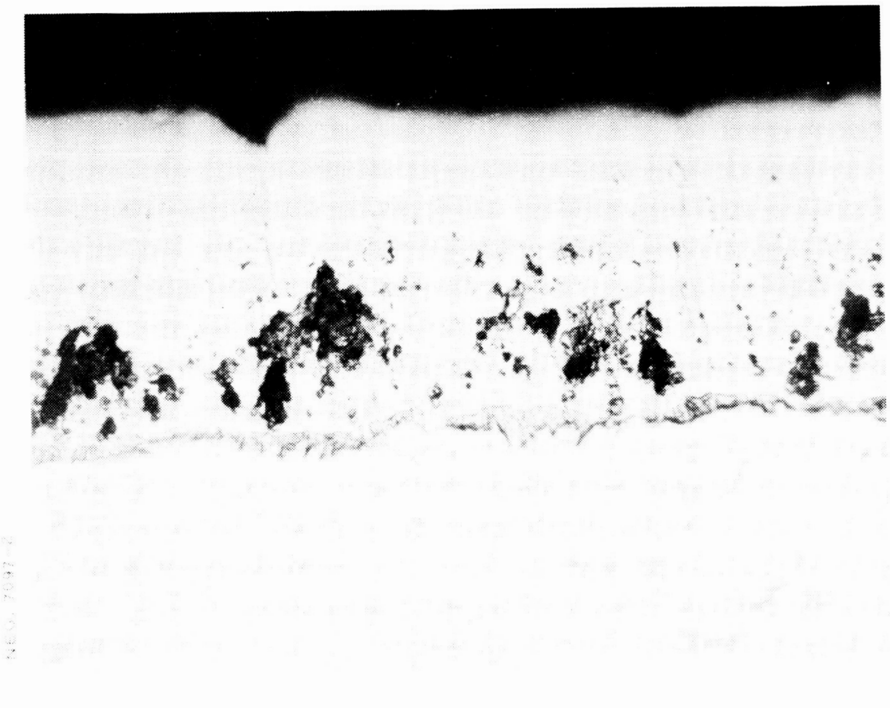

Molybdenum/Durak B After Tensile Testing - 500X

FIGURE 20

(a) Fatigue - Torch

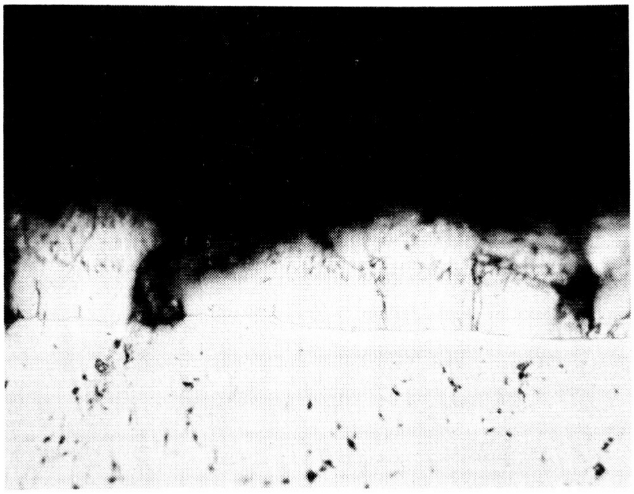

(c) H_2 Thermal Exposure

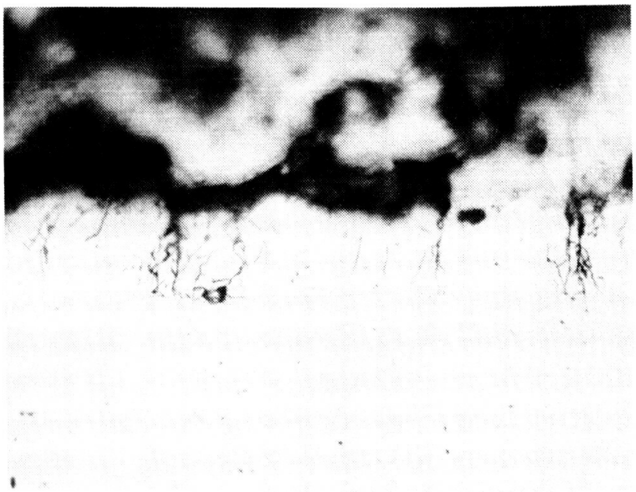

(b) Vacuum Thermal Cycle

90Ta-10W After Tensile Testing - 500X

FIGURE 21

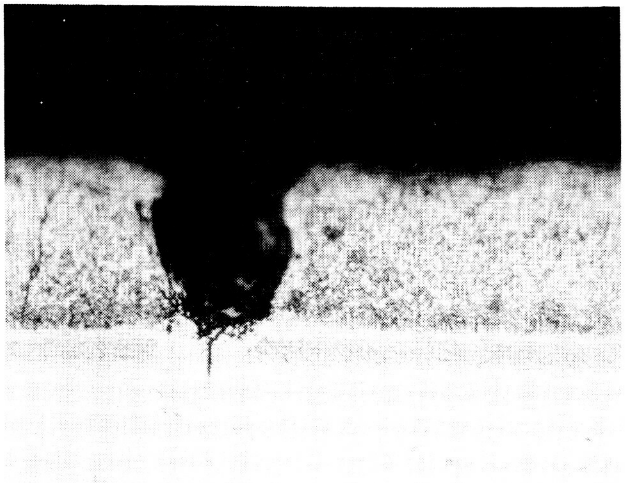

(a) Fatigue - Torch

(b) Vacuum - Thermal Cycle

(c) H_2 Thermal Exposure

C-103/Durak KA After Tensile Testing - 500X

FIGURE 22

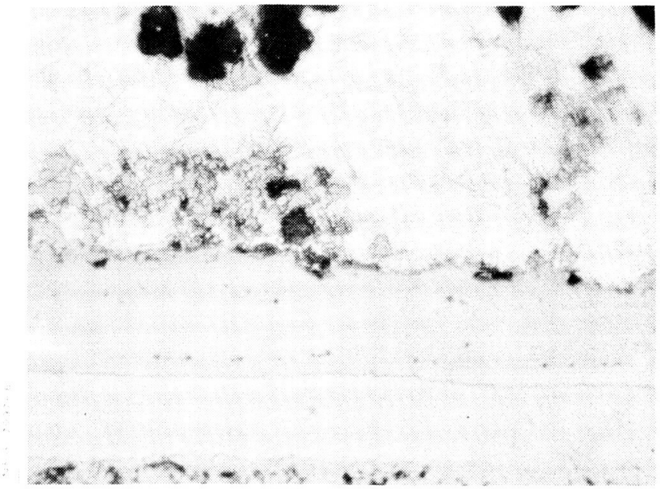

(a) Fatigue - Torch

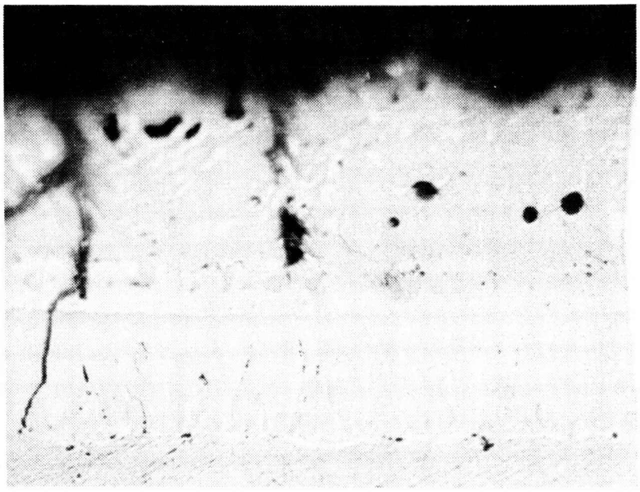

(b) Vacuum - Thermal Cycle

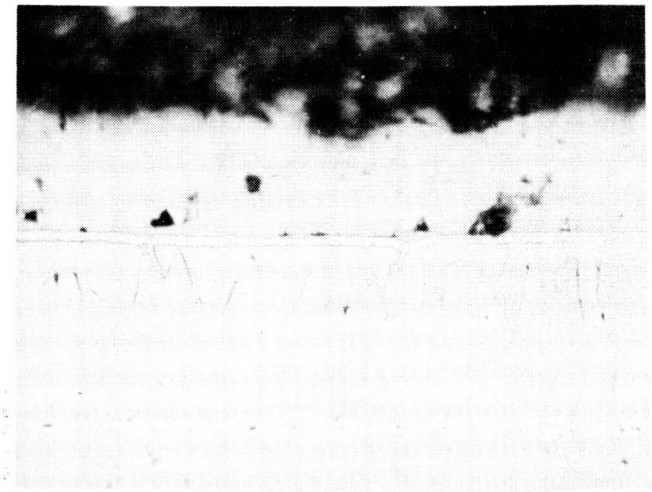

(c) H_2 Thermal Exposure

C-103/W + R508C After Tensile Testing - 500 X

FIGURE 23

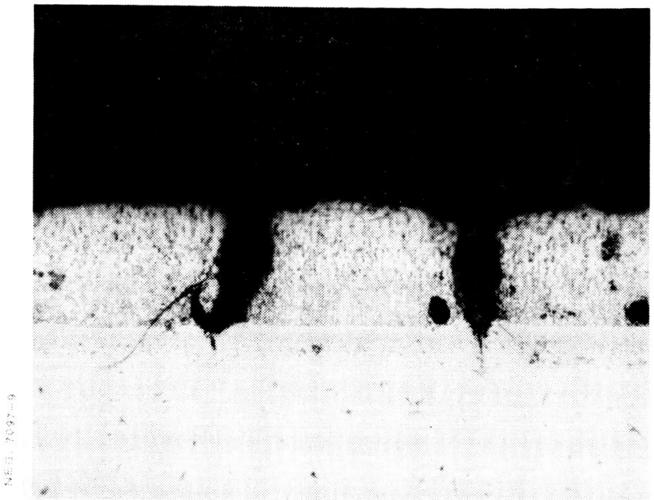

(a) Fatigue - Torch

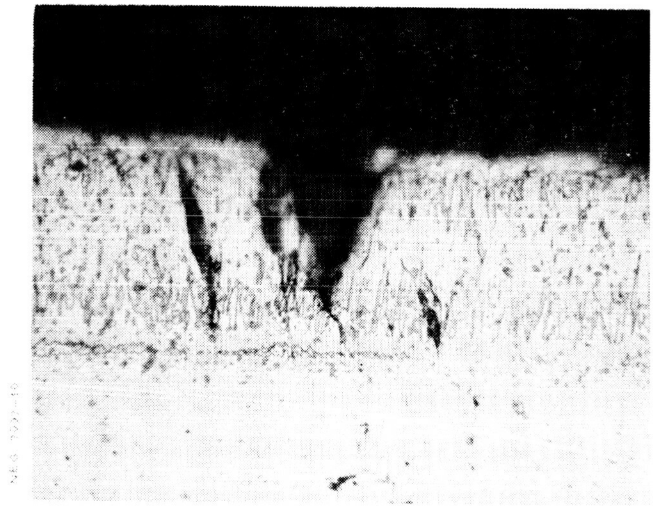

(b) Vacuum Thermal Cycle

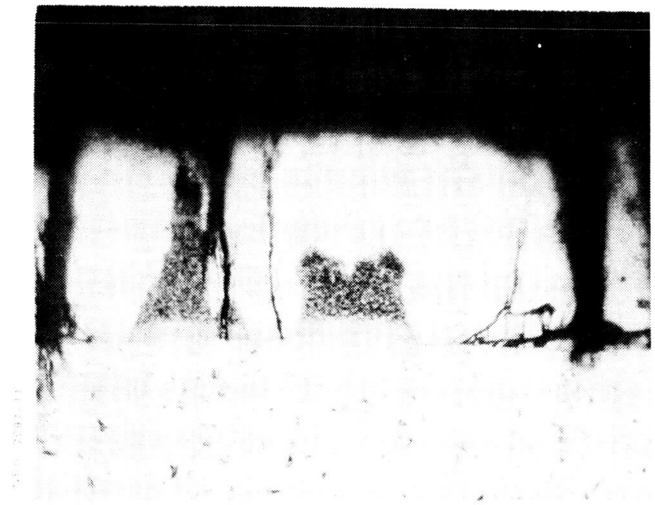

(c) H_2 Thermal Exposure

C-129Y/Durak KA After Tensile Testing - 500X

FIGURE 24

L-605 CHAMBER STRAIN GAGE RISE RATES

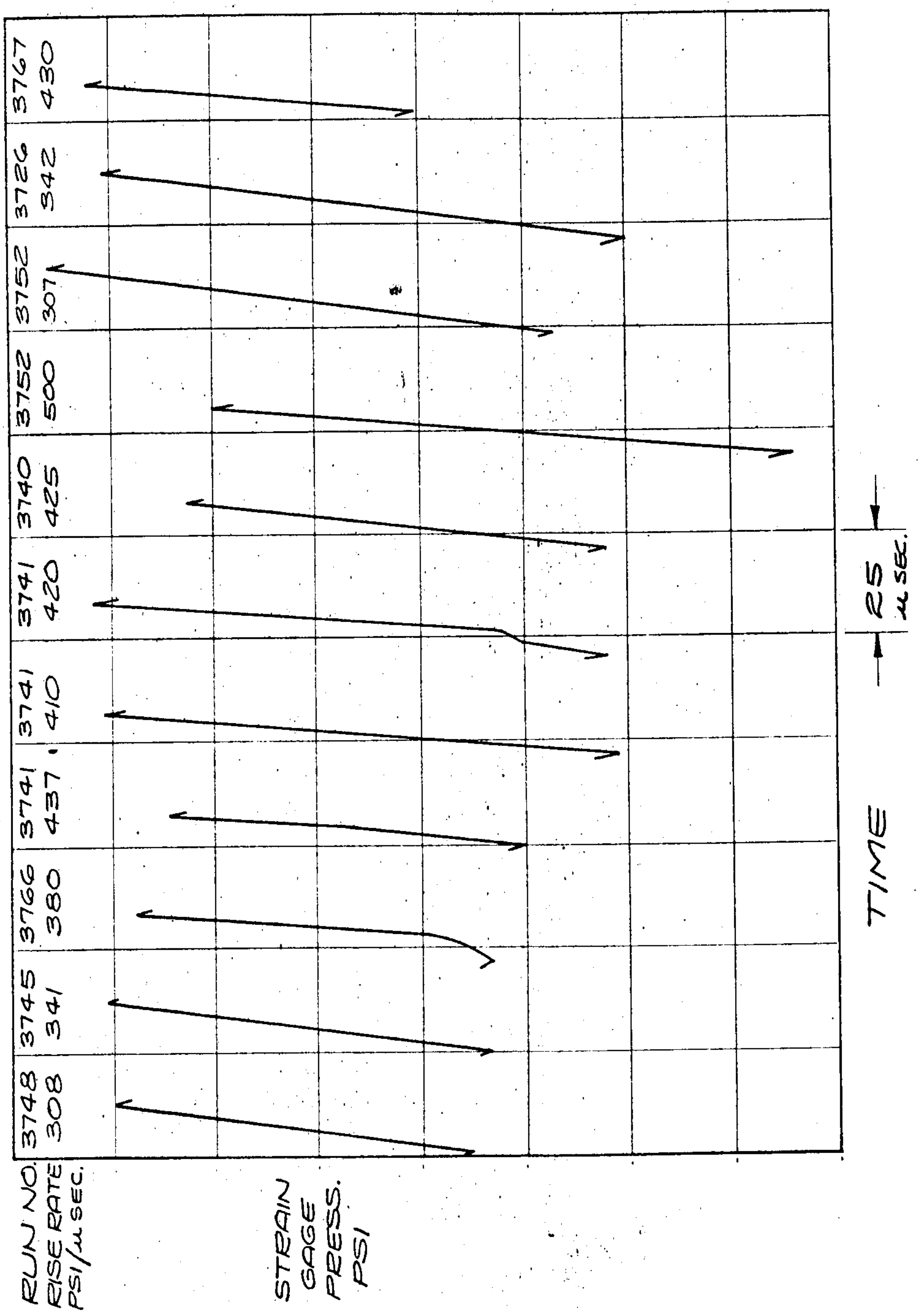

FIGURE 25

L-605 CHAMBER
KISTLER PRESSURE
RISE RATES

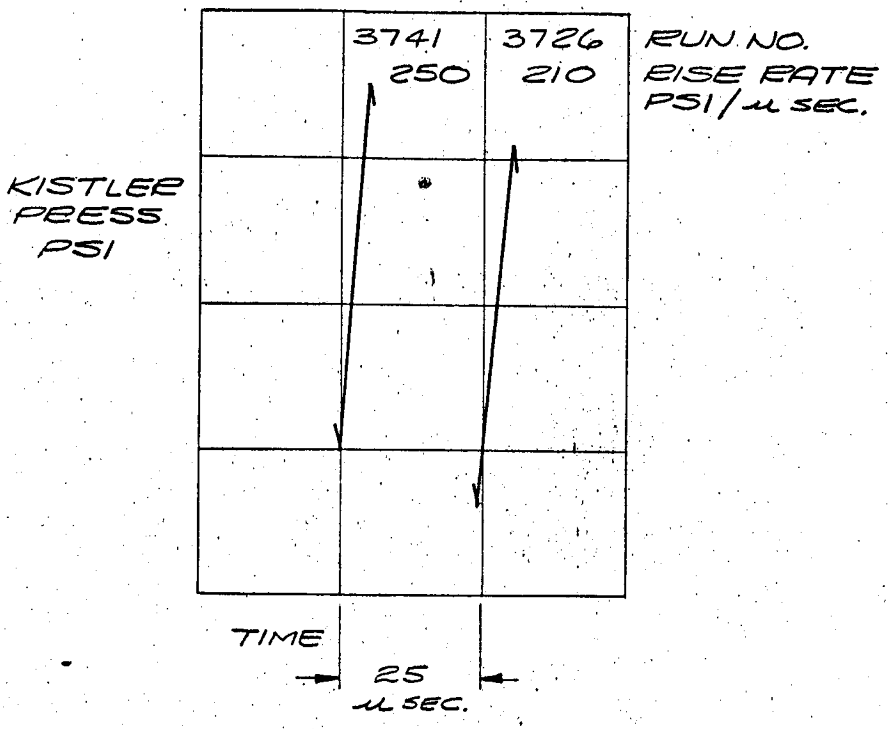

FIGURE 26

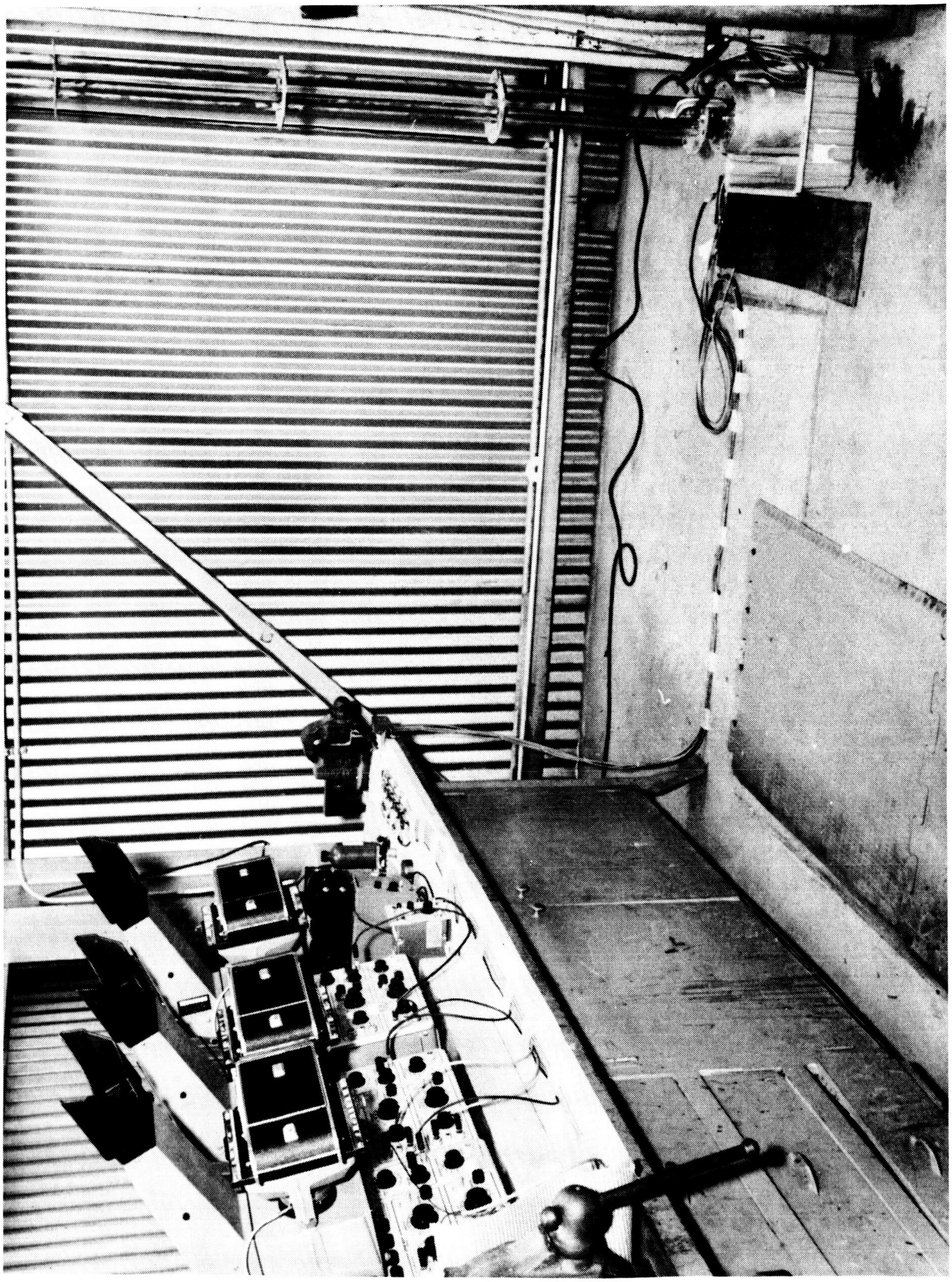

NEG. 6928-4

Chamber Hydraulic Test Setup

FIGURE 27

NEG. 6928-5

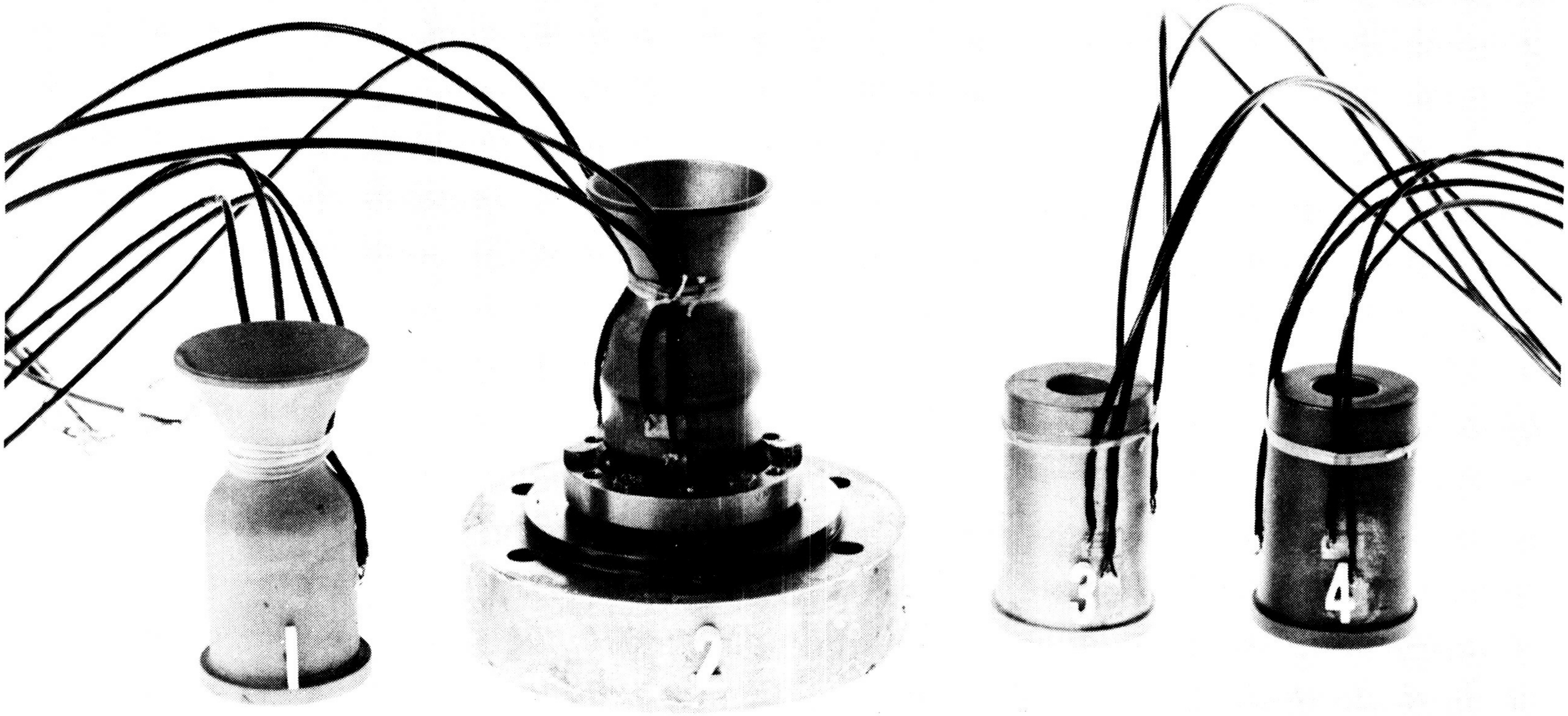

Coated Combustors with Strain Gages

1. 90Ta-10W/R512
2. Molybdenum/Durak B
3. C-103/W + R508C
4. C-103/Durak KA

FIGURE 28

NEG. 6928-2

Molybdenum Chamber

FIGURE 29

NEG. 6928-3

C-103 Chamber

FIGURE 30

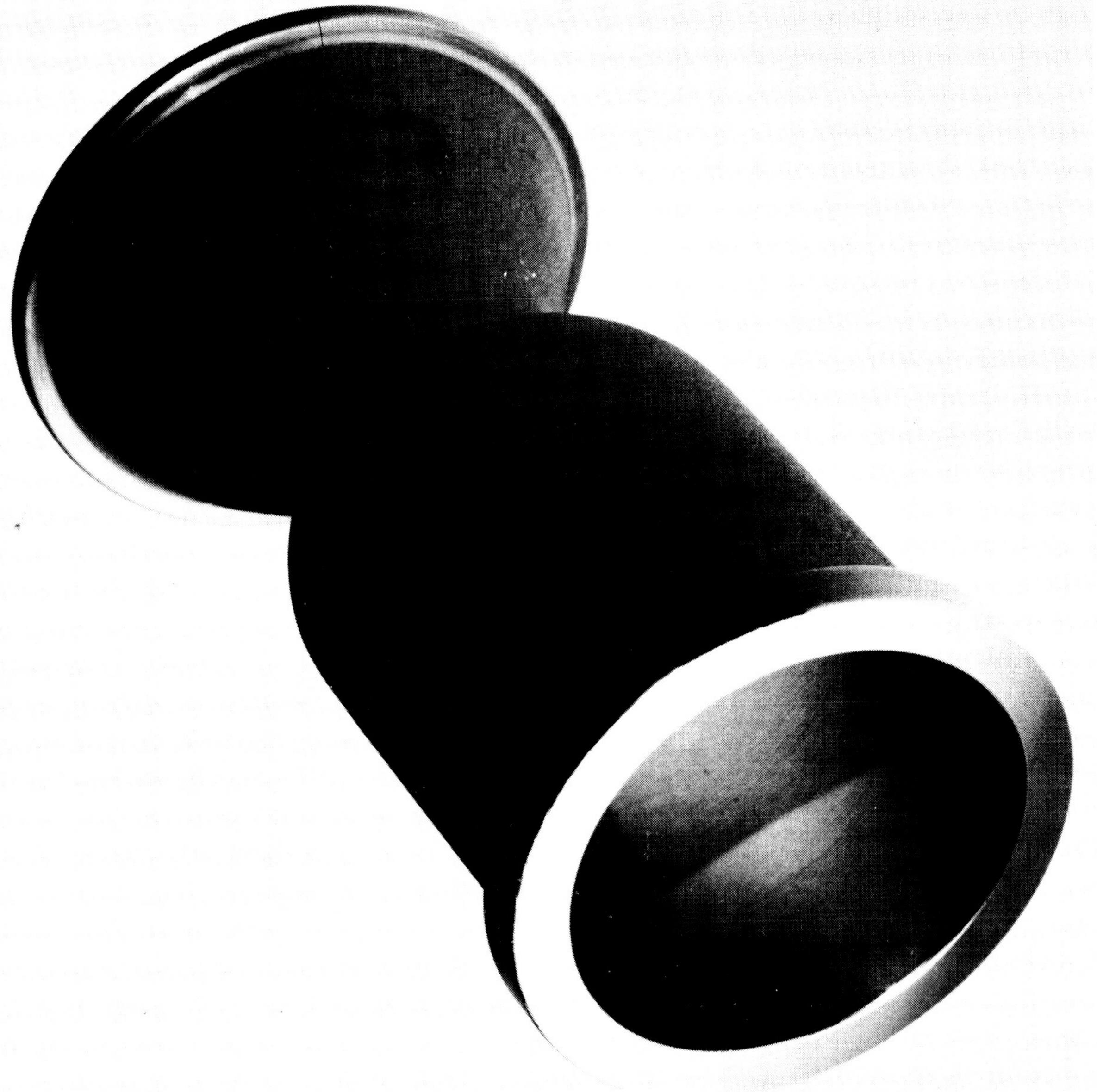

NEG. 6928-1

90Ta-10W Chamber

FIGURE 31

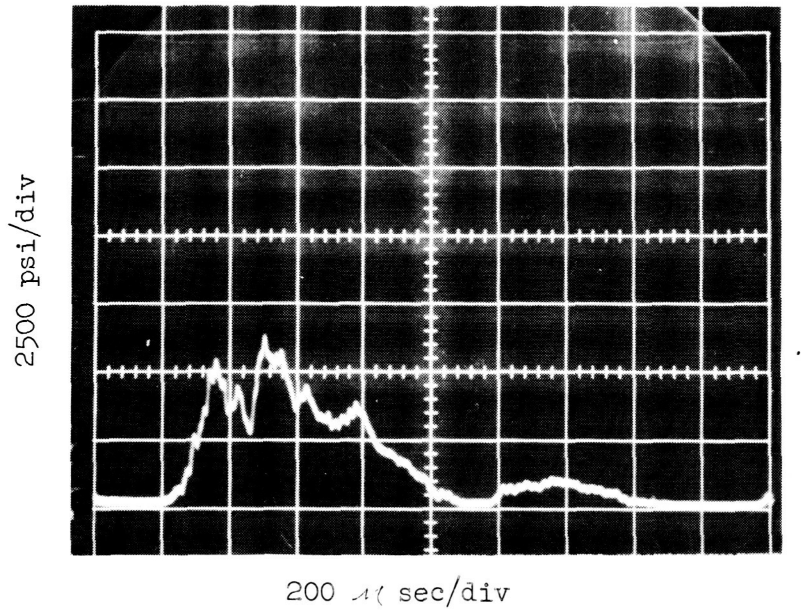

Kistler Transducer Pressure

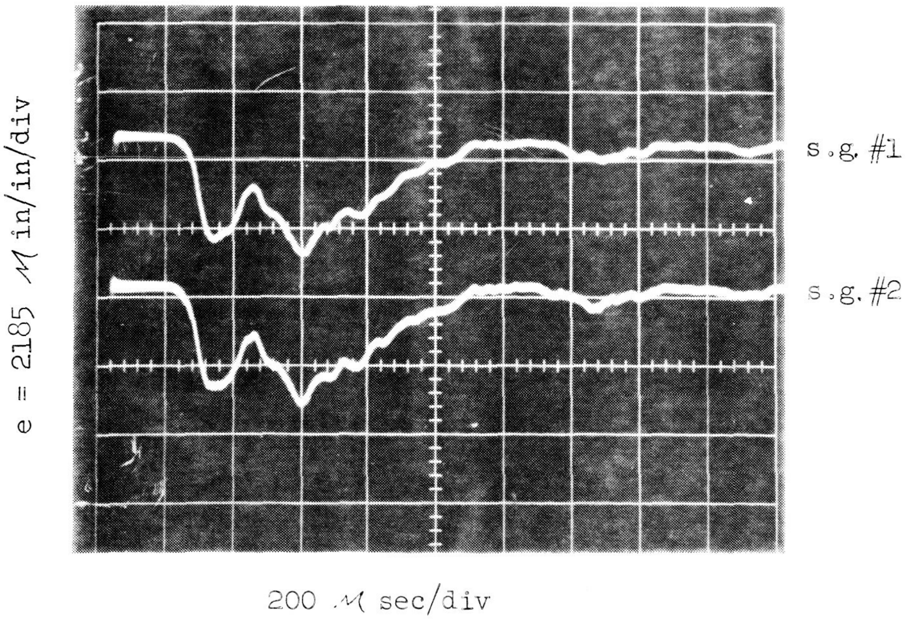

Strain Gage Trace

Typical Hydrodynamic Chamber Test Oscilloscope Trace

FIGURE 32

NEG. 6928-6

Hydrodynamically Burst Molybdenum/Durak B Chamber

FIGURE 33

NEG. CT3322-79

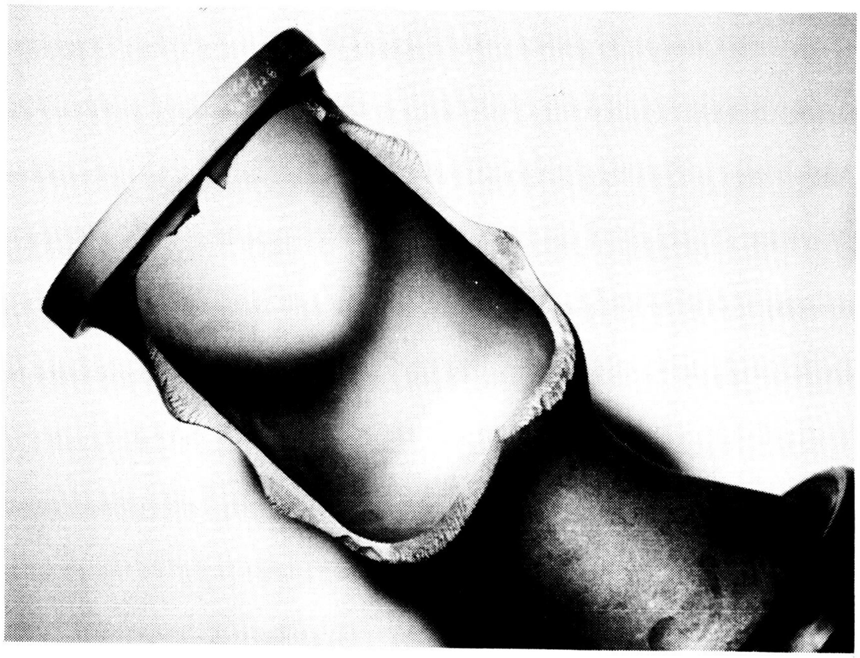

NEG. CT3322-80

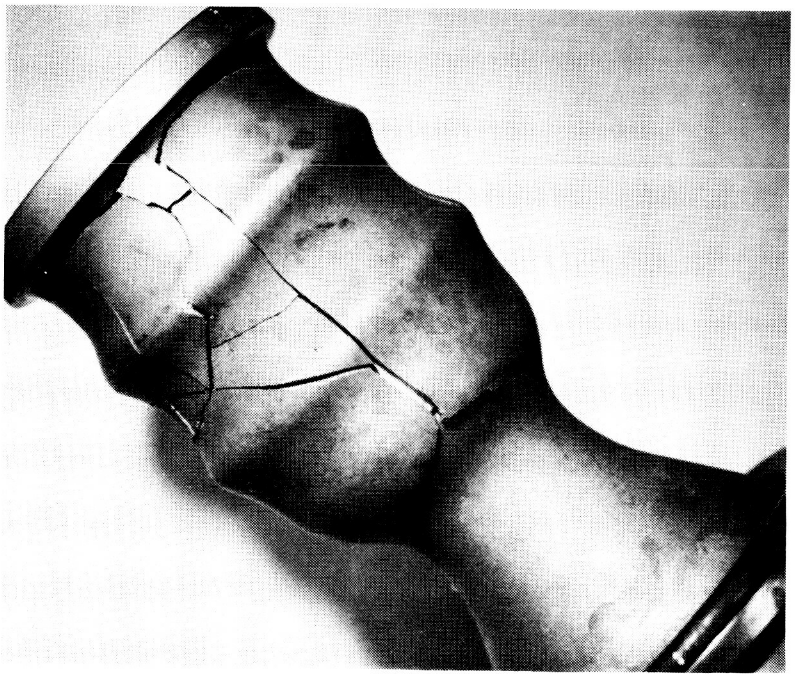

Engine Test Apollo SMRCE Burst Molybdenum/Durak B Chamber

FIGURE 34

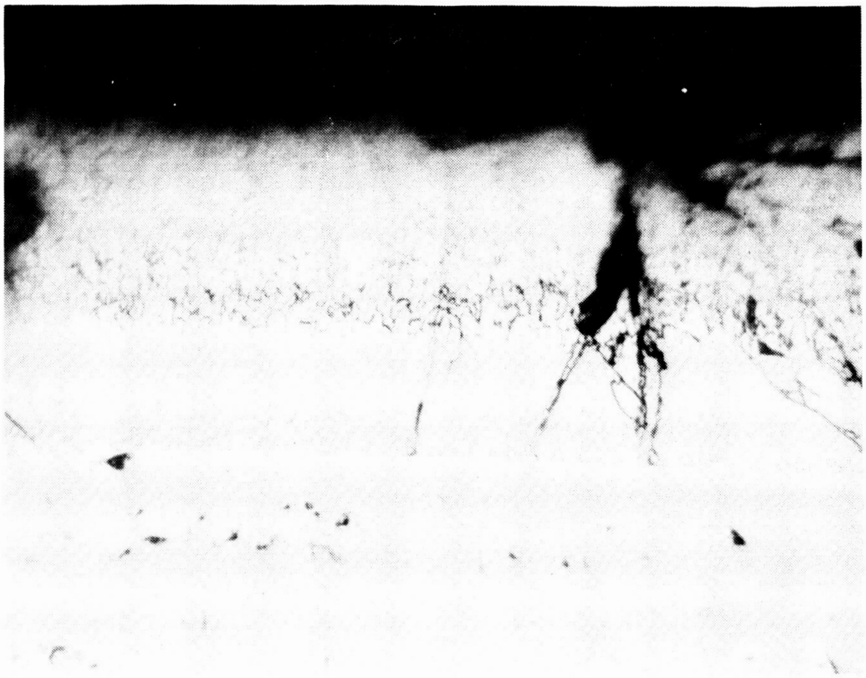

90Ta-10W/R512 Chamber After Testing - 500X

FIGURE 35

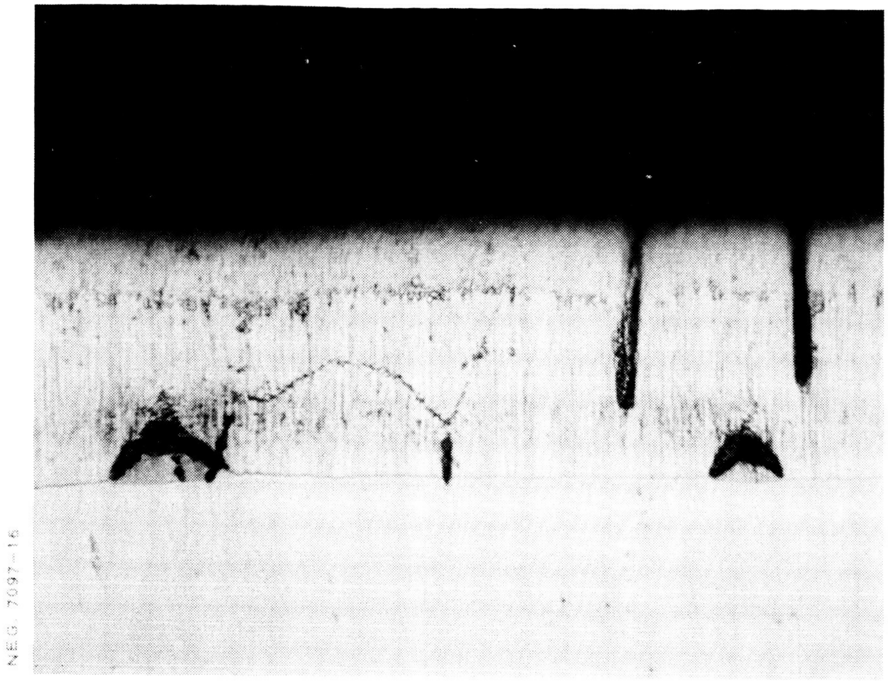

(a) Control Disc

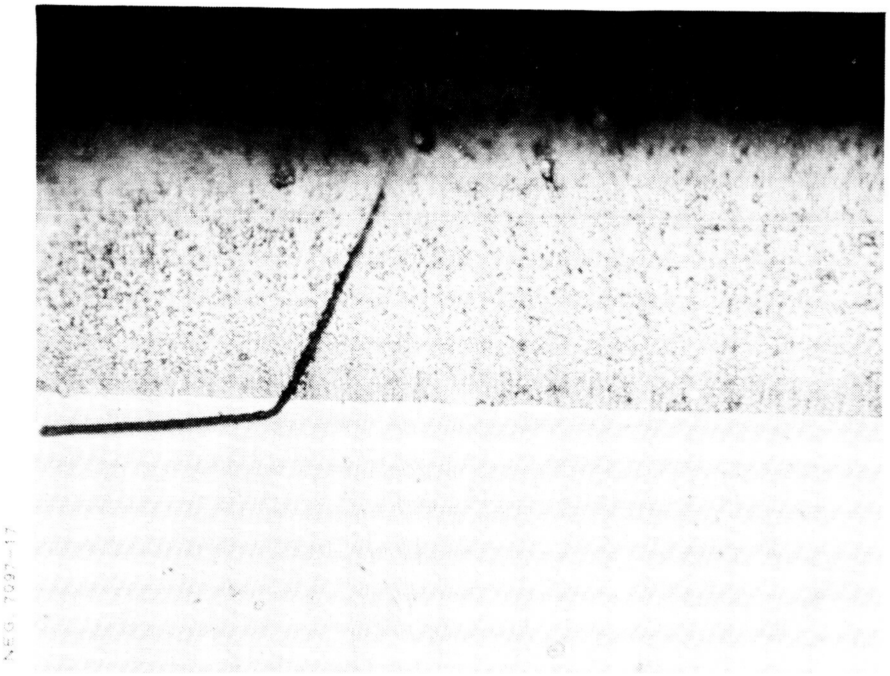

(b) Chamber Specimen After Testing

C-103/Durak KA Chamber and Control Disc - 500 X

FIGURE 36

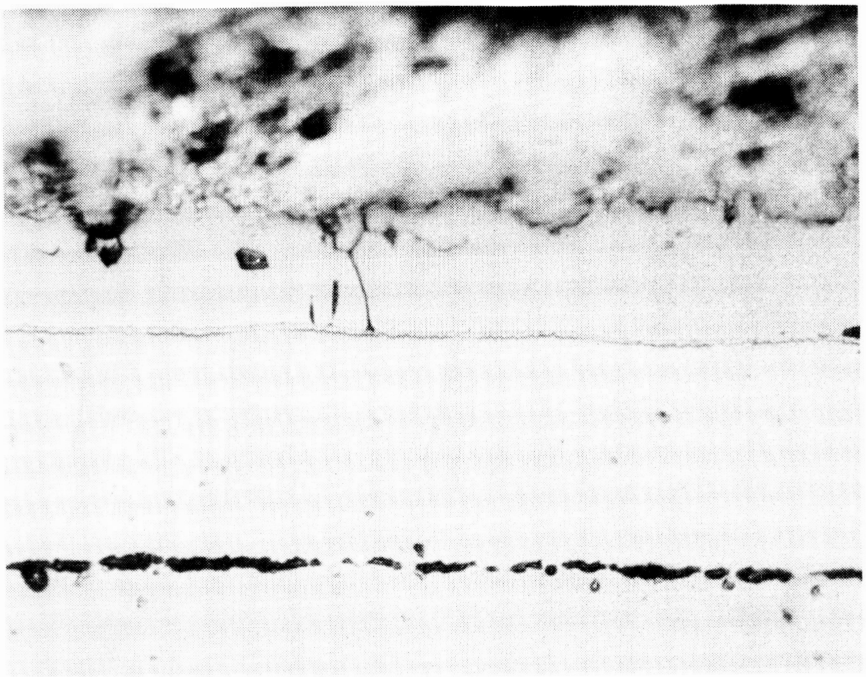

(a) Control Disc

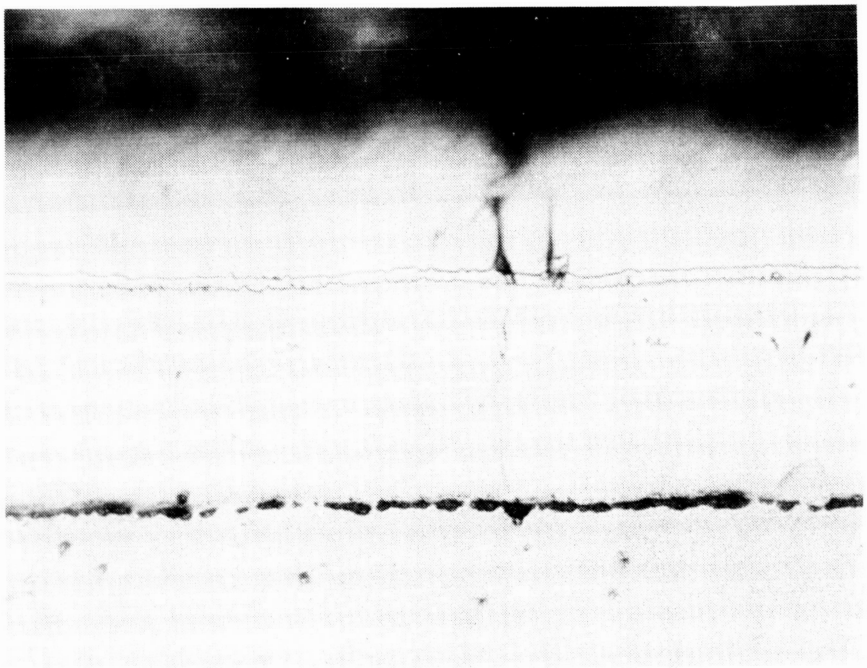

(b) Chamber Specimen after Testing

C-103/W + R508C Chamber and Control Disc - 500X

FIGURE 37

APPENDIX I

HIGH STRAIN RATE PROGRAM

PHASE III - HIGH STRAIN RATE CHAMBER EXPERIMENTS

TEST PLAN

1.0 OBJECTIVE

Comparative evaluation and determined behavior of various coated refractory alloys of Apollo SMRCE combustion chamber configuration exposed to high pressure rise rates similar to engine ignition pressure spike.

2.0 TEST METHOD

The test will be accomplished by dropping a mass against a piston in a fluid filled chamber to generate a pressure spike equivalent to those experienced in the engine. The chamber pressure level will be increased incrementally until the chamber fails. Two methods of measuring devices will be used: a) Kistler transducer to record pressure in the chamber and b) strain gages on the chamber to read strain of the material. The second chamber will be exposed to identical conditions for consistency.

3.0 SYSTEM ANALYSIS

The system was analyzed to determine the magnitude and time characteristics of the pressure pulse. The energy possessed by the falling weight at point of impact with the cylinder is equal to the work done compressing the water:

$$E_{weight} = E_{comp}$$

$$E_{weight} = LW$$

where

L = distance which the weight falls before hitting the piston, and
W = the magnitude of the weight

$$E_{comp} = \int ksds = \frac{ks^2}{2}$$

where

k = spring constant of fluid

s = distance the piston moves to compress the fluid

k can be defined from the geometry of the system and the bulk modulus of the fluid (k^1)

$$k = \frac{k' A_x^2}{V}$$

where

A_x = cylinder cross section area and

V = the system volume

S = the force exerted on the piston by the weight divided by the k,

$$S = \frac{F}{K} \text{ and } F = PA_x$$

These substitutions then give

$$E_{comp} = \frac{P^2 V}{2k}$$

Equating the two energies and solving for L gives:

$$L = \frac{P^2 V}{2k\, W}$$

The motion of the system after the weight contacts the piston is described by the relationship for simple harmonic motion of a spring-mass system. The time to reach peak pressure being 1/4 cycle.

$$t = \frac{\pi/2}{\eta}$$

where η is the natural frequency of the system

$$\eta = \sqrt{\frac{k}{M}}$$

$$t = \frac{\pi}{2}\sqrt{\frac{M}{k}}$$

$$= \frac{\pi}{2}\sqrt{\frac{W}{kg}}$$

The effective weight of this system is the weight of the falling mass plus the weight of the piston or

$$W_{tot} = W + W_p$$

Substituting the above weight and the relationship for k given above gives:

$$t = \frac{\pi}{2A_x}\sqrt{\frac{V(W + W_p)}{gk'}}$$

The system has shown that it can reproduce pressure peaks with approximately the same characteristics as an Apollo engine spike. The performance can be calculated within a good degree of accuracy.

4.0 HARDWARE

4.1 A total of 9 chambers equipped with four strain gages per chamber will be tested:

3 - Molybdenum with Durak B
2 - 90 Ta-10W with R512
2 - C-103 with Durak KA
2 - C-103 with W + R508C

4.2 Apollo attach hardware will be used to duplicate loads on the chamber flange induced by pressure in the chamber.

4.3 Kistler transducer will be installed at the throat to record chamber pressure.

4.4 Test hardware and setup as shown on Figure 1.

5.0 CHAMBER CALIBRATION

5.1 Each chamber shall be pressurized and strain gage calibrated at: 500, 1,000, 1,500, and 2,000 psi prior to testing. Use identical pressure fixture as Apollo.

5.2 The above pressure check shall be cycled one or more times to ascertain repeatability of strain as a function of pressure.

5.3 Four strain gages shall be oriented to read:

a. Circumferential strain (2)
b. Axial strain (2)

6.0 INSTRUMENTATION

Quantity	Description	Model	Range
1	SR-4 Strain Indicator	M	0-±22000 ME
1	SR-4 Switching Unit	220	---
1	Heise Pressure Gage	---	0-3000 psi
1	Kistler Transducer	601H	0-15000 psi
3	Oscilloscope Dual beam with camera	502	---
1	Kistler Charge Amplifier	568	---
1	Kistler Charge Calibration	563	---
1	Transductron	110M	---

7.0 TEST PROCEDURE

7.1 A stainless steel chamber of Apollo SMRCE configuration with strain gages shall be used to duplicate pressure rise rate as experienced on previous Apollo engine spike testing. These rise rates (strain gage and pressure) are shown in Figures 2 and 3.

7.2 Test will be performed at various Kistler chamber pressure levels starting at 1,500 psi and increase incrementally to 10,000 psi. The strain of the chamber shall be measured simultaneously with strain gagees. These results will be correlated with actual engine test data.

When this relationship is duplicated, coated test chamber will be placed in the test rig and test procedure repeated until the chamber fails. Test will be repeated with the second specimen for consistency.

SPIKE TEST RIG SET UP

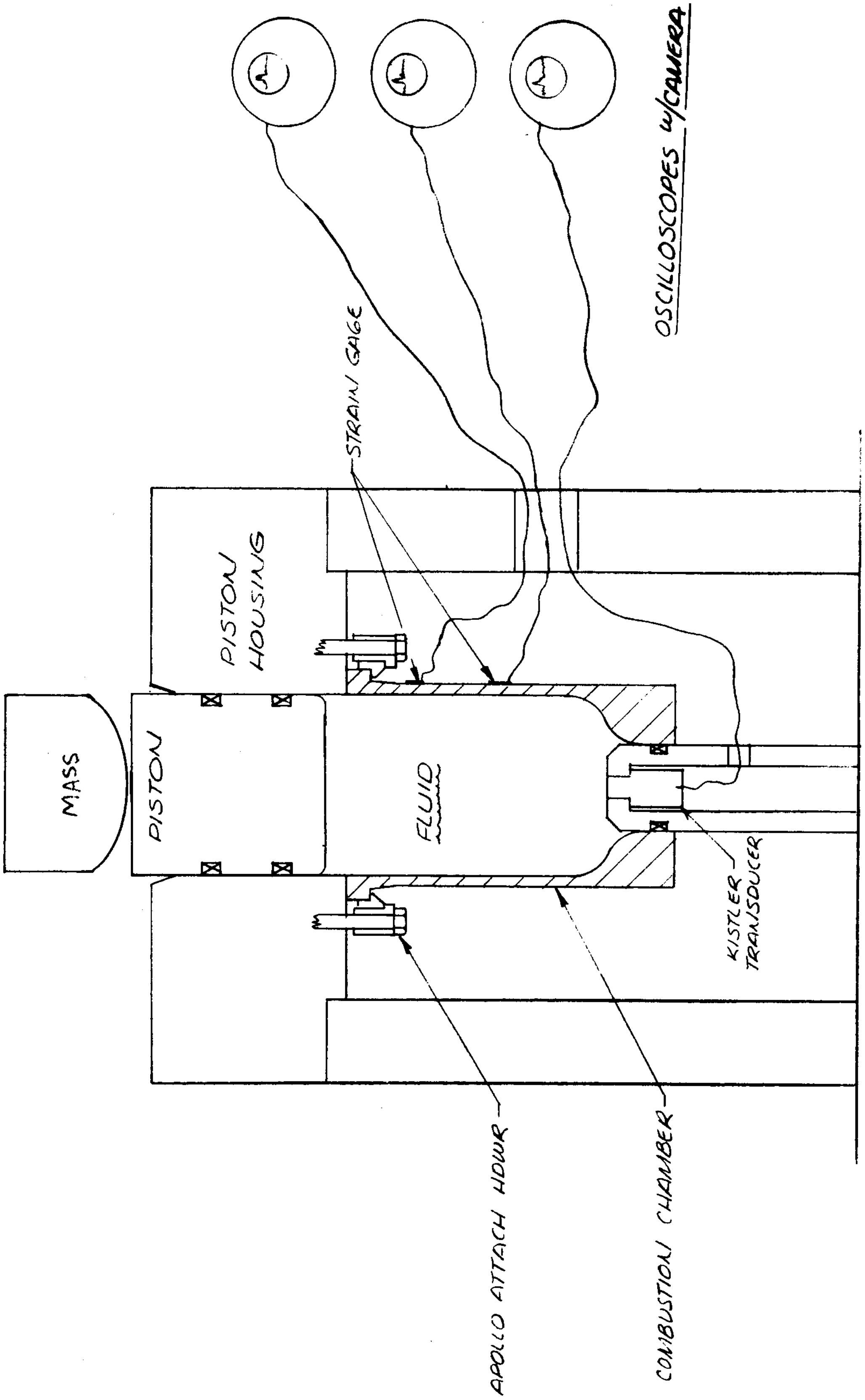

FIGURE 1

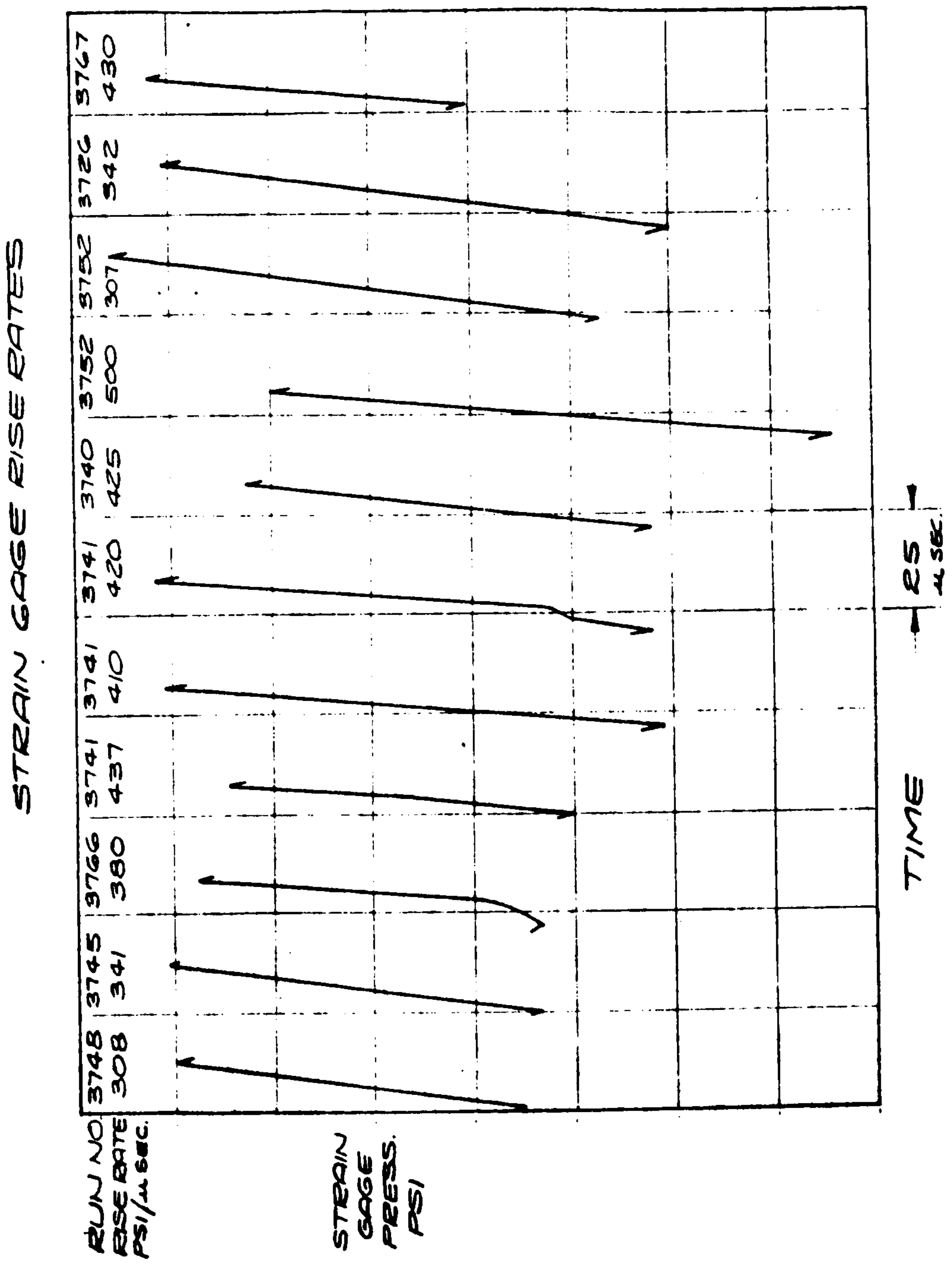
STRAIN GAGE RISE RATES
RUN NO
RISE RATE
PSI/μ SEC.
3748
308
3745
341
3766
380
3741
437
3741
410
3741
420
3740
425
3752
500
3752
307
3726
342
3767
430
STRAIN
GAGE
PRESS.
PSI
TIME
25
μ SEC.

FIGURE 2

KISTLER PRESSURE RISE RATES

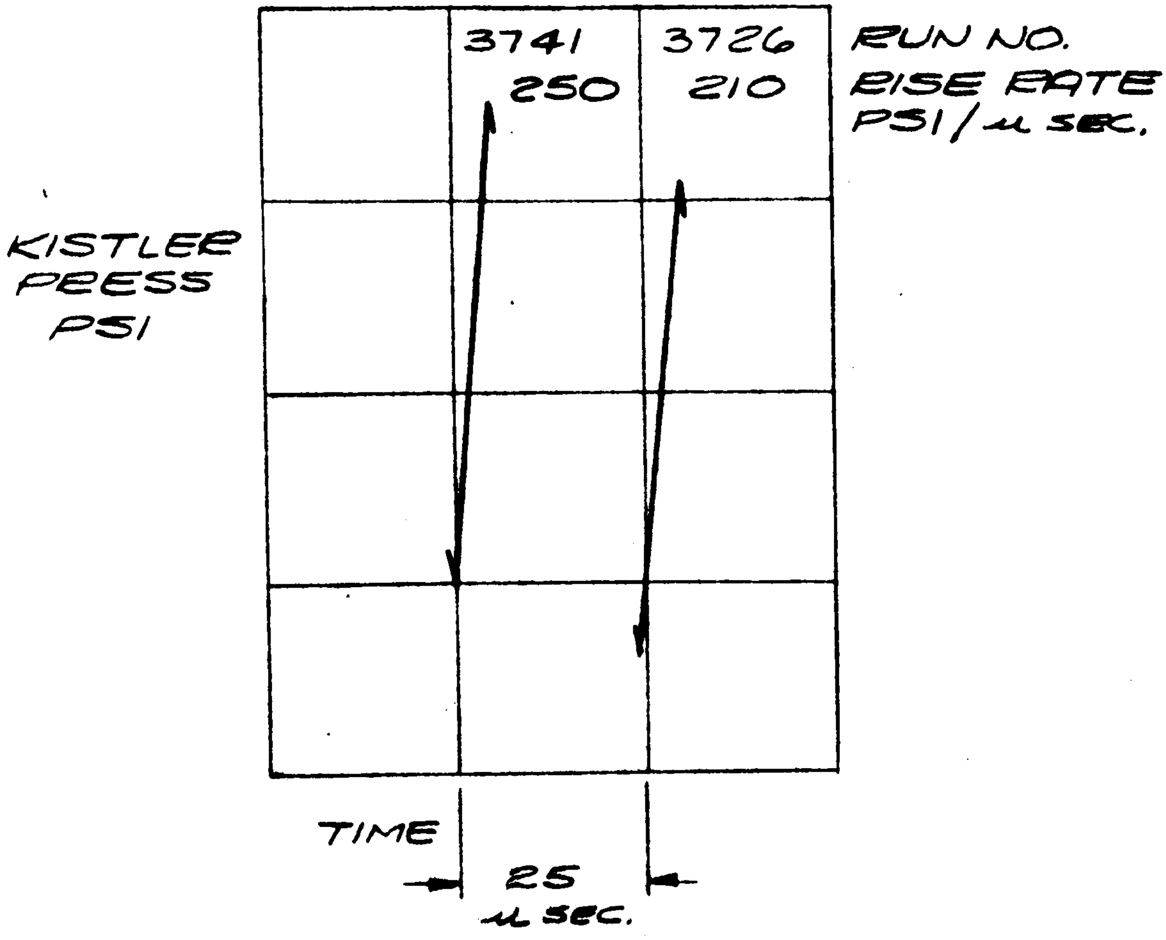

FIGURE 3

APPENDIX II

ANALYSES PERTAINING TO THE TESTING OF ROCKET THRUST CHAMBERS BY WATER HAMMER WAVES

I. INTRODUCTION

In the program which supported the analyses reported herein, an attempt was made to devise an experimental procedure which would indicate the relative merit of various materials for withstanding internal explosions. The alternatives open include actual bi-propellant testing and the use of small explosive charges as two possible means of actually generating an explosion within a test sample. These were rejected because of the lack of control which they introduce into the experiment. An alternative procedure was devised in which water hammer waves are generated with a rise time, pressure, amplitude, and duration similar to those measured during actual chamber testing. The water hammer waves are produced by striking a piston which is free to slide in a water filled test chamber. The resulting pressure is directly related to the velocity of the hammer and this, in turn, can be carefully controlled so as to obtain reproducible test results.

The use of the water hammer technique raises a number of questions concerning the validity of the experiment. Three questions which seem to be of particular importance are the following: (1) what is the nature of the load which is placed on the chamber by the test procedure? In this respect, we wish to define the pressure time history of the load as a function of position within the chamber and the parameters of the experiment. (2) if a chamber does not fail in this test, is it reasonable to presume that it would not fail in actual operation; and conversely, if the chamber does fail, does this mean that it would fail in actual operation? (3) what measurements are significant to the test and how do these measurements relate to the previous two questions? This report presents the results of some analyses of the three questions noted above.

II. THE CHAMBER LOAD

Figure 1 shows a schematic representation of the test setup. The chamber to be tested is mounted in a test fixture with a piston inserted into the upper end of the chamber. The chamber is filled with liquid and the lower end of the chamber is sealed by a plug which contains a pressure transducer in the center of its face. A hammer which strikes the piston is the source of the energy used to generate the pressure raise in the test.

At the moment of impact between the hammer and the piston a system of stress waves is set up which propagate through both the hammer and piston. These compressional waves slow down the hammer and accelerate the piston. When the stress waves reach a boundary, they are reflected and partially transmitted depending on the nature of the interface. The stress waves which propagate through the hammer are reflected as expansion waves further slowing down the hammer until, after one or more of these reflections depending on the geometry of the problem, the hammer separates from the piston.

The pressure wave which reaches the lower end of the piston is reflected as an expansion wave back into the piston, further accelerating that body, and at the same time transmitted as a compression wave into the fluid contained within the chamber. This pressure wave is a water hammer wave whose properties are dependent both on the nature of the fluid and on the nature of the surrounding wall. The water hammer wave pressurizes the chamber, creating a hoop stress and bending stresses within the walls. As this water hammer wave propagates down the chamber, reflected waves continue to move back and forth through the piston, reducing its velocity and gradually changing the nature of the transmitted wave.

When the water hammer wave reaches the far end of the chamber, it is reflected into the fluid in the opposite direction back towards the piston. In general the reflected wave will have an amplitude which is greater than the incident wave. It is this reflected wave which is first measured by the pressure transducer at the far end of the chamber. The reflected wave eventually comes back to the piston where it is again partially transmitted and partially reflected. This process continues indefinitely with wave reflections and transmissions at each end of the chamber and through the piston. There is a general decay in amplitude which eventually predominates over the various wave processes so that after some period of time the magnitude of the waves is so small that the pressure has essentially fallen to zero.

The analysis of this somewhat complex process begins with an examination of the general nature of stress waves both in the piston and hammer and also the associated water hammer wave in the liquid. An introductory discussion on the general nature of the stress waves is presented in Addendum A of this report. Here some illustrations of water hammer waves are given, together with some typical inter-relationships associated with various types of simple reflection and transmission.

A more elaborate analysis of the problem is presented in Addendum B. Here the equations are first examined in Lagrangian coordinates to establish that the approach adopted in Addendum A for examining stress waves in a stationary system is immediately adaptable to the stress analysis of a moving system such as the one under study here. Next, the concept of a wave diagram is introduced by means of some simple examples for impact of bars of various lengths. Then the system under study is examined initially ignoring the question of reflection from the far end of the chamber. Finally in Addendum B, a solution obtained for a system similar to the one under study here in which the fluid is terminated by a metal wall. The corresponding pressure time diagrams have been evaluated for this case for typical combination of system parameters.

A third Addendum has been included in this report. Addendum C presents the results of an investigation of the effect of the chamber termination on the nature of the reflected wave. In Addendum B the termination was assumed to be either non-existent, in the case of the infinitely long fluid column, or an elastic surface of infinite extent. Addendum C examines the effect on the reflected wave of a termination wherein the pressure waves introduce longitudinal stress into the chamber walls thereby accelerating the chamber mass in an axial direction.

One of the interesting wave diagrams discussed in Addendum B is shown in Figure 2. The coordinate axis here is positioned on the horizontal scale and time on the vertical scale. The origin is taken as the interface between the hammer and the piston. In the particular example chosen, both the hammer and piston are presumed to be of equal length L with the liquid extending indefinitely to the right of the piston. Ths piston is characterized by an acoustic impedance

$$Z = \rho C$$

where Z is the acoustic impedance of the piston, ρ is the density of the piston and C is the velocity of sound in the piston material. The hammer is presumed to have the same sonic velocity as the piston, but a different density and hence a different acoustic impedance. Its impedance is given by

$$Z_H = \mu Z$$

The liquid is characterized by an acoustic impedance which differs from that of a piston and, in addition admission, a differing sonic velocity,

$$Z_L = \alpha Z$$

On the diagram are indicated a number of stress waves. These represent displacement of the material from its nominal position. The stress waves are propagated so rapidly compared to the linear velocity of the elements that no attempt has been made here to show how the components actually move with respect to time. Prior to time t = 0 the hammer has been moving toward the piston with velocity V_o. At t = 0, they impact at the origin of the coordinates system. Two stress waves labeled a_o and b_o are generated by this impact. a_o is reflected from the free end of the hammer as c_o which then propagates to the right toward the piston. b_o is partially transmitted into the liquid as e_o and partially reflected back toward the hammer, piston interface as d_o. The location of the stress waves as a function of time can easily be determined by examination of the figure.

When stress wave d_o reaches the hammer-piston interface, it is again reflected as the right running stress wave b_1. At the piston liquid interface, b_1 again gives rise to a transmitted wave e_1 and a second reflection from that surface d_1. These multiple reflections within the piston continue indefinitely.

At the time when stress waves c_o and d_o meet at the origin, the piston separates from the hammer. At this time the hammer velocity has been reduced from its initial value while the velocity of the piston has been increased. After the two waves meet, the piston is moving faster than the hammer by V_o, the initial hammer velocity.

a_o and b_o are both compression waves, while c_o and d_o are both expansion waves (this assumes, of course, that the liquid has a lower acoustic impedance than the piston). After the piston separates from the hammer, b_1, b_2, and b_3 are all expansion waves, while d_1, d_2, d_3, etc., are all compression waves. The waves in the liquid are of the same character as the incident wave from the piston. e_o is a compression wave, while all of the subsequent waves, e_1, e_2, etc., are expansion waves.

One can write a closed form expression for the pressure level in the liquid following each wave. If P_n is the pressure in the liquid following the passage of the water hammer wave e_n, then P_n is given by

$$P_n = 2 \alpha Z V_o \left(\frac{\mu}{1 + \mu}\right) \left(\frac{1 - \alpha}{1 + \alpha}\right)^n$$

The subsequent variation of pressure in the liquid as a function of time is then given by a graph of the type shown in Figure 3. Some numerical values based on a steel piston, water and mercury for the liquids and a hammer whose acoustic impedance is five times that of the piston are presented in Table 1.

Treating the hammer as a mass of the same length as the piston but with a higher acoustic impedance is a mathematical convenience which permits one to avoid a detailed examination of the stress propagation through the striker plate, the interior of the hammer, and the exterior structure of the piston. The actual stress propagation through these components is very complex. In the event that the hammer and piston are actually of the same material but have different length, some of the energy subsequent to impact is trapped as stress waves in the longer of the two components. Under these circumstances the ordinary laws of rigid body impact and rebound are not obeyed. This might be of significance in an experiment in which the design of the impactor had not been well thought out, but it does not apply to the present case. The components actually used in the Marquardt test do behave in very much the same manner that one would expect of bodies which obey rigid body dynamics. All of these difficulties are eliminated by the artifice of assuming a higher density for the hammer relative to the piston while not changing its sonic velocity or length.

As noted previously, the water hammer waves which are sent out from the piston are reflected from the far end of the chamber. This reflection produces a pressure rise in the fluid which increases the hoop stress in the cylinder walls and also creates axial tension in the cylinder. It is this increased pressure which is measured by the pressure pickup. Although the precise amount of the increase depends on the character of the termination, it is a close approximation to state that the pressure approximately doubles on reflection. An elastic wall give somewhat lower numbers, while a wall which acts as a mass and spring gives higher pressure when the end of the chamber rebounds after its initial displacement. Figure 4 shows the variations in pressure-time history for various terminations.

For an elastic wall with a pressure wave of amplitude P_o incident upon it, the reflected wave will have amplitude P given by

$$P_E = \frac{2\ P_o}{1 + \zeta}$$

where ζ is the ratio of the acoustic impedance of the fluid to that of the wall material. For a steel wall and mercury as the fluid

$$P_{E,H_2} = 1.63\ P_o$$

For water and steel,

$$P_{E,H_2O} = 1.94\ P_o$$

For a chamber termination which distends under the applied pressure, the pressure oscillates with time about $2P_o$. The oscillations die away exponentially. They have a maximum amplitude of

$$P_{max} = 2 P_o \left[1 + \frac{2\lambda}{\omega_n} e^{-\frac{\lambda}{\omega'} \tan^{-1} \left(\frac{\omega'}{\lambda}\right)}\right]$$

Where:

$$\lambda = \frac{\pi D^2 Z}{8 m}$$

$$\omega_n^2 = \frac{\pi D^2 hE}{\ell m}$$

$$\omega' = \sqrt{\omega_n^2 - \lambda^2}$$

D = diameter

Z = impedance

m = apparent mass of chamber

h = wall thickness

E = modulus of wall material

ℓ = chamber length

For an assumed mass of 0.3 lb, steel and mercury give

$$P_{max} = 2.02 P_o$$

For water and steel

$$P_{Max} = 2.25\ P_o$$

For a gas filled chamber

$$P_{Max} = 2.0\ P_o$$

As the assumed mass drops towards zero, the maximum pressure falls to

$$P_{Max} = 2\ P_o$$

As noted previously, the reflected pressures travel to the piston face where they modify its motion and are again reflected. Figures 5 and 6 show the results of these interactions for two different combinations of materials assuming an elastic reflection at the chamber end. It may be seen that for some combinations of materials and geometry the first peak will be the highest one with the pressure subsequently falling. For other combinations, especially with heavier pistons and lower fluid impedance, the maximum will occur on one of the subsequent peaks.

Experimental data has been obtained in the Marquardt test apparatus with mercury and water as the fluids. In the case of mercury the maximum pressure is reached on the first or second peak followed by rapid decay. For water, the maximum pressure is not reached until several successive reflections have occurred after which the peaks again reduce in height. While this differs quantitatively from the diagrams shown in Figures 5 and 6, the qualitative agreement is excellent.

III. CHAMBER FAILURE

The failure mechanism for those chambers which have failed because of internal explosions is not known. Examination of fractured chamber components suggests that failure in hoop tension may have been responsible, but this is only conjecture. One of the questions which comes up in this regard is whether the pressure as measured by pressure transducer is a significant parameter in the experiment. Stresses are generated in the chamber walls by virtue of the water hammer waves. As the water hammer wave moves down the chamber, it generates hoop tension behind it by virtue of the internal pressure. It also generates bending stresses at the leading edge of the wave. These are a consequence of the pressure discontinuity across the wave. When the water hammer wave reaches the closed end of the chamber, it distends this end axially, thereby creating axial tension in the chamber walls. Thus, the total state of stress within the chamber is a complex function of time and position. The axial stresses arise from the bending moments in the wall and the distention of the chamber, while hoop stresses arise from the internal pressure and also as a consequence of the bending moments.

A preliminary examination of the combined load in the chamber walls is presented in Appendix D. It is shown there that the bending stress caused by the discontinuity in the pressure wave is given by

$$\sigma_B = \frac{3P}{2\beta^2} e^{-\beta x} \text{Sin } \beta x$$

where:

$$\beta^4 = \frac{12(1-\upsilon^2)}{D^2 h^2}$$

υ = Poisson's Ratio

x = Distance behind wave front

P = Pressure behind wave front

Assuming 0.3 for Poisson's ratio, this quantity has a maximum at $\beta x = \frac{\pi}{4}$ of

$$\sigma_{B_{Max}} = 0.29 \frac{P\,D}{2\,h}$$

which is approximately 60% of the nominal axial stress in a pressure vessel.

The direct axial stress produced by the load at the end of the cylinder has a maximum value which is given by

$$\sigma_{Max} = \frac{P_o D}{2\,h} [1 + e^{-\frac{\pi}{2}\frac{\lambda}{\omega'}}]$$

The maximum value of this quantity is given by

$$\sigma_{Max} = 1.01 \frac{P_o D}{2h} \text{ for mercury in steel}$$

$$= 1.71 \frac{P_o D}{2h} \text{ for water in steel}$$

$$= 2.00 \frac{P_o D}{2h} \text{ for any gas filled chamber}$$

Expressed in terms of the maximum pressure in the reflected water hammer wave, these become

$$\sigma_{Max} = 0.500 \frac{P_{Max} D}{2h} \text{ for mercury}$$

$$= 0.760 \frac{P_{Max} D}{2h} \text{ for water}$$

$$= 1.00 \frac{P_{Max} D}{2h} \text{ for a gas}$$

Reflection of the direct stress tension wave from the flange at the top of the chamber will approximately double this value. The maximum stress will occur where this reflected tension wave meets the reflected water hammer wave in the fluid. Combining these stresses, the total axial stress is seen to be

$$\sigma_{A_{II}} = 1.29 \frac{P\,D}{2h} \quad \text{for mercury}$$

$$= 2.10 \frac{P\,D}{2h} \quad \text{for water}$$

$$= 2.29 \frac{P\,D}{2h} \quad \text{for a gas}$$

which is in each case higher than the nominal hoop stress in a simple pressure vessel. Since the tension wave and the water hammer wave travel at different speeds, they do not always add directly.

Before the tension wave overtakes it, the axial stress is

$$\sigma_{A_o} = 0.29 \frac{P\,D}{2h} \quad \text{for mercury, water, or gas.}$$

After the tension wave passes the first time, the axial stress increases to

$$\sigma_{A_I} = 0.79 \frac{P\,D}{2h} \quad \text{for mercury}$$

$$= 1.05 \frac{P\,D}{2h} \quad \text{for water}$$

$$= 1.29 \frac{P\,D}{2h} \quad \text{for a gas.}$$

The reflection of the wave from the flange then leads to the maximum value.

The bending stress caused by the discontinuity in pressure across the reflected water hammer wave also increases the hoop stresses behind the wave. The maximum hoop stress away from the ends of the chamber is achieved at the location of the maximum bending moment, and is given by

$$\sigma_H = \frac{P\,D}{2h} + \upsilon\,\sigma_B$$

$$= 1.09\,\frac{P\,D}{2h}$$

The situation at the flange end of the chamber is more complex, because the wall is built in here, the axial tensile stresses give rise to circumferential tensile stresses

$$\sigma_c = \upsilon\,\sigma_A$$

Assuming $\upsilon = 0.3$, the circumferential stress after reflection will be

$$\sigma_c = 0.30\,\frac{P\,D}{2h} \quad \text{for mercury}$$

$$= 0.46\,\frac{P\,D}{2h} \quad \text{for water}$$

$$= 0.60\,\frac{P\,D}{2h} \quad \text{for gas}$$

This circumferential stress will diminish away from the flange. If the water hammer wave should arrive at the flange coincident with one of the reflections of the axial stress wave, the maximum circumferential stress near the flange would approach

$$\sigma_{CM} = 1.39 \frac{P\,D}{2h} \ (Hg)$$

$$= 1.78 \frac{P\,D}{2h} \ (H_2O)$$

$$= 1.69 \frac{P\,D}{2h} \ (gas)$$

These values are of the same order of magnitude as the maximum axial stress values.

The hoopstress is sometimes larger and sometimes smaller than the maximum axial stress. The chamber might fail due to this hoop stress before the axial stress reaches its maximum value. It could also fail from the axial stress, even if it survives the initial hoop loading.

This analysis is, of course, dependent on the variation of the incident pressure wave with time, which is more complex than the simple wave which has been assumed here. The duration of the pressure peak depends on the parameters of the problem. In the case of mercury, for example, the maximum axial stress does not occur until approximately 60 microseconds after the wave reaches the far end. The maximum pressure does not occur until approximately 90 microseconds after the wave arrives. If the amplitude of the incident wave does not remain at its peak level for this time period, the stress and pressure maxima will be reduced. For the present case, with a 2-inch long piston and a 3-inch long chamber, it appears that the pressure has already begun to decay before the maximum is reached with a time constant of 39 microseconds. The peak stresses and pressures may be somewhat less than indicated by this analysis.

IV. INTERPRETATION OF THE TEST RESULTS

Most data analysis for these tests will involve the use of the high speed pressure transducer placed at the chamber exit. It is shown in Addendum D that this instrument might only register 81% of the maximum pressure load felt by the chamber walls when the chamber is filled with mercury. With water and gas the instrument should agree with the pressure. In terms of this pressure reading P_K, the highest stresses in each direction are

Axial	Material	Circumferential
$\sigma_{A_{II}} = 1.60 \frac{P_K D}{2h}$	Hg	$\sigma_{CM} = 1.72 \frac{P_K D}{2h}$
$= 2.10 \frac{P_K D}{2h}$	H_2O	$= 1.78 \frac{P_K D}{2h}$
$= 2.29 \frac{P_K D}{2h}$	gas	$= 1.69 \frac{P_K D}{2h}$

One of the principle questions stated before was "If the chamber survives this test, would it survive a chamber detonation?" We can partially answer that question now. When the chamber is filled with gas and an axial detonation wave propagates through it, the chamber loads are of the same nature as those produced by this water hammer experiment. The principle difference is that the acoustic impedance of the gas is very low resulting in the differing values of $\sigma_{A_{II}}$ and σ_{CM} noted above.

It is clear that these are all comparable in value, although not identical. Variations in wave travel and pressure decay times will cause even larger differences in the maximum stresses. Nevertheless it would seem that the results of these tests have a direct bearing on the selection of materials and the design of chambers.

Another factor which tends to obscure the relationship between the water hammer tests and chamber testing is that more than one kind of detonation wave has been observed in rocket engine firings. Waves are sometimes initiated at the exit to the chamber, sometimes at the head, and sometimes at a side wall. While the waves which initiate at a chamber end tend to propagate in the axial direction as plane disturbances, those which initiate at the side of the chamber propagate across it with a resulting nonsymmetric loading of the chamber walls. The present test program made no attempt to simulate this type of loading.

It appears, therefore, that with regard to the question asked above, that survival of the present test does not insure survival of a chamber detonation which registers a comparable peak pressure. The tests are nevertheless of great value. They provide us with means of comparing chamber wall material and structural design under conditions of shock loading which are controllable and reproducible. These shock loading conditions closely simulate at least one type of rocket chamber explosion.

V. CONCLUSIONS

An analytical investigation has been conducted in relation to the testing of rocket thrust chambers by water hammer waves. In the related experiments water hammer waves were propagated axially through liquid filled test chambers, thereby simulating one mode of chamber detonation. Liquids used for propagation of the waves in the test were water and mercury (principally the latter). The analysis indicates that the test conditions should yield stresses for a given pressure level reading, which are comparable to but not identical with those created by an axially propagating detonation wave. The mode of chamber failure will depend on which stresses are the highest, axial or circumferential. The amplitude of these stresses varies both with position in the chamber and time. A chamber might fail due to hoop stress before the axial stress reaches its maximum value. It could also fail from axial stresses even if it survives the initial circumferential loading. The time of occurrence of these maxima is somewhat different for the test case and the chamber detonation case. The maximum axial stresses are about 40% higher in the detonation, while the maximum circumferential stresses are slightly lower. Because of these discrepancies and, in addition, because of the existence of transverse detonation waves, survival of the present test does not insure survival of a chamber detonation. When a chamber fails in the present test, the mode of failure will not necessarily by the same as that caused by a detonation.

The present tests have considerable value in terms of their ability to subject prospective chamber materials and design to controllable reproducible shock loads comparable to those experienced in chamber operation. The present tests do not appear to completely eliminate the need for subsequent rocket firings to guarantee chamber reliability.

TABLE I

Material	Water	Mercury	Steel
Density (gm/cc)	1.0	13.5	7.9
Sonic velocity in infinite medium (ft/sec)	4900	4750	19,000
Sonic velocity in 2" x 0.11" wall steel chamber (ft/sec)	4480	2550	
Wave travel time	112	196	
Acoustic Impedance (psi/ft/sec)	60.3	463	2,022

Hammer to Piston Mass Ratio	Hammer Drop Height h(ft)	Water Hammer Pressure			
		Po	Pk	Po	PK
0.5	1	320	620	2500	4100
0.5	4	640	1160	4900	8000
1.0	1	480	850	3700	6000
1.0	4	960	1860	7400	12000
5.0	1	800	1560	6200	10000
5.0	4	1600	3100	12400	20000

Arrangement of Test Apparatus

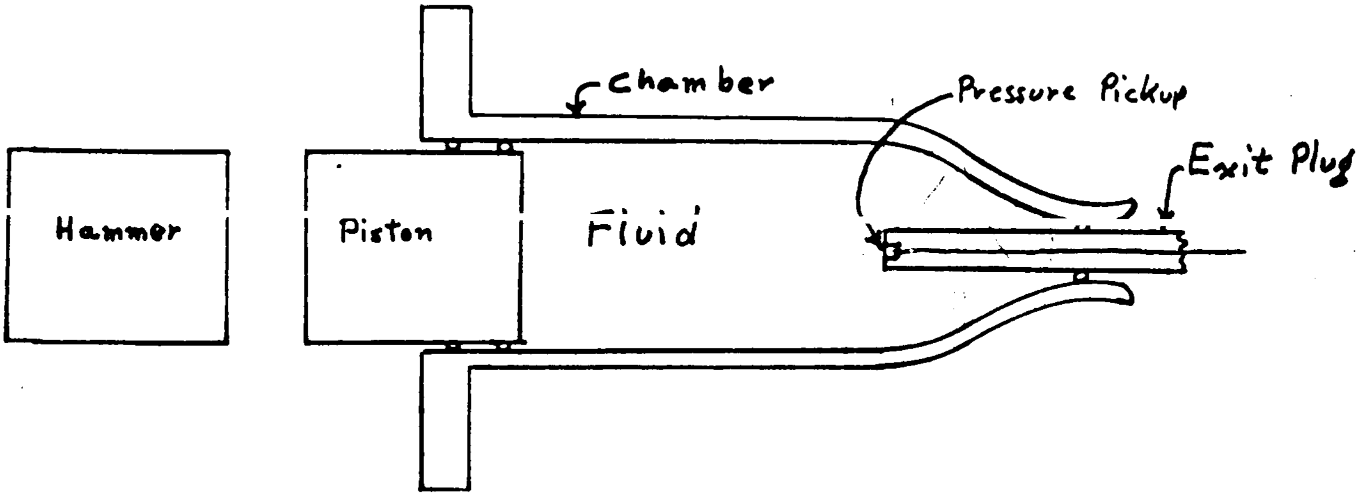

FIGURE 1

Wave Diagram For Initial Impact

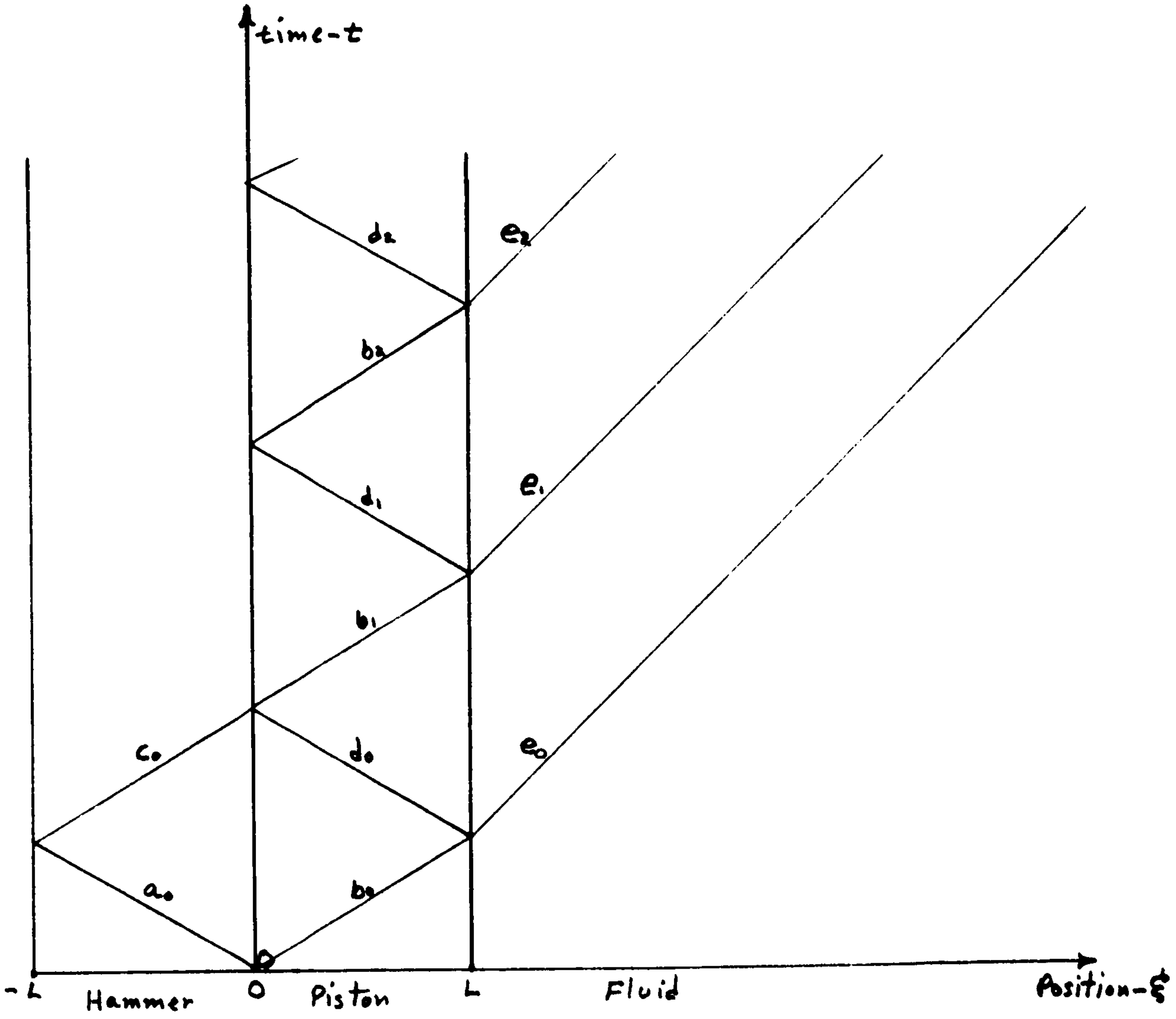

FIGURE 2

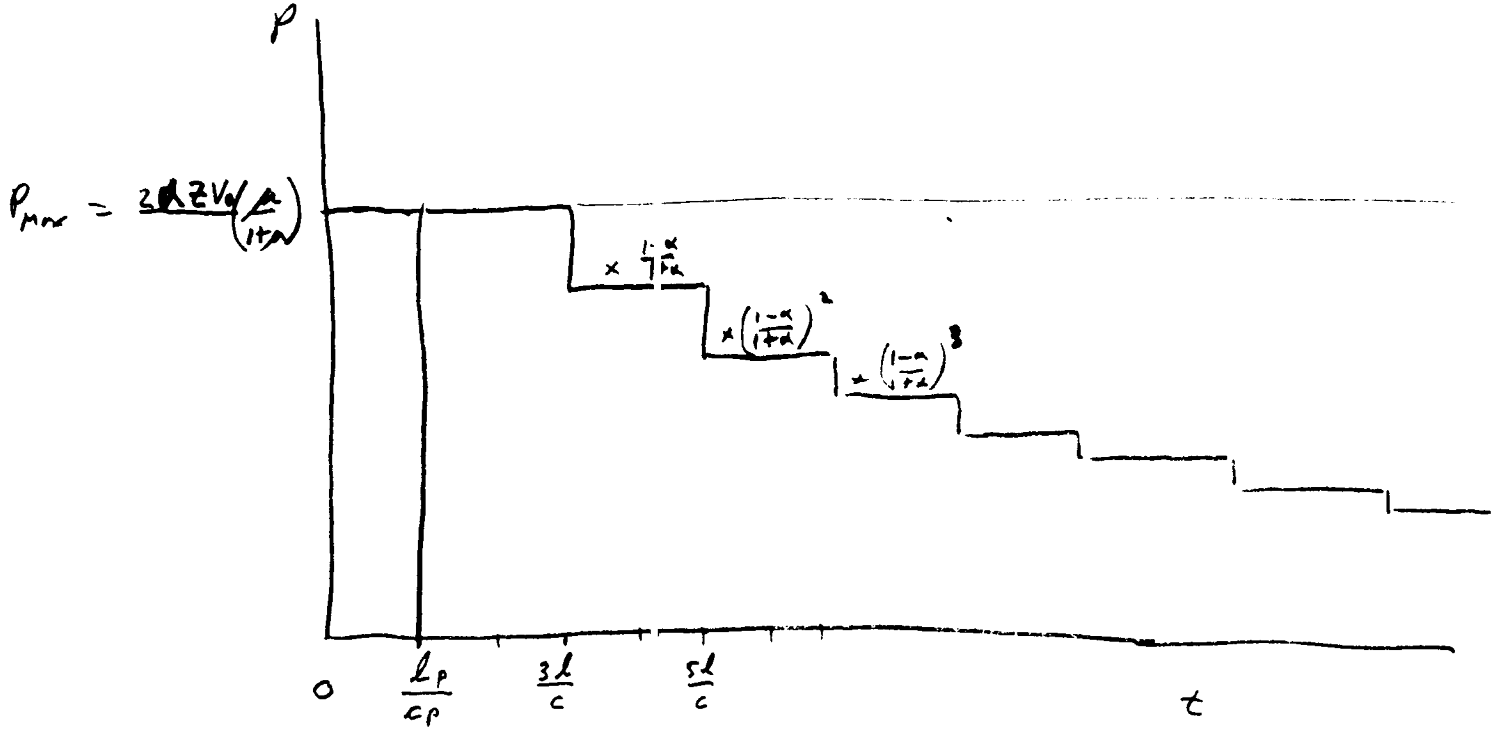

Initial Pressure Variation with Time at Piston Face

FIGURE 3

Chamber End Pressure

Effect of Termination Characteristic

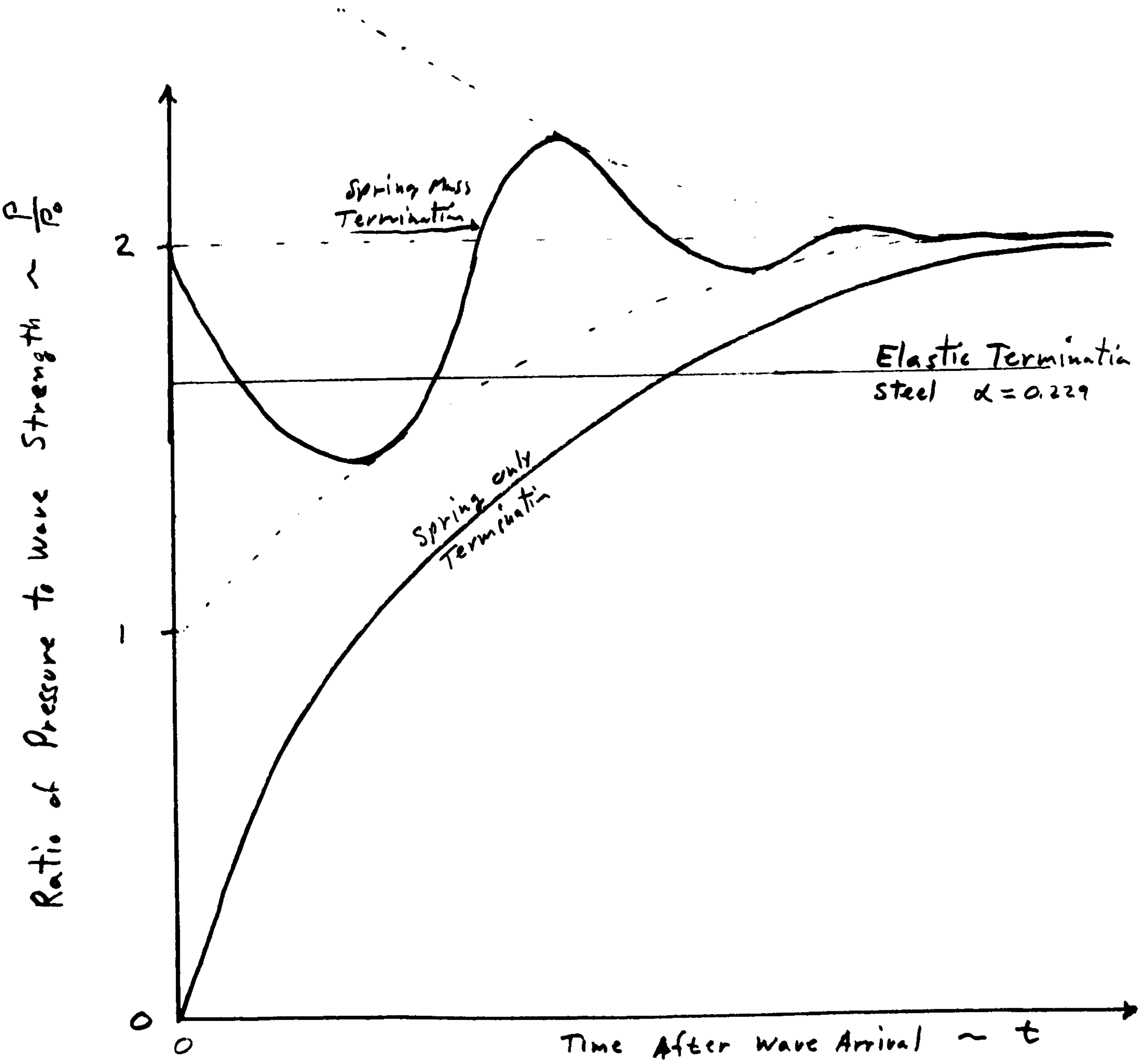

FIGURE 4

Pressure-Time Variation At Piston
Including End Reflection Effects
Low Impedance Liquid

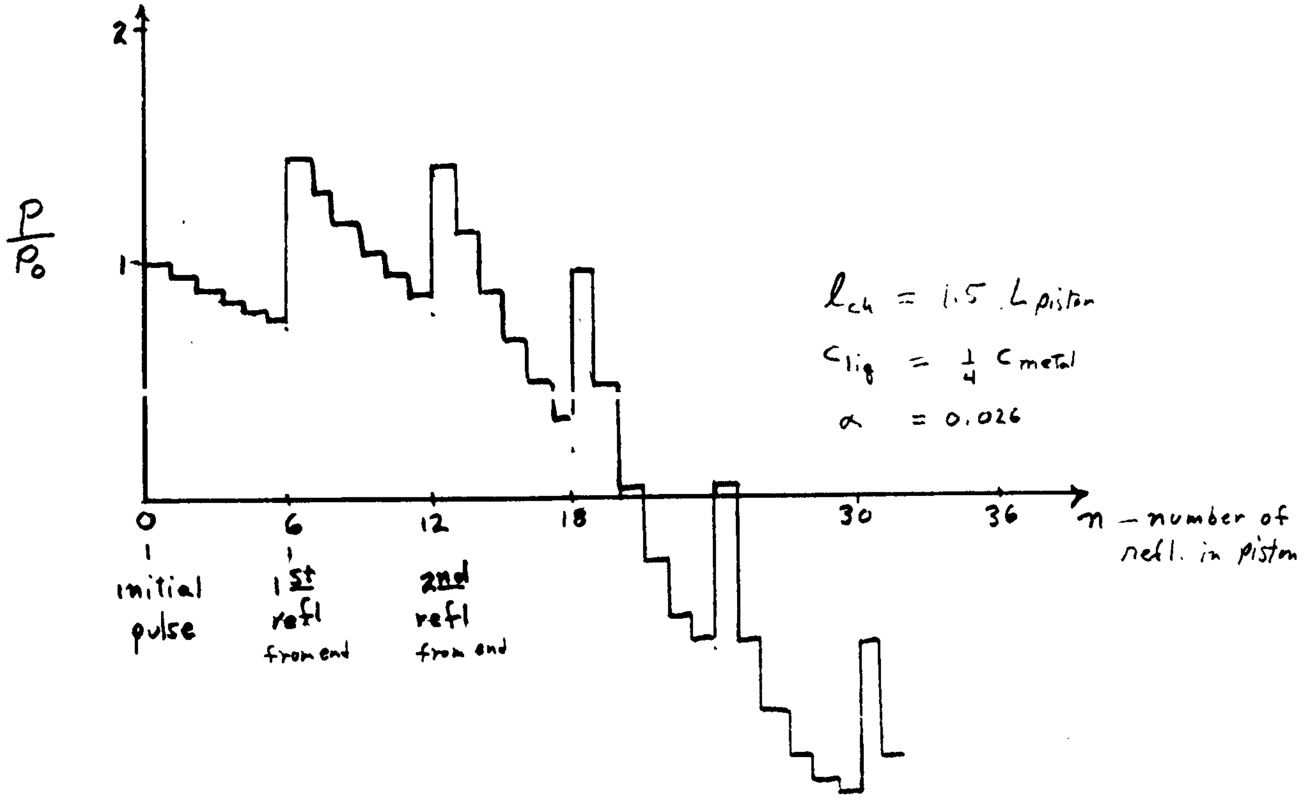

FIGURE 5

Pressure Time Variation At Piston
Including End Reflection Effects
High Impedance Liquid

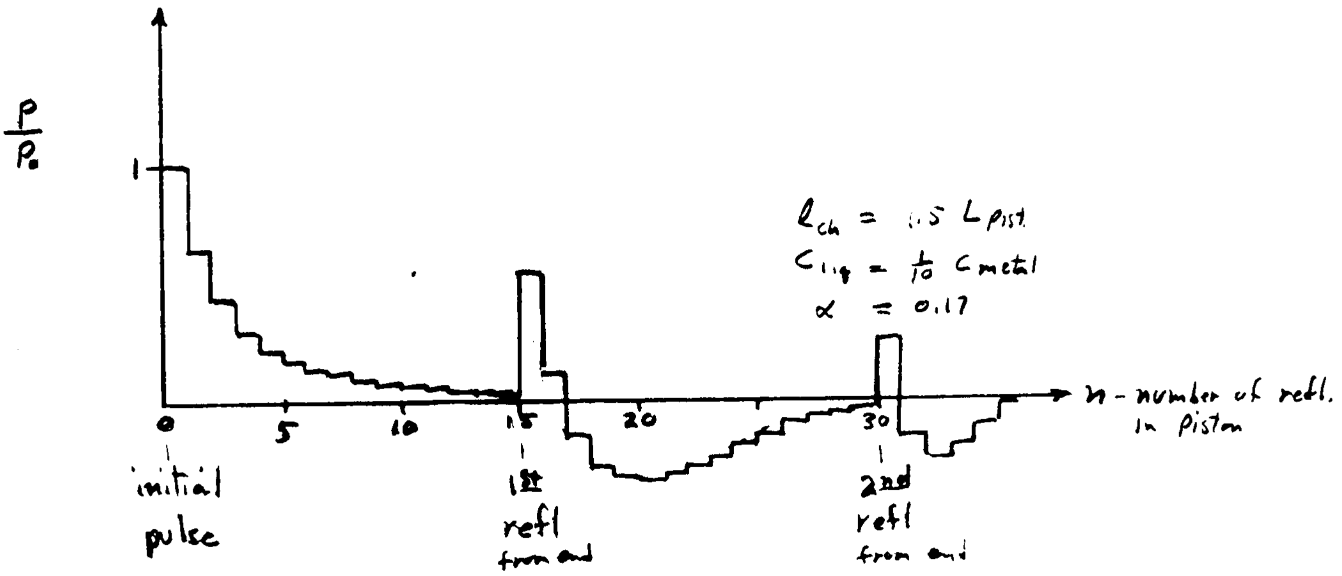

FIGURE 6

ADDENDUM A

STRESS WAVES AND WATER HAMMER WAVES

The elementary analysis of problems in engineering mechanics, such as those discussed in this report, is frequently based on the assumption of "rigid body" properties. It is assumed, in particular, that all points in a body under examination are moving with equal velocity at all times. The state of internal stress is usually ignored. Even when some elastic properties are considered, for example the compressibility of a liquid, it is usually assumed that the entire bulk of the liquid exists in some uniform state of hydrostatic pressure at any instant. While this approach is satisfactory for relatively slow processes, it is not accurate for at least two situations of interest here. First, the stress waves produced by impact are transient in nature. The magnitude of these waves varies both in position and in time throughout the test item. Discontinuities across wave fronts are important sources of stress. Secondly, energy can be stored in strain energy after impact. Rigid body analysis assumes that all energy must be stored as kinetic energy after impact, and hence can yield the wrong momentum exchange analysis. In addition to these factors, the shape of the pressure time and stress time curves can only de determined by an elastic analysis.

1. Velocity of Propagation of Stress Waves

The application to pressure at one end of an elastic column causes a stress wave to propagate through the column away from the point of application. The velocity of propagation of stress waves depends generally on the relationship between the level of the stress and the displacement which it produces. Dilatational waves (tension-compression) travel at one speed while shear waves travel at another. Longitudinal waves in a bar travel at almost the same velocity as dilatational waves in an unbounded medium. Kolsky(1) for example, shows that these may be expressed as:

(1) Stress Waves in Solids: H. Kolsky, Dover 1963

ADDENDUM A (Continued)

Dilatational Waves
$$C_1 = \sqrt{\frac{\lambda + 2\mu}{\rho}}$$
$$= \sqrt{\frac{E}{\rho} \frac{1 - \nu}{1 - \nu - 2\nu^2}}$$

Shear Waves
$$C_2 = \sqrt{\frac{\mu}{\rho}}$$
$$= \sqrt{\frac{E}{\rho} \frac{1}{2(1 + \nu)}}$$

Longitudinal Waves
$$C_o = \sqrt{\frac{E}{\rho}}$$

The propagation of flexural waves is a complex subject which is, fortunately, of little concern to us here.

2. Velocity of Water Hammer Waves

Stress waves are propagated through all elastic media including liquids. Because liquids cannot support shear stresses, the types of waves are restricted to those involving compression and expansion. The velocity of plane water hammer waves in an unbounded medium is given by

$$C_{L_1} = \sqrt{\frac{K}{\rho}}$$

When the liquid is confined with an elastic pipe, the displacement of the pipe walls reduces the velocity of propagation of lontitudinal waves within the liquid. Parmakian(2) gives an expression for the velocity of water-hammer waves in pipes with various types of end restraint.

(2) Water Hammer Analysis: J. Parmakian, Dover 1963

ADDENDUM A (Continued)

$$C_L = \sqrt{\frac{1}{\rho \left(\frac{1}{K} + \frac{Df}{Eh}\right)}}$$

$$= \sqrt{\frac{C_{L_1}}{1 + \frac{Kf}{Eh}}}$$

where

$f_1 = \frac{5}{4} - \nu$ for a pipe anchored at one end without expansion joints

$f_2 = 1 - \nu^2$ for a pipe anchored along its length

$f_3 = 1 - \frac{\nu}{2}$ for a pipe with expansion joints

The value of f is close to 0.9 for any of the cases listed by Parmakian. For $\nu = 0.3$, the values are

$$f_1 = 0.95$$

$$f_2 = 0.91$$

$$f_3 = 0.85$$

3. Stress Wave Relationships

When a stress wave is propagated through an elastic medium there is a change in the stress level and velocity of the material as the wave passes. These are interrelated by

$$\Delta\sigma = \rho \cdot c \Delta v$$

$$= Z \Delta v$$

ADDENDUM A (Continued)

When $\Delta\sigma$ is positive, Δv increases in the direction of the wave which is called a compression wave. When $\Delta\sigma$ is negative the velocity in the direction of propagation is decreased and the wave is called a tension wave or an expansion wave.

The simplest stress waves to envision are those characterized by a step change in stress and velocity. These are used in the discussion below of wave interactions and reflections. In general, however, a stress wave can have any functional form, as long as it has the proper relation between its time and distance coordinates. The general forms of the wave equation are

$$\nu_R (x - ct) = 0$$

for a wave which is moving in the positive x direction, and

$$\nu_L (x + ct) = 0$$

for a wave moving in the negative x direction. "ν" here refers to the displacement of the particles of material relative to the "x" coordinate system. The strain is then given by

$$\epsilon = \frac{\partial \nu}{\partial x} = \nu'$$

The stress is then (using positive stress to denote compression)

$$\sigma = - E \frac{\partial \nu}{\partial x} = - E\nu'$$

The velocity is

$$v = \frac{\partial \nu}{\partial t} = - c\nu'$$

So that

$$\sigma = \frac{E}{C} v$$

$$= \rho c v$$

ADDENDUM A (Continued)

4. Transmission and Reflection of Stress Waves

When a stress wave is propagating in a medium of impedance Z and it reaches an interface where the impedance changes αZ, the wave will be partially transmitted into the medium and partially reflected back into the old medium. Let V_i and σi be the initial states of stress in both media before the wave passes. Let the amplitude of the wave be given by its velocity increase, ΔV. The increase in stress behind the incident wave will be $\Delta\sigma = Z\ \Delta V$.

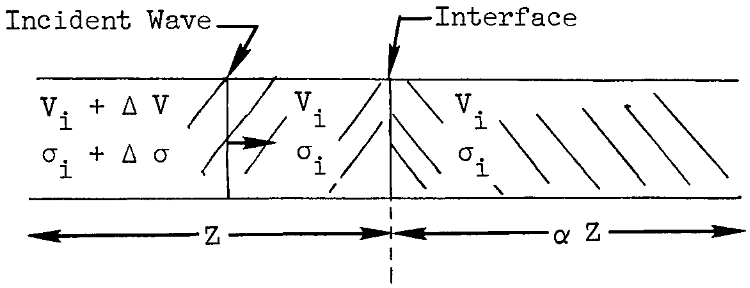

The boundary conditions which must be satisfied after the wave has passed the interface are that the stress level and velocity must be continuous across the interface. If we denote the final velocity and stress by V_f and σ_f, respectively, we find that

$$V_f = V_i + \frac{2\ \Delta V}{1 + \alpha}$$

$$\sigma_f = \sigma_i + \frac{2\ \alpha\ Z\ \Delta V}{1 + \alpha}$$

ADDENDUM A (Continued)

This corresponds to a transmittal wave

$$\Delta V_{TR} = \frac{2}{1+\alpha} \Delta V$$

$$\Delta\sigma_{TR} = \frac{2\alpha Z \Delta V}{1+\alpha} = \frac{2\alpha\Delta\sigma}{1+\alpha}$$

and a reflected wave

$$\Delta V_{RE} = \frac{1-\alpha}{1+\alpha} \Delta V$$

$$\Delta\sigma_{RE} = -\frac{1-\alpha}{1+\alpha} Z \Delta V = -\frac{1-\alpha}{1+\alpha} \Delta\sigma$$

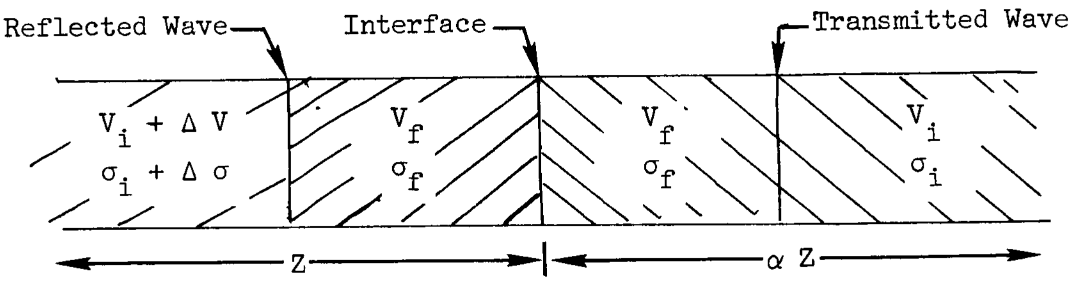

Some special cases of interest, with $\sigma_i = V_i = 0$, are

$\alpha = 0$ Open End

$$\Delta V_{RE} = \Delta V \qquad V_F = 2\Delta V$$

$$\Delta\sigma_{RE} = \Delta\sigma \qquad \sigma_F = 0$$

ADDENDUM A (Continued)

$\alpha \rightarrow \infty$ Closed End

$$\Delta V_{RE} = - \Delta V \qquad V_F = 0$$

$$\Delta\sigma_{RE} = \Delta\sigma \qquad \sigma_F = 2\,\Delta\sigma$$

$\sigma = 1$ Continuous Material

$$\Delta V_{TR} = \Delta V \qquad \Delta V_{RE} = 0$$

$$\Delta\sigma_{TR} = \Delta\sigma \qquad \Delta\sigma_{RE} = 0$$

5. Intersection of Two Waves

When a right running wave and a left running wave cross, each continues unchanged. The material through which both waves have passed respond to the sum of the two effects.

6. Waves Originated by Impact

When two blocks of material impact, stress waves are propagated through both blocks which maintain continuity of velocity and stress across the interface. If both materials are unstressed prior to impact with a relative velocity, V_o as illustrated below,

the stress level after impact will be

$$\sigma_F = \frac{\alpha Z V_o}{1 + \alpha}$$

ADDENDUM A (Continued)

The velocity of the interface after impact will be

$$V_F = \frac{V_o}{1 + \alpha}$$

If both blocks are the same material, $\alpha = 1$ and

$$\sigma_{\alpha = 1} = \frac{Z\ V_o}{2} \quad ; \quad V_{\alpha = 1} = \frac{V_o}{2}$$

7. Wave Diagrams

When analyzing problems in which stress waves are involved, it is convenient to make use of a so-called wave diagram. The ordinate of such a diagram is time while the abscissa is position. Both wave and particle paths can be shown, in principle, but for the present case the particle paths must be shown with an exaggerated slope. They are usually ignored.

The wave construction used in a wave diagram employs the relationships presented above, together with appropriate boundary conditions. At an interface, velocity and pressure are continuous. At an open end the stress level becomes zero. At a closed end, the velocity level becomes zero. A tension wave that reduces the stress level to negative values cannot be transmitted across an interface which has the structural characteristics. In such a case the two materials separate and the stress level becomes zero at the interface.

ADDENDUM A (Continued)

A wave diagram for two blocks of the same size and material which impact is shown below.

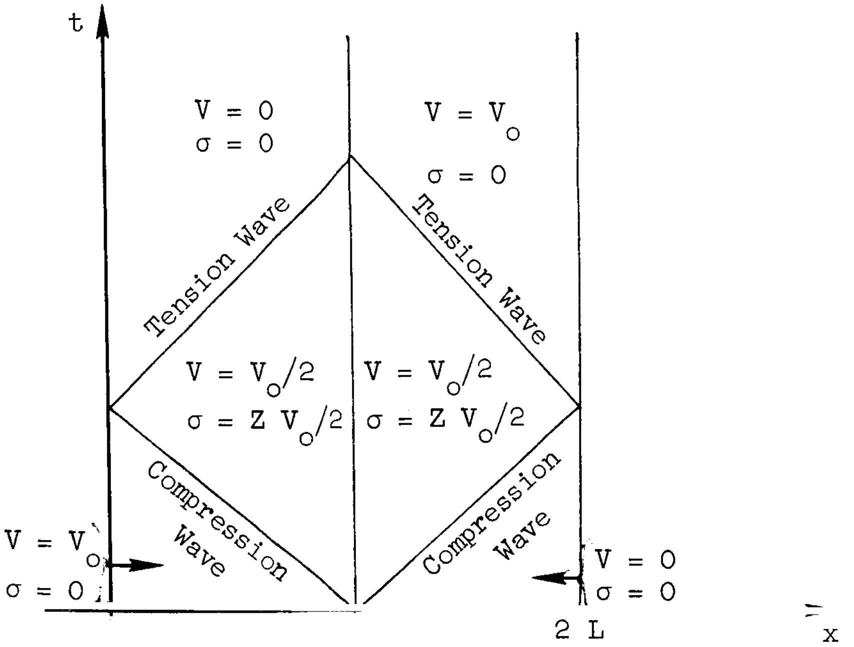

After the two tension waves meet, the first block has stopped while the second one has acquired the original velocity of the first block.

A more detailed analysis of the stress wave diagrams in the present problem is presented in Addendum B.

NOMENCLATURE

Symbol	Description
C	Stress wave velocity
C_o	Velocity of longitudinal waves in a bar
C_1	Wave velocity in an infinite medium (extensional waves)
C_2	Velocity of shear waves
C_L	Velocity of water hammer waves in a pipe
C_{L_1}	Velocity of water hammer waves in an infinite liquid medium
D	Pipe diameter
E	Elastic Modules of stressed medium or of pipe material
f	Coefficient in water hammer velocity equation
h	Thickness of pipe walls
K	Bulk Modulus of liquid
V	Velocity of material propagating stress waves
V_o	Velocity of Block before impact
V_i	Velocity of Material before wave passes
V_f	Velocity of Material after wave passes
ΔV	Velocity change across a stress wave, especially incident wave
ΔV_{TR}	Velocity change across transmitted wave
ΔV_{RE}	Velocity change across reflected wave
x	Position coordinate
Z	Acoustic Impedance
α	Impedance Ratio across Material Interface
λ	Lamé stress constant
μ	Lamé stress constant
ν	Poisson's Ratio
ρ	Material Density
σ	Stress level
σ_i, σ_F, $\Delta\sigma$, $\Delta\sigma_{TR}$, $\Delta\sigma_{RE}$	See corresponding V with subscript

ADDENDUM B

WAVE ANALYSIS OF MARQUARDT TEST APPARATUS

INTRODUCTION

The test apparatus used by The Marquardt Corporation to test rocket thrust chambers, employs a driver or hammer which is allowed to impact on a piston that imparts water hammer waves to a liquid filled cylinder. In order to apply wave analysis to this problem a simplified model is set up below in which only one-dimensional propagation is considered. First a comparison is made between the use of Lagrangian and Eulerian coordinates, then the impact problem is treated separately. Next the liquid column is included, and finally the reflection from the end of the liquid is considered.

1. Lagrangian Coordinates

In order to analyze stress waves in moving bars, one must consider a coordinate system fixed in the material. The wave equations are normally derived for a coordinate system fixed in space (Eulerian coordinates). In conventional coordinates, the equations of motions are

Continuity

$$\frac{\partial \rho}{\partial t} + \frac{\partial \rho u}{\partial x} = 0$$

Momentum

$$\rho \left(\frac{\partial u}{\partial t} + \frac{u \partial u}{\partial x}\right) = \frac{\partial \sigma}{\partial x}$$

Now take a Lagrangian Coordinate System, ξ, τ, such that

$$\tau = t$$

$$\xi = \int_0^x \frac{\rho}{\rho_0} \, d x$$

ADDENDUM B (Continued)

Then ξ represents a coordinate which remains fixed in the material.

To transform the equations of motion, note that

$$\frac{\partial \xi}{\partial x} = \frac{\rho}{\rho_o}$$

$$\frac{\partial \xi}{\partial t} = \int_o^x \frac{\partial}{\partial_t} \left(\frac{\rho}{\rho_o}\right) dx$$

$$= - \int_o^x \frac{\partial}{\partial_x} \left(\frac{\rho\, \upsilon}{\rho_o}\right) dx$$

$$= - \frac{\rho\, \upsilon}{\rho_o}$$

Comparing these, we see that

$$\begin{array}{l||l}
\dfrac{\partial}{\partial x} = \dfrac{\rho}{\rho_o} \dfrac{\partial}{\partial \xi} & \dfrac{\partial}{\partial \xi} = \dfrac{\rho_o}{\rho} \dfrac{\partial}{\partial x} \\[3ex]
\dfrac{\partial}{\partial t} = \dfrac{\partial}{\partial \tau} - \dfrac{\rho\, \upsilon}{\rho_o} \dfrac{\partial}{\partial \xi} & \dfrac{\partial}{\partial \tau} = \dfrac{\partial}{\partial t} + v \dfrac{\partial}{\partial x}
\end{array}$$

Using these transformations, the equations of motion become

$$\frac{\partial \rho}{\partial \tau} + \rho^2 \frac{\partial \upsilon}{\partial \xi} = 0$$

$$\rho \frac{\partial \upsilon}{\partial \tau} = \frac{\rho}{\rho_o} \frac{\partial \sigma}{\partial \xi}$$

$$\frac{\partial x}{\partial \tau} = v$$

ADDENDUM B (Continued)

$$\frac{\partial x}{\partial \xi} = \frac{\rho_o}{\rho}$$

When a material is put under stress, the particles are displaced from their nominal positions. The displacement υ from the unstrained position is

$$\upsilon = x - \xi$$

The strain is given by

$$e = \frac{\partial \upsilon}{\partial \xi}$$

Then

$$\frac{\partial x}{\partial \xi} = 1 + \frac{\partial \upsilon}{\partial \xi} = 1 + e$$

Assuming Hook's law to hold

$$\sigma = Ee = E \frac{\partial \upsilon}{\partial \xi}$$

Then with

$$v = \frac{\partial x}{\partial \tau} = \frac{\partial \upsilon}{\partial \tau}$$

the equations of motion lead to

$$\frac{\partial^2 \upsilon}{\partial \tau^2} = \frac{\theta v}{\partial t} = \frac{1}{\rho_o} \frac{\partial \sigma}{\partial \xi} = \frac{E}{\rho_o} \frac{\partial^2 \upsilon}{\partial \xi^2} = c^2 \frac{\partial^2 \upsilon}{\partial \xi^2}$$

ADDENDUM B (Continued)

Where:

$$c^2 = \frac{E}{\rho_o}$$

Solutions to

$$\frac{\partial^2 \upsilon}{\partial \tau^2} = c^2 \frac{\partial^2 \upsilon}{\partial \xi^2}$$

are of the form

$$\upsilon = \upsilon_L (\tau + \xi/c) + \upsilon_R (\tau - \xi/c)$$

υ_L is a stress wave moving to the left while υ_R is a stress wave moving to the right

The velocity is then given by

$$V = \frac{\partial \upsilon}{\partial_\tau}$$

$$= \upsilon'_L (\tau + \xi/c) + \upsilon'_R (\tau - \xi/c)$$

$$= V_L (\tau + \xi/c) + V_R (\tau - \xi/c)$$

The stress is given by

$$\sigma = E \frac{\partial \upsilon}{\partial \xi}$$

$$= \frac{E}{C} \{\upsilon'_L (\tau + \xi/c) - \upsilon'_R (\tau - \xi/c)\}$$

ADDENDUM B (Continued)

$$= Z \{V_L (\tau + \xi/c) - V_R (\tau - \xi/c)\}$$

$$Z = \frac{E}{C} = \rho_o C$$

The boundary conditions on the solutions are derivable from the momentum, ρ.

$$\rho (t) = \int_0^{x(t)} (\rho V) \Big|_t d x$$

$$d\rho_t = \rho_{t + dt} - \rho_t$$

$$= \int^x [\frac{\partial \rho V}{\partial t} dt] dx + \rho V \frac{dx}{dt} dt$$

If we let $V = \frac{dx}{dt}$ be the rate of motion of the $\xi = \upsilon$ boundary then

$$\frac{d\rho}{dt} = \int^x \frac{\partial \rho v}{\partial t} dx + \rho v V$$

$$= \rho v V + \int^x \frac{\partial}{\partial x} (\sigma - \rho v^2) dx$$

$$= \sigma + \rho v (V - v)$$

At a boundary between regions 1 and 2 that conserve momentum,

$$\rho_{1 + 2} = \int^x (1) + \int_x (2) = \text{constant}$$

$$\frac{d\rho}{dt} = 0$$

ADDENDUM B (Continued)

and

$$\sigma_1 + \rho_1 v_1 (V - v_1) = \sigma_2 + \rho_2 v_2 (V - v_2)$$

and similarly

$$\rho_1 (V - v_1) = \rho_2 (V - v_2)$$

At the end of two bars at impact,

$$v_1 = v_2 = V$$

and therefore

$$\sigma_1 = \sigma_2$$

We can conclude that small displacement theory is exact if we use υ = displacement from original position and $x = \xi + \upsilon$.

Impact of Two Equal Bars

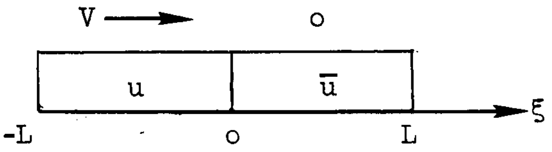

At impact, $\upsilon = V\tau$, $\bar{\upsilon} = 0$ $(\tau \leq 0)$

ADDENDUM B (Continued)

To express the situation after impact, we will define a ramp operator $< >$ such that

$$< x > \equiv 0 \quad \text{if } x < 0$$

$$< x > \equiv x \quad \text{if } x > 0$$

The derivative of the ramp operator is the unit step function

$$S(x) \equiv 0 \text{ if } x < 0$$

$$S(x) \equiv 1 \text{ if } x > 0$$

The wave diagram for the impact is shown below.

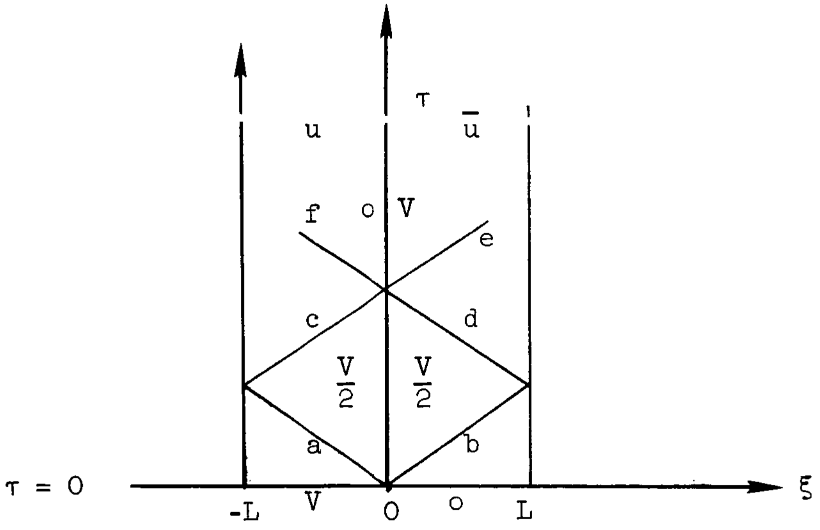

a, b, c, etc., are the wave strengths expressed in terms of velocity increments. After impact

ADDENDUM B (Continued)

$$\upsilon = V\tau + a < \tau + \xi/c > + c < (\tau - \frac{L}{C}) - (\frac{\xi + L}{c}) >$$

$$+ f < (\tau - \frac{2L}{c}) + \xi/c > + \ldots\ldots\ldots$$

$$\bar{\upsilon} = b < t - \xi/c > + d < (\tau - \frac{L}{c}) + (\frac{\xi - L}{c}) >$$

$$+ e < (\tau - \frac{2L}{c}) - \xi/c > + \ldots\ldots\ldots$$

For $\sigma = 0$ at impact, we find

$$b = d = - a = - c = \frac{V}{2}$$

then

$$x = \upsilon + \xi'$$

$$= \xi + V\tau - \frac{V}{2} [< \tau + \xi/c > + < (\tau - \frac{L}{c}) - (\frac{\xi + L}{c}) >]$$

$$\bar{x} = \bar{\upsilon} + \xi$$

$$= \xi + \frac{V}{2} [< \tau - \frac{\xi}{c} > + < (\tau - \frac{L}{c}) + (\frac{\xi - L}{c}) >]$$

The position of the particles in the bars is shown below

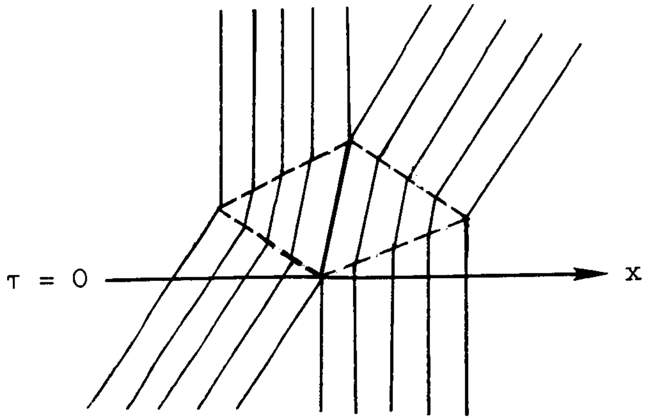

ADDENDUM B (Continued)

The velocity if found from

$$v = \frac{\partial u}{\partial t} = V - \frac{V}{2} [S (\tau + \xi/c) + S (\tau - \frac{2L}{c} - \frac{\xi}{c})]$$

$$\bar{v} = \frac{\partial \bar{u}}{\partial \tau} = \frac{V}{2} [S (\tau - \frac{\xi}{c}) + S (\tau - \frac{2L}{c} + \frac{\xi}{c})]$$

the stress is

$$\sigma = -Z \frac{V}{2} [S (\tau + \xi/c) - S (\tau - \frac{2L}{c} - \frac{\xi}{c})]$$

$$\bar{\sigma} = -Z \frac{V}{2} [S (\tau - \frac{\xi}{c}) - S (\tau - \frac{2L}{c} + \frac{\xi}{c})]$$

Impact of Bars of Unequal Length

In the above example, the bars separated with zero stress in each bar after $\tau = \frac{2L}{c}$. The wave diagrams for bars of unequal length are shown below. In each case the bars separate with no stress in the shorter bar, but with stress waves trapped in the shorter bar. Both energy and momentum are conserved by the impact, but some of the energy is tied up in the wave system.

ADDENDUM B (Continued)

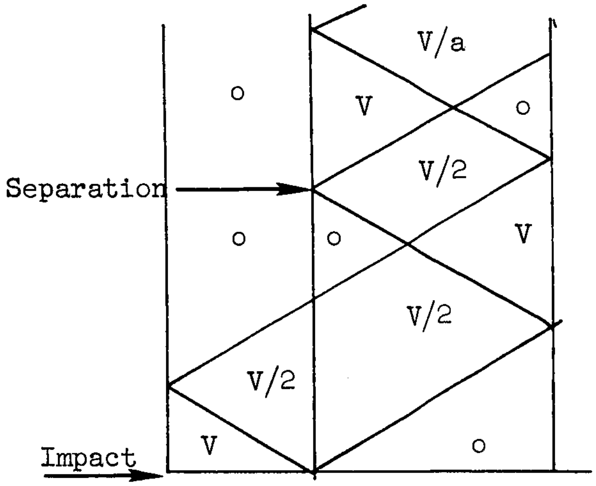

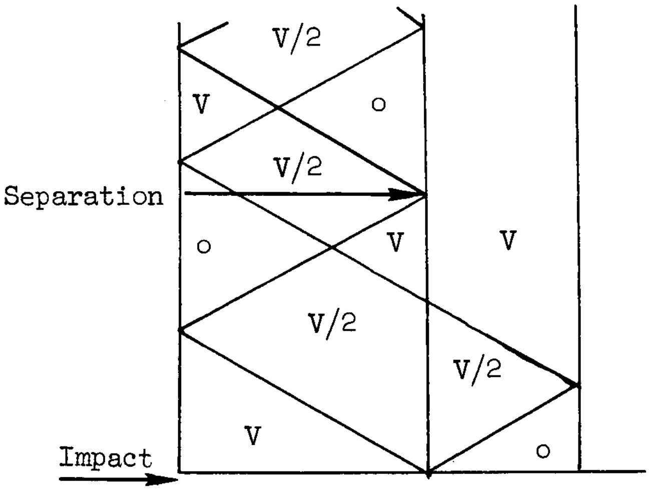

On this basis, the maximum velocity which the second bar could achieve would be V. This result is a consequence of the special geometry of the system. By using a flat plate to strike a solid bar, or a ball to strike a plate, this situation would change. In order to simulate a system in which no energy is tied up in stress waves after impact, one can assume that the density of the first bar differs from that of the second, but that they have the same length. Then the final velocities agree with those found from ordinary rigid body analysis. In a real system the amount of energy tied up in stress waves will not, in general, be zero. The exact magnitude of this quantity can be found by measuring the so-called coefficient of restitution for the system.

Hammer, Piston, and Liquid

In the Marquardt test apparatus, the second mass is in direct contact with a column of fluid. While the impendance of this fluid is small compared to that of the piston, it is not zero. The reflected waves from the piston fluid interface are therefore somewhat less intense and the stress time picture is altered. The water hammer waves generated in the fluid can be determined by a wave analysis similar to that shown for the impact analysis above. The piston has impedance Z and wave velocity c. The length of the piston is L.

The hammer properties are assumed to be

$$Z_H = \mu Z$$

$$c_H = c$$

$$L_H = L$$

The fluid properties are assumed to be

$$Z_L = \alpha Z$$

$$c_L \ll C$$

$$L_L \gg L$$

The wave diagram is shown below

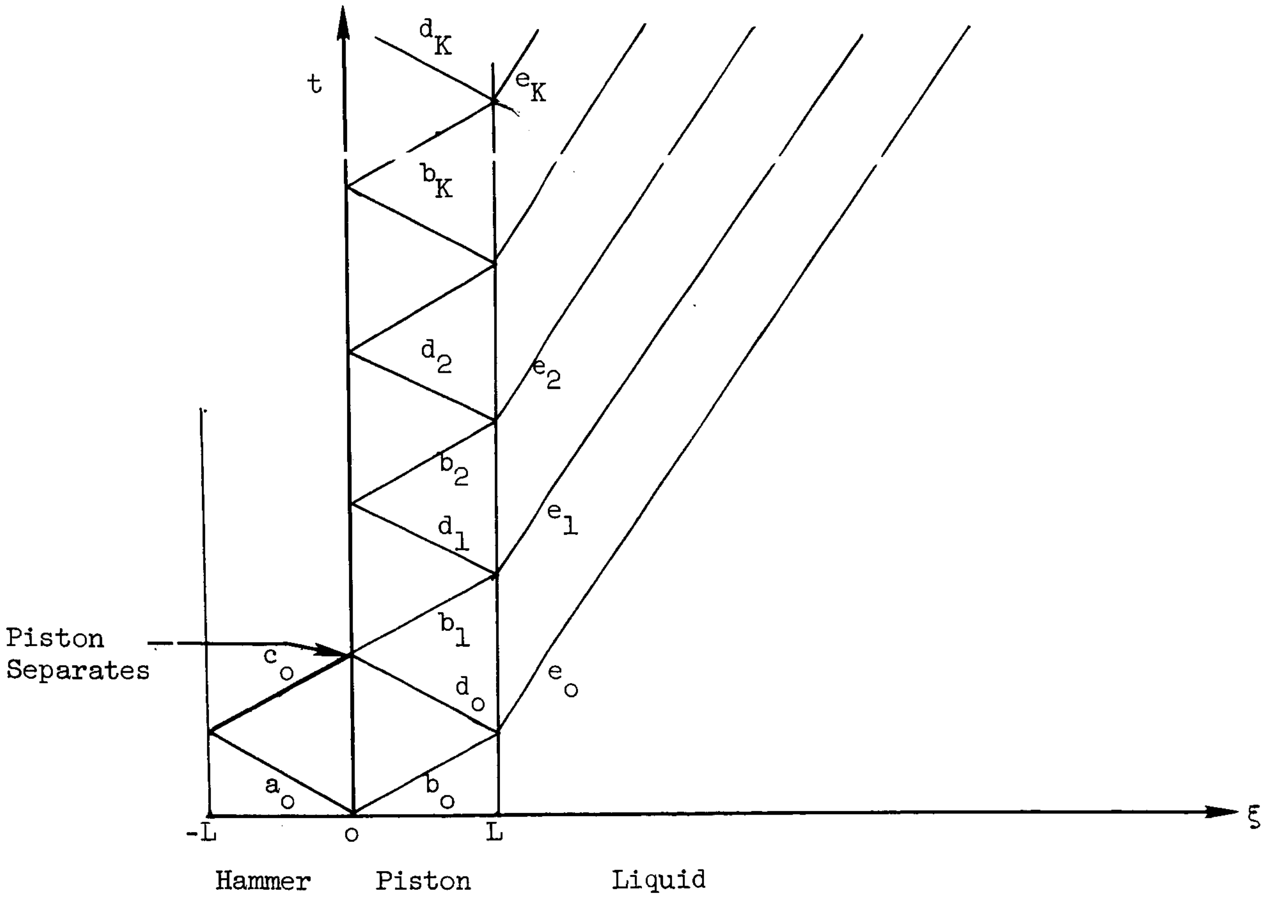

ADDENDUM B (Continued)

To simplify the algebraic expressions, we adopt the following notation:

$\langle + \rangle$ represents a left running wave

$\langle - \rangle$ represents a right running wave

$$\begin{aligned} \langle + \rangle_j &= \left\langle \left(t - \frac{j\,L}{c}\right) + \frac{\xi}{c} \right\rangle \\ \langle - \rangle_j &= \left\langle \left(\tau - \frac{j\,L}{c}\right) - \frac{\xi}{c} \right\rangle \end{aligned} \qquad -L \le \xi \le L$$

$$\left.\begin{aligned} \langle - \rangle_j' &= \left\langle \left(\tau - \frac{(j+1)\,L}{c}\right) - \frac{(\xi - L)}{c_L} \right\rangle \\ \langle + \rangle_j' &= \left\langle \left(\tau - \frac{(j+1)\,L}{c}\right) + \frac{(\xi - L)}{c_L} \right\rangle \end{aligned}\right\} \quad \xi \ge L$$

Then for an initial impact velocity of V

$$\upsilon_h = V\left[\tau - a_o \langle + \rangle_o - c_o \langle - \rangle_1\right]$$

$$\upsilon_p = V\left[b_o \langle - \rangle_o + d_o \langle + \rangle_1 + b_1 \langle - \rangle_2 + d_1 \langle + \rangle_3 \cdots\cdots\right]$$

$$= V \sum_{K=0} \left[b_K \langle - \rangle_{2K} + d_K \langle + \rangle_{2K+1}\right]$$

$$\upsilon_L = V\left[e_o \langle - \rangle_o' + e_1 \langle - \rangle_2' + e_2 \langle - \rangle_4' \cdots\cdots\right]$$

$$= V \sum_{K=0} e_K \langle - \rangle_{2K}'$$

The boundary conditions are that $V_\rho = V_n$ at $\xi = 0$ from $\tau = \upsilon$ until $\tau = \frac{2\,L}{c}$ after which the hammer and piston separate; the $\sigma_h = \sigma_\rho$ during their contact time at $\xi = 0$; that $\sigma_h = 0$ at $\xi = -L$; that $\sigma_\rho = -P_L$ and $V_\rho = V_L$ at $\xi = L$; that $\sigma_\rho = 0$ at $\xi = 0$ after $t = 2\,L/c$.

ADDENDUM B (Continued)

Note that:

$$V = \frac{\partial \upsilon}{\partial t} \qquad \sigma = Z\, c \frac{\partial \upsilon}{\partial \xi} \qquad \text{(using appropriate Z and c)}$$

$$\frac{\partial < + >_j}{\partial \tau} = S_j (+) \equiv S \left[\left(\tau - \frac{j\,L}{c}\right) + \frac{\xi}{c}\right]$$

$$\frac{\partial < - >_j}{\partial \tau} = S_j (-) \equiv S \left[\left(\tau - \frac{j\,L}{c}\right) - \frac{\xi}{c}\right]$$

$$\frac{\partial < - >_j'}{\partial \tau} = S_j' (-) \equiv S \left[\left(\tau - \frac{(j+1)\,L}{c}\right) - \frac{\xi - L}{c_L}\right]$$

$$\frac{\partial < + >_j}{\partial \xi} = \frac{S_j (+)}{c}$$

$$\frac{\partial < - >_j}{\partial \xi} = - \frac{S_j (-)}{c}$$

$$\frac{\partial < - >_j'}{\partial \xi} = - \frac{S_j' (-)}{c_L}$$

Applying the boundary conditions yields

$$\xi = 0, \quad \tau = 0 \; : \; 1 - a_o = b_o$$

$$\xi = 0, \quad \tau = 0 \; : \; - \mu\, Z\, a_o = - Z\, b_o$$

$$\xi = - L, \quad \tau = \frac{L}{c} \; : \; - a_o + c_o = 0$$

ADDENDUM B (Continued)

Therefore

$$c_o = a_o = \frac{1}{\mu + 1}$$

and

$$b_o = \frac{\mu}{\mu + 1}$$

Let

$$\beta_n \equiv \sum^{n} b_k$$

$$\delta_n \equiv \sum_{K=0} d_k$$

$$\epsilon_n \equiv \sum_{K=0}^{n} e_n$$

Then

$$\xi = 0, \tau = \frac{2(n + 1) L}{c} \quad : \quad \beta_{n+1} = \delta_n$$

$$\xi = L, \tau = \frac{(2 n + 1) L}{c} \quad : \quad \beta_n + \delta_n = \epsilon_n$$

$$\xi = L, \tau = \frac{(2 n + 1) L}{c} \quad : \quad Z (\beta_n - \delta_n) = - \alpha Z \epsilon_n$$

ADDENDUM B (Continued)

Solving for β, δ, ϵ yields

$$\beta_n = \frac{1 + \alpha}{2} \epsilon_n$$

$$\delta_n = \frac{1 - \alpha}{2} \epsilon_n$$

$$\epsilon_n = \frac{1 - \alpha}{1 + \alpha} \epsilon_{n - 1}$$

But

$$\epsilon_o = \frac{2}{1 + \alpha} \beta_o = \left(\frac{2}{1 + \alpha}\right)\left(\frac{\mu}{1 + \mu}\right)$$

so that

$$\epsilon_n = \left(\frac{1 - \alpha}{1 + \alpha}\right)^n \left(\frac{2}{1 + \alpha}\right)\left(\frac{\mu}{1 + \mu}\right)$$

$$\beta_n = \frac{1 + \alpha}{2} \epsilon_n$$

$$= \left(\frac{1 - \alpha}{1 + \alpha}\right)^n \frac{\mu}{1 + \mu}$$

$$\delta_n = \left(\frac{1 - \alpha}{2}\right) \epsilon_n$$

$$= \left(\frac{1 - \alpha}{1 + \alpha}\right)^{n + 1} \frac{\mu}{1 + \mu}$$

ADDENDUM B (Continued)

The pressure in the liquid is found from

$$P = \alpha Z c_L \frac{\partial \upsilon_L}{\partial \xi}$$

$$= + \alpha Z V \sum_{K = 0} e_k S'_{2k}$$

and

$$P_n = + \alpha Z \epsilon_n V$$ after passage of the e_n wave.

A plot P versus τ at the piston face would have the appearance sketched below. This ignores the possibility that the hammer will again strike the piston. If μ is greater than 1.0, this will eventually occur.

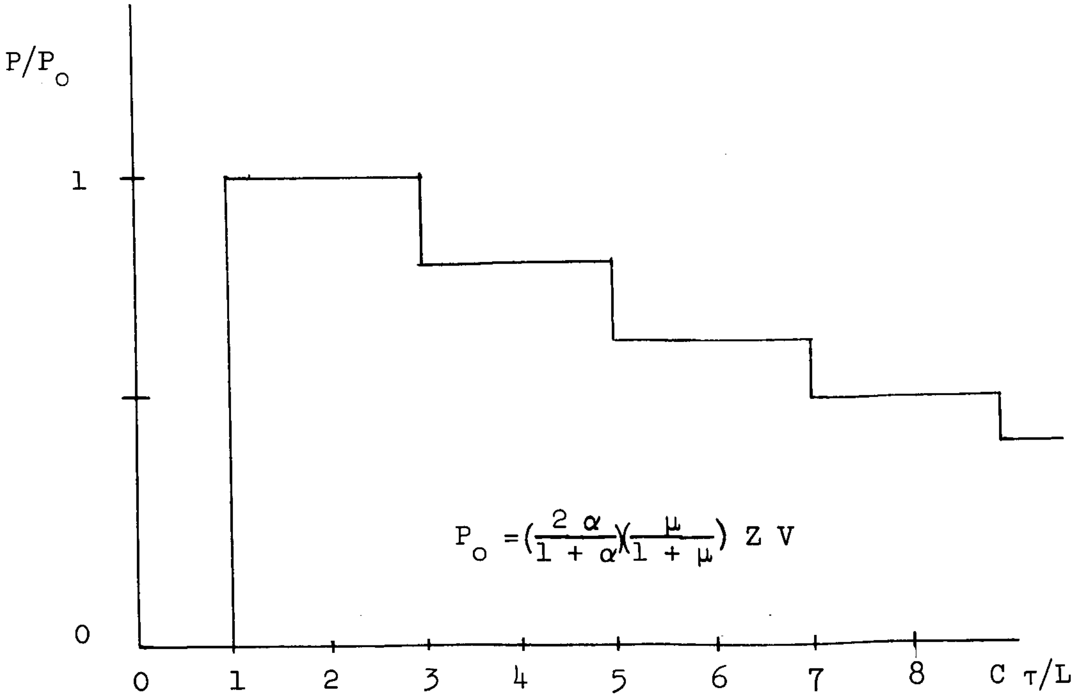

$$P_o = \left(\frac{2\alpha}{1 + \alpha}\right)\left(\frac{\mu}{1 + \mu}\right) Z V$$

ADDENDUM B (Continued)

This is a step function equivalent to an exponential decay with time constant of $-\frac{2}{\ln(1-\alpha/1+\alpha)} \approx \frac{1}{\alpha}$

Hammer, Piston, Liquid, and Wall

When the waves in the liquid reach the end of the chamber, they are reflected back towards the piston. The nature of the reflection depends on the chamber termination. This termination will be assumed here to be a wall of metal such that

$$Z_L = \alpha' Z_w$$

The wave diagram now appears as shown below.

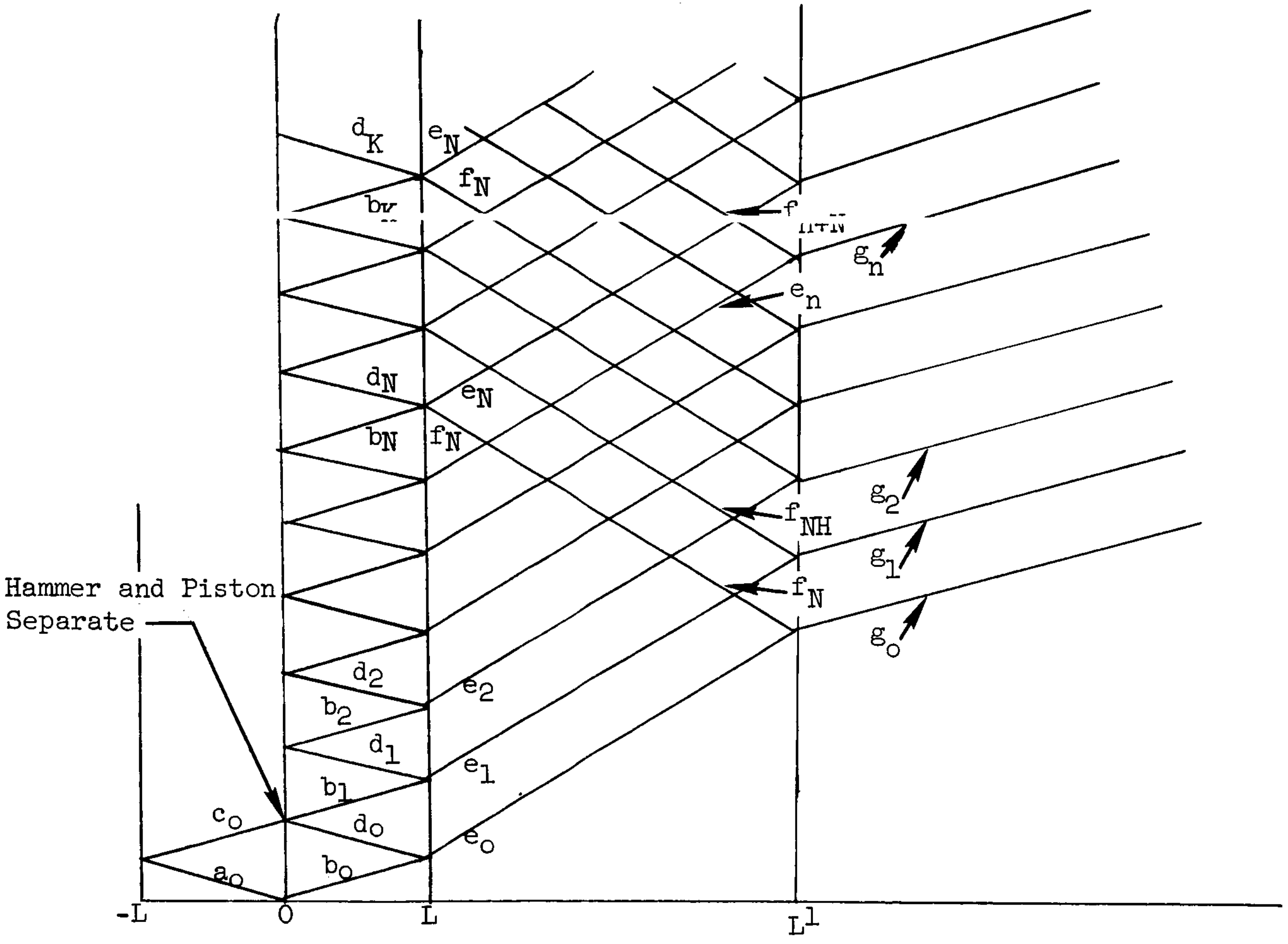

Reflected wave assumed to reach piston after N reflections in piston (at K = N).

ADDENDUM B (Continued)

The displacements are now given by

$$\upsilon_h = V\,(\tau - a_o < + >_o - c_o < - >_o)$$

$$\upsilon_P = V \sum_{k=0} (b_k < - >_{2k} + d_k < + >_{2k+1})$$

$$\upsilon_L = V\,[\sum_{k=0} e_k < - >_{2k} + \sum_{k=N} f_k < + >_{2k}]$$

$$\upsilon_w = V \sum_{k=0} g_k < - >''_{2k}$$

where

$$< - >''_j \equiv < (\tau - \frac{(L' - L)}{c_L} - \frac{(j + 1)\ L}{c} - \frac{(\xi - L')}{c} >$$

Defining

$$\varphi_n = \sum_N^n f_k \quad (\varphi_n = 0 \text{ for } n < [N - 1])$$

$$\gamma_n = \sum_o^n g_k$$

We can apply the boundary conditions to obtain $\xi = 0, \ \tau = 0$

$\xi = 0, \ \tau = 0$ $\qquad 1 - a_o = b_o$

$$- \mu Z a_o = - Z b_o$$

$\xi = - L, \ \tau = \frac{L}{c}$ $\qquad - a_o + c_o = 0$

ADDENDUM B (Continued)

Therefore, as before

$$c_o = a_o = \frac{1}{\mu + 1}$$

$$b_o = \frac{\mu}{\mu + 1}$$

The previous solutions for β_n, δ_n, and ϵ_n are also applicable, until the reflected wave returns ($\eta = N$). The magnitude of the reflected wave is found from

$$\xi = L', \tau = \frac{(2\eta + 1) L}{c} - \frac{L' - L}{c_L} : \sum_{k=0}^{\eta} e_k + \sum_{k=N}^{N+\eta} f_k = \sum_{k=0}^{\eta} g_k$$

$$\alpha' \left(- \sum_{k=0}^{n} e_k + \sum_{k=N}^{N+\eta} f_k\right) = - \sum_{k=0}^{\eta} g_k$$

or

$$\epsilon_\eta + \varphi_{\eta + N} = \gamma_\eta$$

$$\alpha' (- \epsilon_\eta + \varphi_{\eta + N}) = - \gamma_\eta$$

Eliminating γ_η

$$\varphi_{\eta + N} = - \epsilon_\eta \left(\frac{1 - \alpha'}{\alpha' + 1}\right)$$

ADDENDUM B (Continued)

and

$$\gamma_\eta = \epsilon_\eta \frac{2\alpha'}{\alpha' + 1}$$

The boundary condition for $\eta \geqslant N$ at $\xi = L$ becomes

$$\beta_\eta + \delta_\eta = \epsilon_\eta + \phi_\eta$$

$$-\beta_\eta + \delta_\eta = \alpha(-\epsilon_\eta + \varphi_\eta)$$

Eliminating δ_η

$$\beta_\eta = \frac{\alpha + 1}{2}\epsilon_\eta + \frac{1 - \alpha}{2}\varphi_\eta$$

But

$$\varphi_\eta = -\frac{1 - \alpha'}{1 + \alpha'}\epsilon_\eta - N$$

So that

$$\beta_\eta = \frac{\alpha + 1}{2}\epsilon_\eta - \frac{1 - \alpha}{2}\left(\frac{1 - \alpha'}{\alpha' + 1}\right)\epsilon_\eta - N$$

Similarly

$$\delta_\eta = \frac{1 - \alpha}{2}\epsilon_\eta - \frac{1 + \alpha}{2}\left(\frac{1 - \alpha'}{1 + \alpha'}\right)\epsilon_\eta - N$$

Finally, note that for any $\eta > 0$, there is no stress at $\xi = 0$

$$\beta_\eta = \delta_\eta - 1$$

ADDENDUM B (Continued)

Now consider β_N and ϵ_o

$$\beta_N = \left(\frac{1 - \alpha}{1 + \alpha}\right)^N \frac{\mu}{1 + \mu}$$

$$\epsilon_o = \left(\frac{2}{1 + \alpha}\right)\left(\frac{\mu}{1 + \mu}\right)$$

Then

$$\epsilon_N = \frac{2}{\alpha + 1} \left[\beta_N + \frac{1 - \alpha}{2} \left(\frac{1 - \alpha'}{1 + \alpha'}\right) \epsilon_o\right]$$

$$= \frac{\mu}{1 + \mu} \left[\frac{2}{\alpha + 1} \left(\frac{1 - \alpha}{1 + \alpha}\right)^N + \frac{2}{1 + \alpha} \left(\frac{1 - \alpha}{1 + \alpha}\right) \left(\frac{1 - \alpha'}{1 + \alpha'}\right)\right]$$

$$= \epsilon_o \left[\left(\frac{1 - \alpha}{1 + \alpha}\right)^N + \left(\frac{1 - \alpha}{1 + \alpha}\right) \left(\frac{1 - \alpha'}{1 + \alpha'}\right)\right]$$

$$\delta_N = \frac{1 - \alpha}{2} \epsilon_N - \frac{1 + \alpha}{2} \left(\frac{1 - \alpha'}{1 + \alpha'}\right) \epsilon_o$$

$$= \left(\frac{1 - \alpha}{1 + \alpha}\right)^{N + 1} \frac{\mu}{1 + \mu} - \left(\frac{2\alpha}{1 + \alpha}\right)\left(\frac{1 - \alpha'}{1 + \alpha'}\right)\epsilon_o$$

$$= \frac{\mu}{1 + \mu} \left[\left(\frac{1 - \alpha}{1 + \alpha}\right)^{N + 1} - \frac{4 \alpha}{(1 + \alpha)^2} \left(\frac{1 - \alpha'}{1 + \alpha'}\right)\right]$$

Then, since $\beta_\eta = \delta_{\eta - 1}$

$$\beta_{N + 1} = \delta_N$$

ADDENDUM B (Continued)

and

$$\epsilon_{N+1} = \frac{2}{\alpha + 1} [\beta_{N+1} + \frac{1 - \alpha}{2} (\frac{1 - \alpha'}{1 + \alpha'}) \epsilon_1]$$

$$\epsilon_{N+1} = (\frac{2}{\alpha + 1})(\frac{\mu}{1 + \mu}) (\frac{1 - \alpha}{1 + \alpha})^{N+1} - \frac{4\alpha}{(1 + \alpha)^2} (\frac{1 - \alpha'}{1 + \alpha'}) \epsilon_o + (\frac{1 - \alpha}{1 + \alpha})(\frac{1 - \alpha'}{1 + \alpha'}) \epsilon_1$$

But

$$\epsilon_1 = \frac{1 - \alpha}{1 + \alpha} \epsilon_o$$

So that

$$\epsilon_{N+1} = \epsilon_o [(\frac{1 - \alpha}{1 + \alpha})^{N+1} + (\frac{1 - \alpha'}{1 + \alpha'}) (\frac{(1 - \alpha)^2 - 4\alpha}{(1 + \alpha)^2})]$$

and

$$\delta_{N+1} = \frac{1 - \alpha}{2} \epsilon_{N+1} - \frac{1 + \alpha}{2} (\frac{1 - \alpha'}{1 + \alpha'}) \epsilon_1$$

$$= \frac{\mu}{1 + \mu} (\frac{1 - \alpha}{1 + \alpha})^{N+2} - \frac{8\alpha}{(1 + \alpha)^2} (\frac{1 - \alpha'}{1 + \alpha'}) \epsilon_o$$

$$= \frac{\mu}{1 + \mu} [(\frac{1 - \alpha}{1 + \alpha})^{N+2} - \frac{16\,\alpha}{(1 + \alpha)^3} (\frac{1 - \alpha'}{1 + \alpha'})]$$

$$= \beta_{N+2}$$

ADDENDUM B (Continued)

Similarly

$$\delta_{N+2} = \frac{\mu}{1+\mu} \left(\frac{1-\alpha}{1+\alpha}\right)^{N+3} + \frac{1-\alpha}{2} \left(\frac{1-\alpha'}{1+\alpha'}\right) \frac{(21\alpha + 2\alpha^2 + \alpha^3)}{(1+\alpha)^3} \epsilon_o$$

$$= \frac{\mu}{1+\mu} \left[\left(\frac{1-\alpha}{1+\alpha}\right)^{N+3} + \left(\frac{1-\alpha}{1+\alpha}\right) \left(\frac{21\alpha + 2\alpha^2 + \alpha^3}{(1+\alpha)^3}\right) \left(\frac{1-\alpha'}{1+\alpha'}\right)\right]$$

$$= \beta_{N+3}$$

and so forth.

A general form can be obtained by means of difference equations. The results are given below.

Let

$$\theta = \frac{1-\alpha}{1+\alpha}$$

$$\eta = \frac{1-\alpha'}{1+\alpha'}$$

Then

$$\epsilon_\eta = (1+\theta)\,\theta^\eta \{ 1 \qquad \eta < N$$

$$+ \eta\,\theta^{-N-1} [\theta^2 + (\theta^2 - 1) \tbinom{\eta - N}{1}] \qquad N < \eta < 2N$$

$$+ \eta^2\,\theta^{-2N-2} [\theta^4 + 2\,\theta^2(\theta^2 - 1) \tbinom{n - 2N}{1} + (\theta^2-1)^2 \tbinom{\eta - 2N}{2}] \quad 2N < \eta < 3N$$

$$+ \eta^3\,\theta^{-3N-3} [\theta^6 + 3\theta^4(\theta^2-1)\tbinom{\eta - 3N}{1} + 3\,(\theta^2-1)^2\,\theta^2 \tbinom{\eta - 3N}{2}$$

$$+ (\theta^2-1)^3 \tbinom{\eta - 3N}{3}] \qquad 3N < \eta < 4N$$

ADDENDUM B (Continued)

$$+ \eta^4 \, \theta^{-4N-4} \, [\theta^8 + 4\theta^6 (\theta^2 - 1) \binom{\eta-4N}{1} + \ldots.] \quad 4N < \eta < 5N$$

$$+ \ldots\ldots\ldots\ldots\ldots\ldots\ldots\ldots\ldots\ldots\}$$

Each term becomes effective as noted to the right.

The pressure in the liquid can again be found from

$$P = - \alpha \, Z \, c_L \frac{\partial \upsilon_L}{\partial \xi}$$

$$= \alpha \, Z \, V \, [\sum_{k=0} e_k \, S'_{2k} (+) - \sum_{k=N} f_k \, S'_{2k} (-)]$$

Pressure at the piston face will be found from the fact that both waves of the e and f families intersect there for the same k. Therefore at

$$t = \frac{(2\eta + 1) \, L}{c}$$

$$P_{L_\eta} = \alpha \, Z \, V \, (\epsilon_\eta - \varphi_\eta)$$

$$= \alpha \, Z \, V \, (\epsilon_\eta + \eta \, \epsilon_{\eta - N})$$

Pressure at the wall will be found from the fact that the nth wave of the e family intersects the $(\eta + N)^{th}$ member of the f family. Therefore at

ADDENDUM B (Continued)

$$\tau = \frac{(2\eta + 1)\,L}{c} - \frac{L' - L}{c_L} = \frac{[2\,(\eta - N) + 1]L}{c} + \frac{L' - L}{c_L}$$

$$P_\eta = \alpha\, Z\, V\, (\epsilon_\eta - \varphi_{\eta + N})$$

$$= \alpha\, Z\, V\, (1 + \eta)\, \epsilon_\eta$$

To see how the pressure will vary with time, consider two cases

I) Metal wall, $C_L = 1/4\ c$, $\alpha = \alpha' = 0.026$, $L' = 2.5\ L$

then $\eta = \theta = 0.950$, $N = 6$

This case is plotted in Figure B-1. The negative pressures are not real.

II) Metal wall, $c_L = 1/10\ c$, $\alpha = \alpha' = 0.17$, $L' = 2.5L$

then $\eta = \theta = 0.71$, $N = 15$.

This case is plotted in Figure 8-2.

The analysis shown here does not consider the possibility of additional impacts between the hammer and piston. These will occur unless $\mu < 1$.

Pressure-Time Variation At Piston

Including End Reflection Effects

Low Impedance Liquid

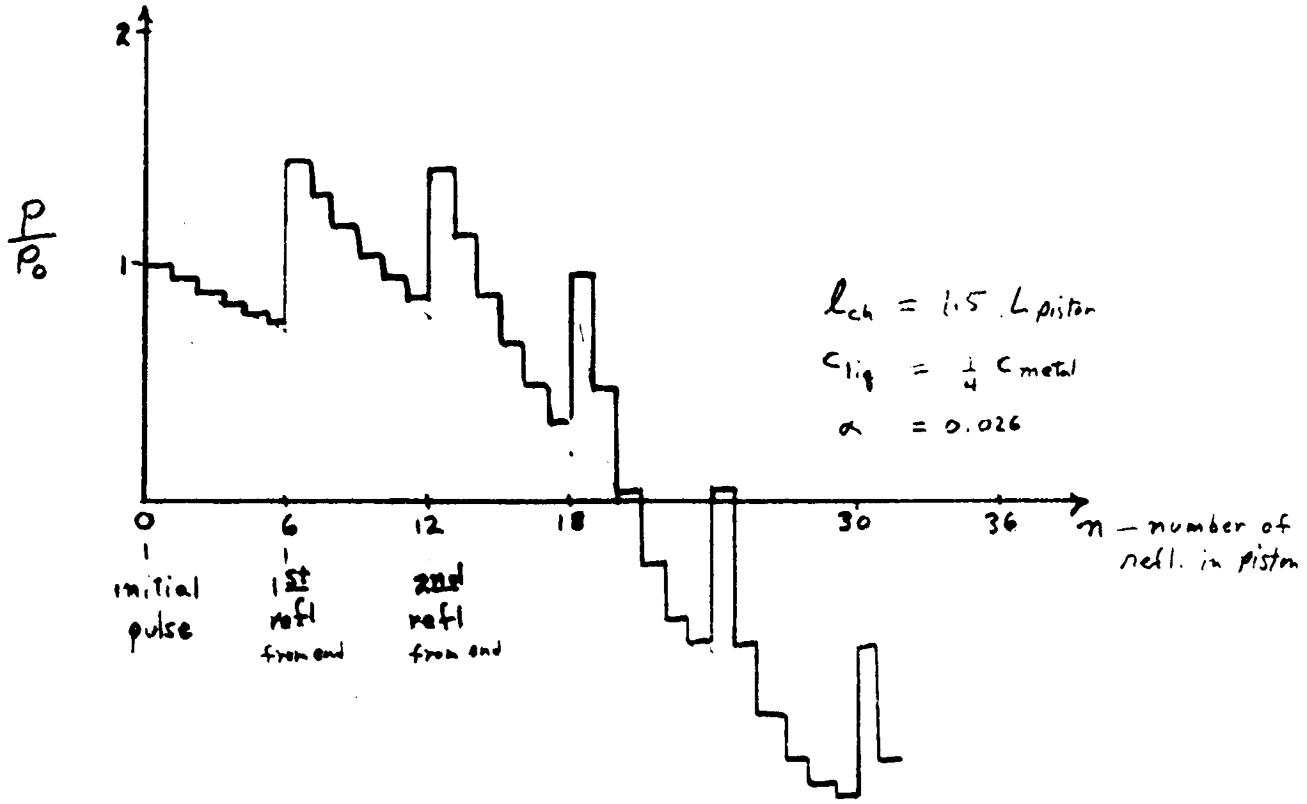

FIGURE B-1

Pressure Time Variation At Piston

Including End Reflection Effects

High Impedance Liquid

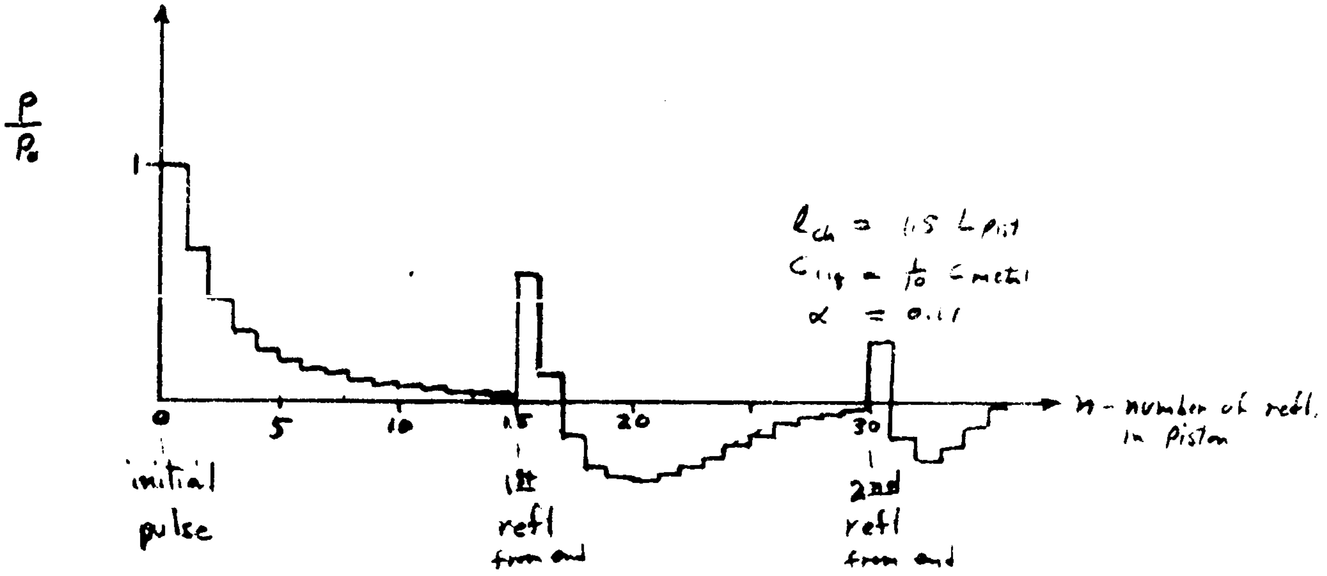

FIGURE B-2

ADDENDUM C

EFFECT OF THE TERMINATION ON THE REFLECTION

When the stress waves in the liquid reach the far end of the chamber, they are reflected back towards the piston. The nature of this reflection depends on the elastic nature of the termination of the chamber. Three types of chamber termination are considered below; an elastic termination, a massless springlike termination, and a termination which has mass-spring characteristics.

Elastic Termination

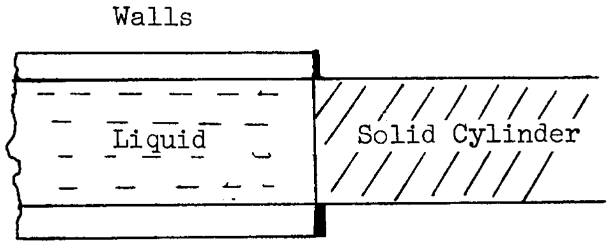

If the impedance of the liquid is Z_L and the impedance of the solid cylinder is Z_S, and if

$$\zeta = \frac{Z_L}{Z_S}$$

then the amplitude of the pressure behind the reflected wave will be

$$P = \frac{2}{1 + \zeta} P_o$$

where P_o is the pressure level behind the incident wave.

ADDENDUM C (Continued)

Springlike Termination

An incident wave of amplitude P_o arrives at the end. Since the end has not been displaced, the stress on the liquid from the end is zero. The initial reflected wave has zero stress and a doubled velocity. It is an expansion wave behind which

$$P\ (t = 0) = 0$$

$$V\ (t = 0) = -2\frac{P_o}{Z_L}$$

As the end moves, the tension in the shell applies pressure to the liquid.

The stress is given by

$$\sigma_x = -E\frac{\Delta \ell}{\ell}$$

The pressure on the liquid is then

$$P = -\frac{4\ h\ \sigma_x}{D}$$

$$= \frac{4\ h\ E\ \Delta\ell}{D\ell}$$

The increase in pressure causes a compression wave train to be propagated through the liquid, reducing the velocity of the termination

$$\frac{dV}{dt} = -\frac{1}{Z_L}\ \frac{dp}{dt}$$

ADDENDUM B (Continued)

But

$$v = \frac{d\,\Delta\ell}{dt}$$

therefore

$$\frac{dv}{dt} = -\frac{4}{D}\frac{h\,E}{Z_L\ell}\,v$$

which yields

$$V = V_o\, e^{-\frac{t}{\tau}}$$

where

$$V_o = V(t = o) = -2\,\frac{P_o}{Z_L}$$

$$\tau = \frac{D\,Z_L\,\ell}{4\,h\,E}$$

we can now find P and σ_x

$$P = \frac{4\,h\,E\,\Delta\ell}{D\ell}$$

$$= \frac{Z_L}{\tau}\int_o^t v\,d\,t$$

$$P = 2\,P_o\,(1 - e^{-t/\tau})$$

$$\sigma_x = \frac{P_o D}{2h}\,(1 - e^{-t/\tau})$$

ADDENDUM C (Continued)

Mass-Spring Termination

If the termination is assumed to have a mass, m, and also exhibit springlike characterisitcs, the analysis becomes somewhat more complex. From Newton's Law we obtain

$$m \frac{dv}{dt} = P \frac{\pi}{4} D^2 + \sigma_x \pi D h$$

Again assuming

$$\sigma_x = - \frac{E \Delta \ell}{\ell}$$

$$v = \frac{d \Delta \ell}{dt}$$

and

$$\frac{dP}{dt} = Z_L \frac{dv}{dt}$$

we obtain

$$m \frac{d^2 v}{dt^2} + \frac{\pi D^2}{4} Z_L \frac{dv}{dt} + \frac{\pi D h E}{\ell} v = 0$$

If we let

$$\omega_N^2 = \frac{\pi D h E}{m \ell}$$

and

$$2 \lambda = \frac{\pi D^2 Z_L}{4 m}$$

ADDENDUM C (Continued)

and

$$\omega' = \sqrt{\omega_N^2 - \lambda^2}$$

Then the solution becomes that of a damped oscillator with

$$v = A e^{-\lambda t} e^{\pm i \omega' t}$$

The system is critically damped when

$$\lambda^2 = \omega_N^2$$

or

$$m_c = \frac{\pi D^3 Z_L^2 \ell}{64 h E}$$

For larger m, the system will oscillate. For smaller m it is over-damped. The system under study is oscillatory.

Solving for A when the initial conditions that

$$v (t = o) = 0$$

$$\sigma_x (t = o) = 0$$

yields

$$v = \frac{4 P_o}{Z} \frac{\lambda}{\omega'} e^{-\lambda t} \operatorname{Sin} \omega' t$$

ADDENDUM C (Continued)

$$P = 2 P_o \left[1 - \frac{2\lambda}{\omega'} e^{-\lambda t} \operatorname{Sin} \omega' t \right]$$

$$\sigma_x = \frac{P_o D}{2 h} \left[1 + e^{-\lambda t} \left(\frac{\lambda}{\omega'} \operatorname{Sin} \omega' t - \cos \omega' t \right) \right]$$

Solving for the maximum pressure and the maximum stress

$$P_{max} = 2 P_o \left[1 + \frac{2\lambda}{\omega_N} e^{-\frac{\lambda}{\omega'} \tan^{-1} \left(\frac{\omega'}{\lambda} \right)} \right]$$

$$\text{at } t = \frac{1}{\omega'} \tan^{-1} \left(\frac{\omega'}{\lambda} \right)$$

$$\sigma_{max} = \frac{P_o D}{2 h} \left[1 + e^{-\pi \frac{\lambda}{\omega'}} \right]$$

$$\text{at } t = \frac{\pi}{\omega'}$$

ADDENDUM C (Continued)

Numerical Examples

Given Values

$D = 2''$

$\ell = 3''$

$h = 0.11''$

$E = 3 \times 10^7$ psi

$Z_L = 60.3$ psi sec/ft for H_2O

$Z_L = 463$ psi sec/ft for Hg

$Z_w = 2022$ psi sec/ft for steel

$m \simeq 0.3\#$

Elastic Termination

H_2O	H_2
$P = 1.94\ P_o$	$P = 1.71\ P_o$

Springlike Termination

H_2O	H_2
$\tau = 2.3\ \mu sec$	$\tau = 17.5\ \mu sec$

ADDENDUM C (Continued)

Mass-Spring Termination

	H_2O	Hg
m_c	$= 0.003\#$	$= 0.165\#$
λ	$= 1.02 \times 10^4 \text{ Sec}^{-1}$	$= 7.79 \times 10^4 \text{ Sec}^{-1}$
ω_N	$= 9.4 \times 10^4 \text{ Sec}^{-1}$	$= 9.4 \times 10^4 \text{ Sec}^{-1}$
ω'	$= 9.34 \times 10^4 \text{ Sec}^{-1}$	$= 5.26 \times 10^4 \text{ Sec}^{-1}$
T	$= 67\ \mu\text{Sec}$	$= 119\ \mu\text{Sec}$
P_{max}	$= 2.25\ P_o$	$= 2.02\ P_o$
σ_{max}	$= 1.71 \frac{P_o D}{2 h}$	$= 1.01 \frac{P_o D}{2 h}$
σ_{max}	$= 0.760 \frac{P_{max} D}{2 h}$	$= 0.500 \frac{P_{max} D}{2 h}$

ADDENDUM D

Preliminary Examination of Combined Loads

The water hammer test used by Marquardt to simulate chamber detonations applies a complex load system to the structure being tested. The internal pressure creates hoop stresses. When the wave is reflected from the end of the chamber, axial stresses are created. These stresses are propagated through the chamber walls, and reflect with increased magnitude from the flanged end of the chamber. As the water hammer wave moves through the liquid, it creates an axial pressure discontinuity. This causes bending stresses to appear in the walls.

All of these stresses are transient, appearing at different positions in the chamber at different times. The computation of the maximum combined loading was beyond the scope of the present analysis. A conservative extimate can be made by summing the peak levels of each of these.

Bending Stress Due to Discontinuity Across the Wave

Consider a cylinder of infinite length within which a pressure wave has created a discontinuity in pressure. To the left of the wave the pressure is zero. To the right the pressure is P

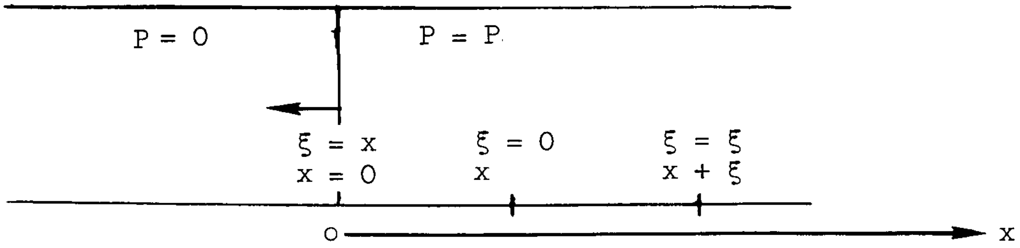

ADDENDUM D (Continued)

Timoshenko(1) gives an expression for the bending moment at x due to a load at ξ as

$$d\,M_x = -\frac{P\,d\,\xi}{4\,\beta}\,\psi\,(\beta\,\xi)$$

Where:

$$\psi\,(\beta\,\xi) = e^{-\beta\,\xi}\,[\cos\beta\,\xi - \mathrm{Sin}\,\beta\,\xi]$$

$$\beta^4 = \frac{12\,(1-\nu^2)}{D^2\,h^2}$$

and ξ is measured away from x.

The total moment at x is then found by integrating over ξ.

$$M_x = \int_{-\infty}^{\infty} d\,M_x$$

$$= \int_{-\infty}^{-x} d\,M_x + \int_{-x}^{\infty} d\,M_x$$

But

$$\int_{-\infty}^{-x} d\,M_x = 0$$

because P is zero over this region.

---

(1) Theory of Plates and Shells, S. Timoshenko: McGray Hill, 1940 pp 389 ff

ADDENDUM D (Continued)

Therefore

$$M_x = \int_{-\infty}^{\infty} d\ M_x$$

$$= \frac{P}{4\ \beta^2}\ e^{-\beta x}\ \text{Sin}\ \beta x$$

It might seem that the use of an integral over an infinite range would invalidate this analysis for the present finite problem. Actually, this is not the case.

$\nu = 0.3$

$D = 2.0$ in.

$h = 0.11$ in.

We find

$$\beta = 3.87\ \text{in.}^{-1}$$

The bending moment is therefore largely due to the pressure loading within 1/4 inch from the point under examination. Pressure applied more than 3/4 inch away has only a negligible effect. Extension of the integration limits to infinity has only a small effect except near the origin of the wave .

ADDENDUM D (Continued)

The maximum bending moment can be found from

$$\frac{\partial M_x}{\partial x} = 0$$

The maximum of $e^{-\beta x}$ Sin βx occurs at

$$\beta x = \frac{\pi}{4}$$

and is given by

$$e^{-\frac{\pi}{4}} \operatorname{Sin} \frac{\pi}{4} = 0.322$$

So that

$$M_{x_{max}} = \frac{0.0805 \, P \, h \, D}{\sqrt{12 \, (1 - \upsilon^2)}}$$

The axial stress due to bending is given by

$$\sigma_\beta = \frac{6 \, M_x}{h^2}$$

$$= 0.294 \, \frac{P \, D}{2 \, h} \quad (\nu = 0.3)$$

This is comparable to the membrane stress in a pressure vessel.

$$\sigma_t = 0.50 \, \frac{P \, D}{2 \, h}$$

A circumferential stress equal to $\nu \, \sigma_\beta$ is created.

ADDENDUM D (Continued)

Stresses Due to End Loading

The end load on the chamber produces an axial stress of

$$\sigma_{max} = \frac{P_o D}{2 h} [1 + \frac{\lambda}{\omega'} e^{-\pi \frac{\lambda}{\omega'}}]$$

and a maximum pressure of

$$P_{max} = 2 P_o [1 + \frac{2 \lambda}{\sqrt{\lambda^2 + \omega'^2}} e^{-\frac{\lambda}{\omega'} \tan^{-1} (\frac{\omega'}{\lambda})}]$$

The stress would be highest for a given P_o for a material that would make

$$\frac{\lambda}{\omega'} = \frac{1}{\pi}$$

Then

$$(\sigma_{max})_{max} = \frac{P_o D}{2 h} [1 + \frac{e^{-1}}{\pi}]$$

$$= 1.117 \frac{P_o D}{2 h}$$

$$(P_{max})_{\sigma_{max}} = 2.81 P_o$$

ADDENDUM D (Continued)

This would yield a stress to pressure ratio of

$$\sigma_{max} = 0.397 \frac{P\ D}{2\ h}$$

For mercury

$$\sigma_{max} = 0.50 \frac{P\ D}{2\ h}$$

For water

$$\sigma_{max} = 0.76 \frac{P\ D}{2\ h}$$

Combined Axial Loads

The end load stresses are propagated through the shell toward the flange from the closed end of the chamber as tension waves. Depending on the nature of the flange structure, these stress waves could double in amplitude upon reflection. The maximum combined stresses in the axial direction would therefore occur when the reflected maximum due to end loading was coincident with the maximum due to the discontinuity across the reflected water hammer wave. An axial wave diagram is shown below which illustrates this point. The wave in the shell is shown starting at the time of the stress peak there, which is at

$$\omega' t = \pi$$

It propagates at the velocity of longitudinal stress waves in the metal, about 20,000 ft/sec.

ADDENDUM B (Continued)

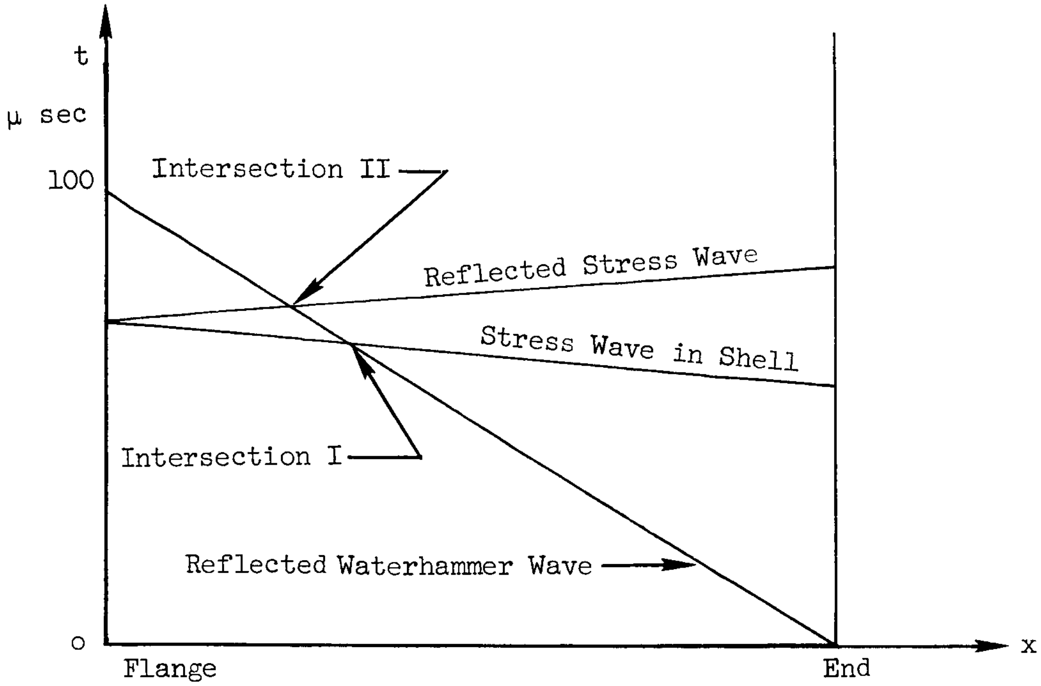

This is clearly an oversimplification of a complex phenomena. Nevertheless, it does indicate that the combined stress peak will be localized both in time and in space. At Intersection I, the stress will be

$$\sigma_I = \sigma_\beta + \sigma_{max}$$

At Intersection II, the stress will be

$$\sigma_{II} = \sigma_\beta + 2\,\sigma_{max}$$

Since the maximum bending stress is

$$\sigma_\beta = 0.294\,\frac{P\,D}{2\,h}$$

ADDENDUM D (Continued)

We find

Fluid → ↓ Stress	$\frac{\lambda}{\omega'} = \frac{1}{\pi}$	Hg	H_2O
$\frac{2\,h}{P\,D} \times \sigma_\beta$	0.294	0.294	0.294
$\frac{2\,h}{P\,D} \times \sigma_{max}$	0.397	0.500	0.760
$\frac{2\,h}{P\,D} \times \sigma_I$	0.691	0.794	1.054
$\frac{2\,h}{P\,D} \times \sigma_{II}$	1.088	1.294	1.814

Circumferential Stresses

A hoop stress of

$$\sigma_H = \frac{P\,D}{2\,h}$$

will exist behind the water hammer wave. In addition, there will be circumferential stresses due to the bending stress at the wave front and the axial tension at the flange. The bending stress gives rise to a circumferential stress

$$\sigma_{c_B} = \nu\,\sigma_B$$

The axial stress causes the shell to contract slightly, except at the flanges. If these are assumed to prevent radial strain, a circumferential stress

ADDENDUM D (Continued)

$$\sigma_{cl} = \nu \, \sigma_{max}$$

will arise. The total circumferential stress will thus also depend on both time and location.

The maximum circumferential stress can be found from

$$\sigma_c = \frac{P\,D}{2\,h} + \nu \, \sigma_{axial}$$

Using 0.3 for ν, these then become

Fluid → ↓ Stress	$\frac{\lambda}{\omega'} = \frac{1}{\pi}$	H_2	H_2O
Wave Front $\frac{2\,h}{P\,D}\,\sigma_c$	1.09	1.09	1.09
Intersection I Near Flange $\frac{2\,h}{P\,D}\,\sigma_{c_I}$	1.21	1.24	1.31
Intersection II Near Flange $\frac{2\,h}{P\,D}\,\sigma_{c_{II}}$	1.33	1.39	1.54

Distribution:

NASA Manned Spacecraft Center Propulsion and Power Division Auxiliary Propulsion and Pyrotechnics Branch/EP4 2101 Webster-Seabrook Road Houston, Texas 77058	Attention: Mr. N. Chaffee Contract NAS 9-4905 3 copies
NASA Manned Spacecraft Center General Research Procurement Branch/BG 721 2101 Webster-Seabrook Road Houston, Texas 77058	Attention: Mr. John J. Twohig Contract NAS 9-4905 1 copy
NASA Manned Spacecraft Center Technical Information Division Library and Documentation Branch/BF 33 2101 Webster-Seabrook Road Houston, Texas 77058	4 copies
Mr. John A. Scheller Office of Manned Space Flight Code MAT NASA Headquarters Washington, D. C.	1 copy
NASA Scientific & Technical Information Facility Atten: Acquisitions Branch (RQT-35662) P. O. Box 33 College Park, Maryland	2 copies